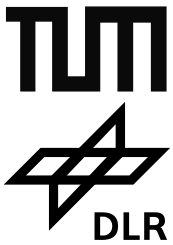

Technische Universität München

Fakultät für Elektrotechnik und Informationstechnik

Professur für Umweltsensorik und Modellierung

Impact of molecular absorption spectroscopy data on methane retrieval from SCIAMACHY and GOSAT shortwave infrared spectra

---

Master's Thesis

Haoran Xu

Supervisors:

Prof. Dr.-Ing. Jia Chen
Dr.rer.nat. Franz Schreier

12 July, 2017

Abstract

Methane is an important species of Earth's atmosphere, highly relevant for climate. Accordingly, a large number of spaceborne sensors are observing this species in the thermal, near and shortwave infrared. For the analysis of shortwave infrared spectra measured by SCIAMACHY aboard the Envisat and the simulated spectra of GOSAT, respectively, in this master thesis the Beer InfraRed Retrieval Algorithm (BIRRA) was used to retrieve methane column densities from the radiance with respect to different sets of observations. Our investigations are based on the separate comparisons of retrieved fitting parameters with respect to the different molecular absorption spectroscopic databases in order to account for their impact on the retrieval quality.

After the analysis, it can be concluded that HITRAN 2012 and GEISA 2015 have a comparable performance with good retrieval quality, HITRAN 1986 achieves the worst quality. Moreover, several useful suggestions are provided for the further improvement on retrieval according to the study.

Contents

List of Figures

Chapter 1

Introduction

1.1 Motivation

Global warming is the continuing rise in the average temperature of Earth's climate system. Through the growing use of factories, fuel consuming cars and other emission from fossil fuels, the Earth's temperature has rapidly increased since the beginning of the industrial age. Today, the quality of the atmosphere has been irreversibly depleted over time because of the global warming, which brings on kinds of hazards to human beings, e.g. unusual heat, sea level rise, frequent tropical storms, flood and so on. It is through something called the enhanced greenhouse effect, which is the key ingredient of global warming. Greenhouse gases include water vapor, carbon dioxide, methane, nitrous oxide and ozone. In our research, we will focus on the investigation of methane (CH_4) retrieval using shortwave infrared spectra from a satellite instrument. For the purpose of obtaining more accurate and consistent concentration data of the trace gases, the impact of the forward model parameters on the final product is intended to be evaluated.

1.2 Remote Sensing of Greenhouse Gases

Remote sensing techniques can be classified into two main surveying ways, passive and active sensing. Passive sensing measures energy that is naturally available, which can be detected in the day, as long as the amount of energy is large enough to be recorded. Fourier Transform spectrometer (FTS) and grating are examples of passive remote sensing. Active sensing (for example RAdio Detection And Ranging (RADAR) and Light Detection And Ranging (LiDAR)), on the other hand, emits artificial radiation and measures the reflected and backscattered radiation from the target to monitor the earth surface or atmospheric features.

The remote sensing methods that can be used to observe and estimate emissions of the greenhouse gases can be classified with respect to the observation platform,

e.g. ground-based, balloon, aircraft and satellite remote sensing. Every method has its own scope of application and advantages. Ground-based measurements of atmospheric CO_2 and CH_4 concentrations began in the 1950s and 1970s. For instance, Network for the Detection of Atmospheric Composition Change (NDACC), formely known as the Network for the Detection of Stratospheric Change (NDSC), which is composed of more than 70 remote sensing research stations for observing the state of the stratosphere and upper troposphere. NDACC monitors the stratosphere with an emphasis on the ozone depletion and also the concentration of the greenhouse gases [Angelbratt et al., 2011]. Another network of groundbased FTS is the Total Column Carbon Observing Network (TCCON) is a network of Fourier Transform spectrometers, providing accurate measurements of column CO_2, CH_4 and other gases [Wunch et al., 2011]. One of the main tasks of TCCON is to validate the observation of satellites [Parker et al., 2011], because it possesses much higher spectral resolution and less noise compared to the satellite. Airplane or balloon instruments can sample the air at different altitudes directly, allowing accurate measurements of column averages to be derived [Washenfelder et al., 2006]. Column readings made at individual TCCON sites have themselves been calibrated using airborne observations of atmospheric composition.

1.3 Satellite Remote Sensing

Among the diverse remote sensing techniques only satellites are able to provide global coverage of the Earth surface. Satellite remote sensing of methane concentration in the Earth's atmosphere is based on spectroscopic measurements which uses the gases' properties of absorbing electromagnetic radiation at specific wavelengths. Many satellite instruments measure the solar radiation that is reflected off the Earth's surface, whereas (thermal) infrared and microwave radiation is emitted by the Earth.

There have been and are several satellite missions to measure column-averaged CH_4 or CO_2 concentrations, e.g. SCanning Imaging Absorption Monitoring Spectrometer for Atmospheric Chartography (SCIAMACHY) [Gottwald and Bovensmann, 2011], Greenhouse Gases Observing Satellite (GOSAT) [Yokota et al., 2004], Orbiting Carbon Observatory 2 (OCO-2), CarbonSat (TanSat) and so on. SCIAMACHY finished the work in 2012, while GOSAT and OCO-2 are currently operating. In the future, satellite missions such as Sentinel-5 Precursor (S5P) or the planned Sentinel-5 (S5, launch in 2020) will carry out the new missions for remote sensing purpose. In this thesis we will use the measurement data from SCIAMACHY and simulated GOSAT observation to proceed our retrieval and research. These two satellite missions are briefly summarised below.

SCanning Imaging Absorption Monitoring Spectrometer for Atmospheric Chartography (SCIAMACHY)

SCIAMACHY was launched onboard Envisat, a European Space Agency (ESA) satellite which operated from 2002 to 2012 with the major mission of measuring atmospheric trace gas concentration as well as aerosol and cloud properties. SCIAMACHY provided one of the earliest record of total column CO_2 and CH_4 measurements with precision of 2-5 ppm in CO_2 and 30-50 ppb in CH_4, with a spatial resolution of 30×60 km^2 (see Buchwitz et al. [2005]). There are three different viewing geometries implemented by SCIAMACHY: nadir, limb, and sun/moon occultations which yield total column values as well as distribution profiles in the stratosphere and (in some cases) the troposphere for trace gases, clouds and aerosols. In standard operation it achieved full global coverage in nadir viewing mode every six days.

Incoming solar radiation is split into 8 channels by the optical unit of the spectrometer. Channels 1 and 2 cover the Ultraviolet (UV) part of the spectrum, channel 3 and 4 are responsible for the visible range and channel 5 measures radiation in the Near-InfraRed (NIR). Channel 6, 7 and 8 collect the Short-Wavelength InfraRed (SWIR) region. Table 1.1 indicates the exact spectral ranges and resolution of the eight channels.

Table 1.1: Specifications of SCIAMACHY channels (from Gottwald and Bovensmann (2011, Table 3.4))

Channel	Spectral Range [nm]	Spectral Range [cm^{-1}]	Resolution [nm]
1	214 - 334	29,940 - 46,728	0.24
2	300 - 412	24,272 - 33,333	0.26
3	383 - 628	15,923 - 26,110	0.44
4	595 - 812	12,315 - 16,807	0.48
5	773 - 1063	9407 - 12,937	0.54
6	971 - 1773	5640 - 10299	1.48
7	1934 - 2044	4892 - 5170	0.22
8	2259 - 2386	4191 - 4426	0.26

Greenhouse Gases Observing Satellite (GOSAT)

GOSAT is operated by the Japanese Aerospace Exploration Agency (JAXA), the Japanese Ministry of the Environment (MOE) and the National Institute for Environmental Studies (NIES). It was launched in January 2009 for the study of transport mechanisms of greenhouse gases such as carbon dioxide (CO_2) and methane (CH_4) in order to monitor these greenhouse gases in the atmosphere. GOSAT is equipped with a spectrometer (TANSO-FTS) and a cloud and aerosol imager (TANSO-CAI). Since its launch, solar absorption spectra with good spectral reso-

lution and high signal-to-noise is delivered by the Fourier Transform spectrometer onboard. GOSAT achieves the global coverage in three days. Measurement precision is 2-3 ppm in CO_2 and approximately 15 ppb in CH_4 (see ESA (2015) Report for Mission Selection).

FTS is an instrument that applies optical interference. Light received by FTS is split into two beams which propagate separately along two different optical paths in order to create an optical path difference between each other. After the recombination of the two beams, it results in the interference. The optical path length difference is continuously changed, meanwhile the FTS measures the intensity of the interference. The distribution of light intensity over a range of wavelengths indicated in a spectrum is obtained via performing Fourier transform on the measured data.

Not only the sunlight reflected from the Earth's surface but also the light emitted from the atmosphere and the surface are observed by FTS. Spectral bands 1 to 3 are in charge of the observation of the former part during the daytime, and the latter part is measured in band 4 both in day and night. The first 3 bands split the light into two paths polarized vertically and horizontally. Band 4 does not split the light. The instrument thereby observes the incoming light in seven different channels. Table 1.2 gives the specfication of the FTS instrument onboard GOSAT.

GOSAT-2 (Greenhouse gases Observing SATellite 2) is a successor to GOSAT and will be launched in 2018 with a design lifetime of 5 years. It will continue and enhance spaceborne measurement of major greenhouse gases from space started by GOSAT in order to monitor the impacts of climate change and human activities on the carbon cycle.

Table 1.2: Specification of FTS on GOSAT (from `http://www.gosat.nies.go.jp/en/about_2_observe.html`)

Band	Target species	Spectral coverage [μm]	Spectral Resolution [μm]
1	O_2	0.758 - 0.775	0.5
2	CO_2, CH_4	1.56 - 1.72	0.27
3	CO_2, H_2O	1.92 - 2.08	0.27
4	CO_2, CH_4	5.56 - 14.3	0.27

1.4 Research Objective

The aim of SCIAMACHY nadir SWIR observation is to retrieve information on atmospheric gases such as CO, CH_4, CO_2 and so on. The research carried out by this thesis is based on the CH_4 retrieval using SCIAMACHY channel 6 radiance spectra.

The inverse problem is solved by the Beer InfraRed Retrieval Algorithm (BIRRA) software that has been developed at the Remote Sensing Technology Institute at DLR. For the weakly absorbing gases, because the signal observed is not strong enough for altitude dependent concentration profile retrieval, it is customary to retrieve CH_4 vertical column densities (VCD) as the final product,

$$N_{CH_4} \equiv \int_{z_{\mathrm{srf}}}^{z_{\mathrm{TOA}}} n_{CH_4}(z)dz \ , \tag{1.1}$$

where z_{srf} is the surface altitude, z_{TOA} is the altitude of top of atmosphere (TOA) and $n_{\mathrm{CH_4}}$ represents the number density of methane. The retrieval analyses are proceeded with respect to the satellite orbit and surface region. The impact of multiple retrieval settings and parameters is also an important subject of ongoing investigation.

Additionally we simulate the GOSAT observation with an ensemble of 42 diverse atmosphere profiles (see section 2.2 in Garand et al. [2001]) and take it as a second set of spectra observations which has better spectral resolution and higher signal-to-noise. The tasks of the research can be generally listed as:

- Intercomparison of the spectroscopic line parameters of different databases
- Altitude sensitivity of different trace gases
- CH_4 retrieval from SCIAMACHY observation and simulated GOSAT spectrum
- Influence of different line database on the retrieval result with respect to the satellite orbit and the Earth's region.

1.5 Outline

In chapter 2 the physical and mathematical background of this work is explained. An overview of atmospheric radiative transfer and inversion theory by means of the least squares method is given. BIRRA as the software package for the retrieval is also introduced. Chapter 3 includes the sensitivity studies which is divided in two parts. A survey of the Jacobians and altitude sensitivity delivers insight into the sensitivity of the retrievals to different altitude regions in addition to useful hints to the appropriate spectral region selection. Moreover, the spectroscopic database (HITRAN 1986, HITRAN 2012 and GEISA 2015) as molecular absorption input are investigated by the comparison of the line parameters. Chapter 4 exhibits the retrieval results using one dataset containing data for one Envisat orbit (orbit 8663) and another dataset comprising data of the Sahara region. The databases mentioned before are utilized to retrieve methane vertical column densities. The final

product VCD as well as other fitting parameters are compared. Chapter 5 displays the retrieval for simulated GOSAT data which are created with diverse atmospheric profiles. In chapter 6 final conclusions are drawn and suggestions for future development of BIRRA are given.

Chapter 2

Theory and algorithm

2.1 Radiative Transfer and Forward Model

The radiative transport equation, which describes how the specific intensity of radiation is changed as it passes through a medium which may absorb, scatter, or add emission to the radiation. On the one hand, radiation $I(\nu)$ passes through a region of extinction (absorption/scattering) in atmosphere with distance ds along a specific path, the change in specific intensity can be described as

$$dI(\nu) = -\varepsilon(\nu, s)\, I(\nu)\, ds \ , \tag{2.1}$$

where $\varepsilon(\nu)$ is the extinction coefficient at wavenumber ν. It consists of absorption α and scattering σ, $\varepsilon = \alpha + \sigma$. Wavenumber is the spatial frequency of a wave: $\nu = \frac{1}{\lambda} = \frac{f}{c}$, where λ is the wavelength, f is the frequency of the wave. We may compute $\varepsilon(\nu)$ as the product of number density n_m of molecule m and absorption cross section k_m

$$\varepsilon(\nu, s) = \sum_m n_m(s)\, k_m(\nu, s) \ . \tag{2.2}$$

For the radiance there will be an exponential fall off in the intensity of initial radiation I_0 as Eq. (2.3) describes, which is derived from Eq. (2.1)

$$\begin{aligned} I(\nu, s) &= I_0(\nu)\, e^{-\int_0^s \varepsilon(\nu, s)\, ds} \\ &= I_0(\nu)\, e^{-\tau(\nu, s)} \ , \end{aligned} \tag{2.3}$$

where $\tau(\nu, s)$ is the optical depth at wavenumber ν. In an inhomogeneous atmosphere, we obtain the optical depth by integrating along the path.

On the other hand, for the emission term, $j(\nu)$ is the emissivity, the contribution of the emissivity of a medium to the flux in general can be a function as

$$dI(\nu) = j(\nu, s)\, ds \ . \tag{2.4}$$

The fundamental equation of radiative transfer is governed by emission and extinction. Combining Eq. (2.1) und Eq. (2.4), we obtain an expression of the equation of radiative transfer, which include a source term J and the weakening of the incident radiation $-\varepsilon I$ by absorption and scattering

$$\frac{\mathrm{d}I(\nu)}{\mathrm{d}s} = j(\nu, s) - \varepsilon(\nu, s)\, I(\nu) \ . \tag{2.5}$$

It is often convenient to express this in terms of optical depth. Dividing by $\varepsilon(\nu, s)$ and recogenizing $d\tau(\nu, s) = ds\, \varepsilon(\nu, s)$:

$$\begin{aligned} \frac{\mathrm{d}I(\nu, s)}{\mathrm{d}\tau(\nu, \mathrm{s})} &= \frac{j(\nu, s)}{\varepsilon(\nu, s)} - I(\nu, s) \\ &= J(\nu, s) - I(\nu, s) \ , \end{aligned} \tag{2.6}$$

J denotes the source function which comprises the intensity's enhancement induced by thermal emission of atmosphere and scattering into the beam direction. By analogy with Eq. (2.3) and Eq. (2.6), the monochromatic intensity of radiation can be expressed as

$$\begin{aligned} I(\tau) &= I_0(\nu)\, e^{-\tau(\nu,s)} + \int_0^{\tau} J(\nu, s)\, e^{-\tau(\nu,s)}\, d\tau(\nu, s) \\ &= I_0(\nu)\, \mathcal{T}(\nu, s) - \int_0^{s} J(\nu, s')\, \frac{\partial \mathcal{T}(\nu, s')}{\partial s'}\, ds' \ . \end{aligned} \tag{2.7}$$

For an arbitrary slant path, the radiance indensity I at wavenumber ν received by an instrument at position $s = 0$ is described by the equation of radiative transfer. I_0 refers to a background contribution at position s and $\mathcal{T}$ is the monochromatic transmission defined by Beer's law,

$$\mathcal{T}(\nu, s) = e^{-\tau(\nu,s)} = \exp\left(- \int_0^{s} \alpha(\nu, s')\, ds' \right) \tag{2.8}$$

$$= \exp\left(- \int_0^{s} ds' \sum_m k_m\big(\nu, p(s'), T(s')\big)\, n_m(s') \right) \ . \tag{2.9}$$

The extinction coefficient ε can be written as α, when scattering σ is neglectable. The absorption coefficient α is affected by different molecules m in the atmosphere. That is why α_m is calculated by summing up the contributions of different molecules.

Assuming local thermodynamic equilibrium in the atmosphere and absence of Rayleigh scattering effect because of the fact that the wavelength of infrared radiation is very long in comparison to the radius of air molecules. The source function J is given by

$$B(\nu, T) = \frac{2\, h\, c^2\, \nu^3}{e^{\frac{hc\nu}{k_B T}} - 1} \ . \tag{2.10}$$

The Planck function B describes the intensity radiated by a blackbody as a function of frequency f (or wavelength) at a given temperature T. h, k_B represent the Planck constant and Boltzmann constant, respectively.

2.1.1 Near Infrared Radiative Transfer by Nadir Viewing

In the near infrared region, the radiative transfer equation can be simplified. Firstly, because of the low contribution, molecular (Rayleigh) scattering can be neglected. Furthermore, the effect of aerosol and cloud scattering on the retrieval can be relieved by proxy modeling (see section 2.4). Thus, the scattering part of the source function is neglected in our radiative transfer forward model. Secondly, since the thermal emission of atmosphere and Earth's surface is negligible compared to the solar radiation from background, Eq. (2.7) can be transformed by discarding the integral part. For a double path through the atmosphere, the intensity of radiation can be expressed as

$$\begin{aligned} I(\nu) &= \frac{r(\nu)}{\pi}\,\mu_\odot\, I_{\text{sun}}(\nu)\,\mathcal{T}_\downarrow(\nu)\,\mathcal{T}_\uparrow(\nu) \\ &= \frac{r(\nu)}{\pi}\,\mu_\odot\, I_{\text{sun}}(\nu) \\ &\quad \exp(-\int_{\text{earth}}^{s_{\text{sun}}} ds' \sum_m k_m\big(\nu, p(s'), T(s')\big)\, n_m(s') \\ &\quad \exp(-\int_{\text{earth}}^{s_{\text{sat}}} ds'' \sum_m k_m\big(\nu, p(s''), T(s'')\big)\, n_m(s'')\ , \end{aligned} \tag{2.11}$$

where r is the surface albedo and $\mathcal{T}_\downarrow$, $\mathcal{T}_\uparrow$ (with $\mathcal{T} = \mathcal{T}_\downarrow\mathcal{T}_\uparrow$) represent the transmission of radiation along the path from the sun to the earth and the earth to observer satellite, respectively. Using a plane-parallel approximation in which the path variable s is assumed to be uniquely related to the altitude z. $s' = z'/\mu$ is calculated with $\mu \equiv \cos\theta$ for an observer zenith angle θ, similarly $s'' = z''/\mu_\odot$ for a solar zenith angle (SZA) $\theta_\odot$.

2.1.2 Molecular Absorption

The molecular absorption cross section denotes the ability of a molecule to absorb a photon of a particular wavenumber and polarization, which is generally obtained by summing over the contributions from many spectral lines,

$$k_m(\nu, z) = \sum_l S_l^{(m)}\big(T(s)\big)\, g\Big(\nu; \hat{\nu}_l^{(m)}, \gamma_l^{(m)}\big(p(z), T(z)\big)\Big)\ . \tag{2.12}$$

A single spectral line is characterized by its position $\hat{\nu}$, line strength S, and line width γ (by convention γ = HWHM (Half width at half maximum) = $\frac{1}{2}$FWHM

(Full width at half maximum). In the spectral range from the Ultraviolet to the microwave, a molecule may undergo a transition to a higher energy level by absorbing electromagnetic radiation and it may drop to a lower level by emitting radiation. Absorption and emission can occur only in association with discrete changes in energy level ΔE. The transition wavenumber $\hat{\nu}$ of absorbed or emitted radiation is related to the change in energy level

$$\hat{\nu} = \frac{\Delta E}{hc} \ . \tag{2.13}$$

For an individual line the cross section is the product of the temperature dependent line strength $S(T)$ and a normalized line shape function $g(\nu)$ describing the broadening mechanism.

2.1.3 Broadening of Absorption Lines

An individual atom/molecule making a transition between energy levels emits one photon with a well-defined energy/frequency. However, profiles of real spectral lines are not infinitely narrow. The finite width of lines can be attributed to the motions and collisions of the gas molecules. In our case, the line shape function is described by a Voigt profile including both, the effect of Doppler broadening and pressure broadening.

Doppler Broadening

Doppler broadening arises from the thermal motions of molecules, which is described by a Gaussian line shape

$$g_D(\nu) = \frac{1}{\gamma_D} \left(\frac{\ln 2}{\pi}\right)^{\frac{1}{2}} \cdot e^{-\ln 2\left(\frac{\nu-\hat{\nu}}{\gamma_D}\right)^2} \ . \tag{2.14}$$

The half width (HWHM) is essentially determined by the line position $\hat{\nu}$, the temperature T, and the molecular mass m,

$$\gamma_D = \hat{\nu}\sqrt{\frac{2\ln 2kT}{mc^2}} \ . \tag{2.15}$$

A Doppler half width for a typical atmospheric molecule of mass $m \approx 36$amu (atomic mass units) is numerically presented as

$$\gamma_D \approx 6 \cdot 10^{-8}\, \hat{\nu}\sqrt{T[K]} \ . \tag{2.16}$$

Pressure Broadening

Pressure (collision) broadening arises from molecular collisions. In this case, g is described by Lorentz line shape function

$$g_L(\nu) = \frac{\gamma_L/\pi}{(\nu - \hat{\nu})^2 + \gamma_L^2} \ , \tag{2.17}$$

where the Lorentz half width γ_L is given by

$$\gamma_L(p, p_s, T) = \left(\gamma_L^{(0,\text{air})} \frac{p - p_s}{p_0} + \gamma_L^{(0,\text{self})} \frac{p_s}{p_0} \right) \times \left(\frac{T_0}{T} \right)^n \ . \tag{2.18}$$

γ_L is proportional to pressure p and decreases by increasing temperature. In the gas mixture, p is the total pressure and p_s is the partial pressure of the absorber molecule. The total width is given by the sum of an air-broadening contribution due to collision with other molecules and a self broadening contribution caused by collision between the absorber molecules. The approximation of exponent n is $\frac{1}{2}$ according to the kinetic theory of gases. The self broadening coefficient $\gamma_L^{(\text{self})}$ is so far known for only a few transitions. If it is not specified, the half width is represented with air broadening coefficient $\gamma_L^{(\text{air})}$. This is also a good approximation for most molecules with small concentration, i.e. $p_s \ll p_{\text{air}}$.

$$\gamma_L(p, T) = \gamma_L^{(\text{air})} \frac{p}{p_0} \times \left(\frac{T_0}{T} \right)^n \ . \tag{2.19}$$

Typical value of air broadening coefficient are $\gamma_L^{(\text{air})} \approx 0.1p[\text{cm}^-1/\text{atm}]$ (see Tab.2 in Rothman et al. [1987])

The Voigt Profile

The width of the absorption line is not determined by a single broadening mechanism. In our forward modeling the line shape $g(\nu)$ is expressed as a Voigt function. The Voigt profile combines effects of both broadenings, which is a convolution of the Lorentzian profile from pressure broadening and the Gaussian profile from Doppler broadening

$$\begin{aligned} g_V(\nu) &= g_L \otimes g_D \\ &= \frac{\sqrt{\ln 2/\pi}}{\gamma_D} K(x, y) \end{aligned} \tag{2.20}$$

$$K(x, y) = \frac{y}{\pi} \int_{-\infty}^{+\infty} \frac{e^{-t^2}}{(x - t)^2 + y^2} \, dt \ , \tag{2.21}$$

where K is the Voigt function, the dimensionless variables x, y are defined in terms of the distance from the line center $(\nu - \hat{\nu}_0)$ and the Lorentz and Doppler half-width γ_L, γ_D:

$$x = \sqrt{\ln 2}\,\frac{\nu - \hat{\nu}_0}{\gamma_D} \quad \text{and} \quad y = \sqrt{\ln 2}\,\frac{\gamma_L}{\gamma_D}\ . \tag{2.22}$$

A comparison of Lorentzian, Doppler, and Voigt half-width is given in Fig. 2.1, in which γ_L, γ_D represent Lorentzian and Doppler half-width. The Lorentzian half-width is proportional to pressure and hence drops approximately exponentially with altitude (black dashed line), while the Doppler broadening shows almost no altitude dependence (solid lines with different color), the half-width varies with the line position. Take spectral line of position $\nu_0 = 1000\,\mathrm{cm}^{-1}$ as an example, below 20 km, pressure broadening is the dominant factor in determining the width of absorption lines, whereas above 50 km, where less frequent molecule collisions happens, Doppler broadening is the dominant factor. Between 20 and 50 km, the line shape is a convolution of the Doppler and Lorentz shapes.

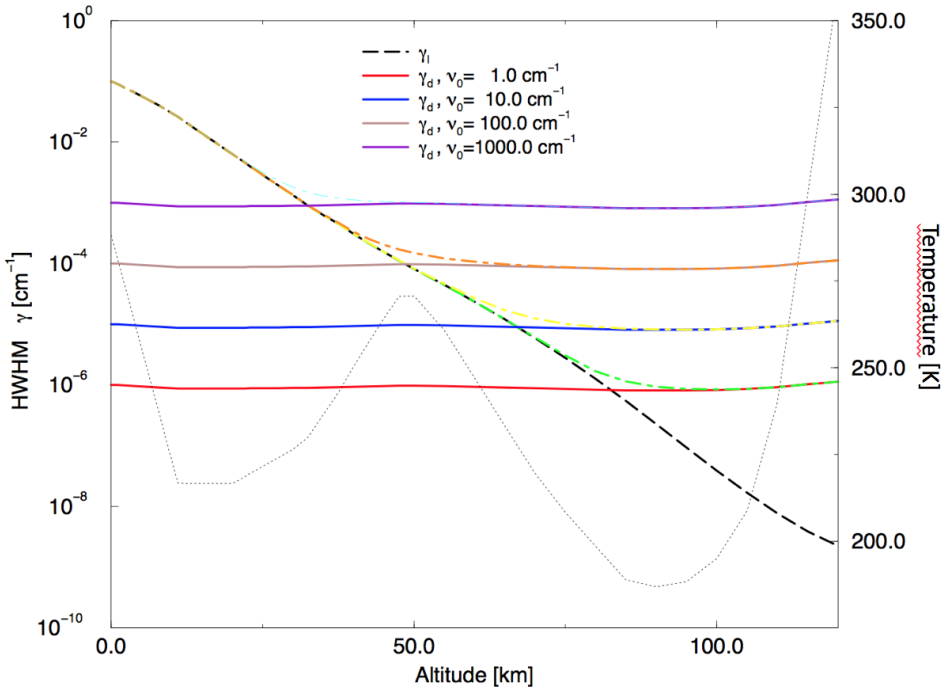

Figure 2.1: Half widths (HWHM) for Lorentz-, Doppler- and Voigt-profile as a function of altitude for a variety of line positions $\hat{\nu}$. (Pressure and temperature: US standard atmosphere, molecular mass 36amu). (Credit: Schreier [2009])

There are only numerical methods to approximate the Voigt line profile due to non-closed form integral included in Eq. (2.21). For more details of the Voigt profile, e.g.

mathematical characteristics, limitation and approaches to numerically approximation, algorithms implement as well as information on complex error function W, see Armstrong [1967]; Schreier [1992, 2009, 2011] and references therein.

2.1.4 Instrument Response Function

Any instrument will induce a smoothing of spectral radiance. For simulating the spectra measured by the instrument, one of the important components is the instrument spectral response function. The monochromatic intensity spectrum calculated by the radiative transfer equation is used to be convolved with a normalized spectral response function S

$$\hat{I}(\nu) \equiv (I \otimes S)(\nu) = \int_{-\infty}^{+\infty} I(\nu') \times S(\nu - \nu')\, d\nu' \ . \tag{2.23}$$

For SCIAMACHY measurements, a Gaussian function is commonly utilized,

$$S_G(\nu, \gamma) = \frac{1}{\gamma} \left(\frac{\ln 2}{\pi} \right)^{1/2} \cdot \exp \left[- \ln 2 \left(\frac{\nu}{\gamma} \right)^2 \right] \ , \tag{2.24}$$

where γ is HWHM. In our study, we simulate the GOSAT measurements with sinc function $\mathrm{sinc}(\nu)$, which is a good approximation for the response function of a FTS.

$$S_s(\nu) = \frac{\sin \nu}{\nu} \ . \tag{2.25}$$

2.2 Inversion Theory

The retrieval objective of nadir satellite observation aims at the vertical distribution of trace gases such as CH_4, CO, N_2O and so on. Our approach to get the vertical column density (VCD) product is through the estimation of molecular scaling factor. The scaling factor of all molecules relevant and other unknown parameters can be fitted by means of nonlinear least squares which can be generally presented as

$$\min_x \| \boldsymbol{y} - \boldsymbol{F}(\boldsymbol{x}) \|^2 \ , \tag{2.26}$$

where $\boldsymbol{y}$ is the measured radiation intensity (a vector of m components), $\boldsymbol{F}$ denotes the forward model: $\mathbb{R}^n \to \mathbb{R}^m$ that corresponds to the radiative transfer equation and instrument model. Combining Eq. (2.11) and Eq. (2.23), the forward model is defined by

$$\begin{aligned} \boldsymbol{F}(\boldsymbol{x}) \ &\equiv \ \hat{I}(\nu) = \frac{r(\nu)}{\pi}\, \mu_\odot\, I_{\mathrm{sun}}(\nu) \\ &\times \ \exp \left[- \sum_m \alpha_m\, \tau_m^{\mathrm{prior}}(\nu) \right] \otimes S(\nu, \gamma) + b(\nu) \ . \end{aligned} \tag{2.27}$$

In our inverse problem, the actual optical depth is represented as scaling factor α_m related with the a-priori optical depth, e.g. optical depth τ of molecule m, $\tau_m(\nu) = \alpha_m \tau^{\text{prior}}$. For each spectral line at wavelength ν, τ_m^{prior} is computed in advance with a-prior profiles such as the molecular volume mixing ratio $q_m(z)$ or number density $n_m(z) = q_m(z) \times n_{\text{air}}(z)$ of molecule m, atmospheric temperature $T(z)$, pressure $p(z)$ which are extracted from climatologial models.

$$\tau_m^{\text{prior}}(\nu) = \int_{z_{\text{srf}}}^{z_{\text{TOA}}} dz' \left(\frac{1}{\mu} + \frac{1}{|\mu_\odot|} \right) n_m^{\text{prior}}(z)\, k_m(\nu, z) \ , \tag{2.28}$$

where $z_{srf}, z_{TOA}, \mu, \mu_\odot$ are observation geometry parameters mentioned above. Additionally, $r(\nu)$ in Eq. (2.27) describes the surface albedo (reflectivity) and $b(\nu)$ is the baseline correction, which are expressed by a polynomial approximation with possible highest degree 2.

$$r(\nu) = r_0 + r_1\nu + r_2\nu^2 \tag{2.29}$$

$$b(\nu) = b_0 + b_1\nu + b_2\nu^2 \tag{2.30}$$

The coefficients of the two polynomials $\boldsymbol{r}, \boldsymbol{b}$ combine with the molecular scaling factor $\boldsymbol{\alpha_m}$ and HWHM γ of the response function to constitute the state vector $\boldsymbol{x} \equiv (\boldsymbol{\alpha}, \gamma, \boldsymbol{r}, \boldsymbol{b})$. In the case of the SCIAMACHY channel 6 retrieval, the width γ is assumed to be known.

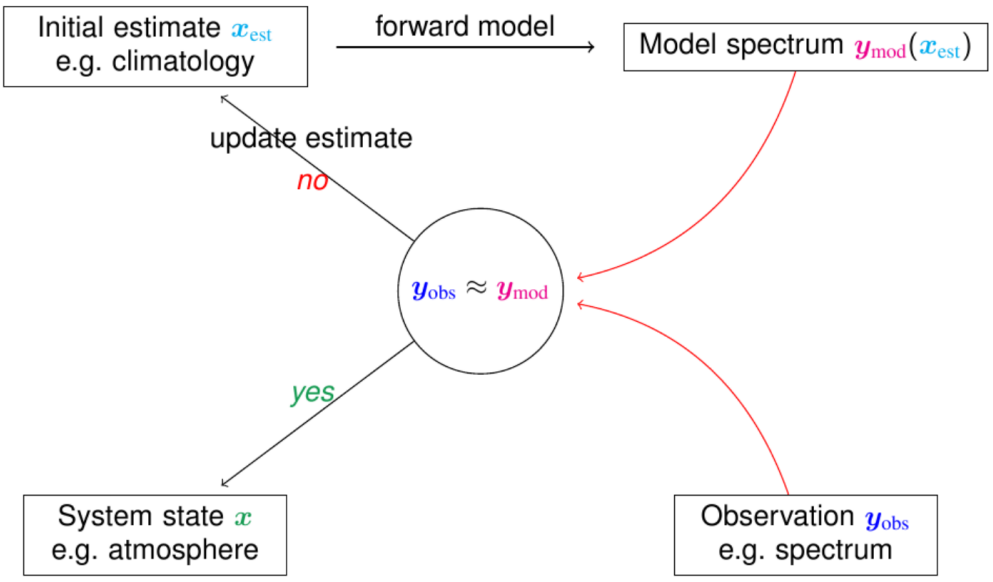

Figure 2.2: Principle of an iterative inversion by optimization

Fig. 2.2 gives an introduction of the iterative inversion by optimization. The evaluation of the state vector $\boldsymbol{x}$ generally requires an iterative calculation method. The

observation $\boldsymbol{y}_{obs}$ is compared with the model spectrum $\boldsymbol{y}_{mod}$ which is calculated with an initial guess of $\boldsymbol{x}$, the state vector would be adapted with correction afterwards for the next comparison. This approach is repeated until the simulated spectrum coincides with the measured spectrum sufficiently precisely, which results in the final state vector. This comparing method applies least squares approach. A series of articles on "Fitting Nature's Basic Function", published by Rust [2001a,b, 2002, 2003] gives a more detail discussion of the least squares method and for the application of iterative method of inversion in the remote sensing field one can refer to Stephens [1994].

2.2.1 Nonlinear Least Squares

In case of a nonlinear least squares problem, an iterative process is used. The iteration is terminated when a convergence criterion is satisfied. Initial estimations for the elements of state vector $\boldsymbol{x}$ are required for finding the solution to a nonlinear least squares problem.

$$\boldsymbol{x}^{k+1} = \boldsymbol{x}^k + \Delta\boldsymbol{x} \ , \tag{2.31}$$

where k is an iteration number, and the update vector $\Delta\boldsymbol{x}$ indicates the increment for each iteration. Fitting of the forward model $\boldsymbol{F}$ depending on the unknown state vector $\boldsymbol{x}$ with n parameters to the observation data set $\boldsymbol{y}$ for each sampling point $t_i, i = 1, 2, ..., m$ can be achieved by minimizing the objective function,

$$\boldsymbol{\Phi}(\Delta\boldsymbol{x}) = \sum_{i=1}^{m} \left[\boldsymbol{y} - \boldsymbol{F}(\boldsymbol{x}^k + \Delta\boldsymbol{x})\right]^2 \ . \tag{2.32}$$

Linearization of the forward model is achieved by approximation to a first-order Taylor series expansion about $\boldsymbol{x}^k$

$$\boldsymbol{F}(\boldsymbol{x}^k + \Delta\boldsymbol{x}) = \boldsymbol{F}(\boldsymbol{x}^k) + \Delta\boldsymbol{x}\,\boldsymbol{J}(\boldsymbol{x}^k) \ , \tag{2.33}$$

where $\boldsymbol{J}(\boldsymbol{x}^k)$ denotes the $m \times n$ Jacobian matrix containing the first-order partial derivatives of the forward model function $\boldsymbol{F}$ with respect to the unknown parameters x_j of the state vector. It is defined and arranged as follows,

$$\boldsymbol{J}_{i,j}(\boldsymbol{x}) = \frac{\partial \boldsymbol{F}(t_i, \boldsymbol{x})}{\partial x_j} \ . \tag{2.34}$$

By substituting the foward model in the objective function $\boldsymbol{\Phi}$ with Taylor expansion, the objective function can be rewritten as

$$\boldsymbol{\Phi}(\Delta\boldsymbol{x}) = \left[\left(\boldsymbol{y} - \boldsymbol{F}(\boldsymbol{x}^k)\right) - \Delta\boldsymbol{x}\,\boldsymbol{J}(\boldsymbol{x}^k)\right]^T \left[\left(\boldsymbol{y} - \boldsymbol{F}(\boldsymbol{x}^k)\right) - \Delta\boldsymbol{x}\,\boldsymbol{J}(\boldsymbol{x}^k)\right] \ . \tag{2.35}$$

Assume the partial derivative of the objective function $\boldsymbol{\Phi}(\Delta \boldsymbol{x}^k)$ with respect to the unknown increment to be zero, which results in an estimate of $\Delta \boldsymbol{x}^k$,

$$\Delta \boldsymbol{x}^k = \left[\boldsymbol{J}(\boldsymbol{x}^k)^T \boldsymbol{J}(\boldsymbol{x}^k)\right]^{-1} \boldsymbol{J}(\boldsymbol{x}^k)^T \left(\boldsymbol{y} - \boldsymbol{F}(\boldsymbol{x}^k)\right) \ . \tag{2.36}$$

Then the correction term $\Delta \boldsymbol{x}^k$ can be used for the estimate of the next iteration step. The iterative method is called Gauss-Newton algorithm.

2.2.2 Separable Nonlinear Least Squares

The forward model function Eq. (2.27) depends linearly on the parameters surface albedo r and baseline correction b of the state vector $\boldsymbol{x}$. Hence the separable nonlinear least squares method can be applied in our inverse problem. Eq. (2.26) can be reduced to a separable nonlinear least squares problem (see Golub and Pereyra [2003]). Then the state vector $\boldsymbol{x}$ can be splitted in two vectors, one vector $\boldsymbol{\eta}$ includes nonlinear parameters and the other vector $\boldsymbol{\beta}$ contains the linear parameters.

$$\boldsymbol{\eta} \equiv (\boldsymbol{\alpha}, \gamma) \in \mathbb{R}^p \qquad \boldsymbol{\beta} \equiv (\boldsymbol{r}, \boldsymbol{b}) \in \mathbb{R}^q \ . \tag{2.37}$$

The forward model can be transformed as

$$\boldsymbol{F}(\boldsymbol{x}) = \sum_{l=1}^{q} \beta_l \, \boldsymbol{f}_l(\eta) \ . \tag{2.38}$$

$\boldsymbol{f}_l$ for $l = 1,...,q$ can be integrated in a matrix defined as

$$\boldsymbol{M}(\eta) = (\boldsymbol{f}_1(\boldsymbol{\eta}), \boldsymbol{f}_2(\boldsymbol{\eta}), ..., \boldsymbol{f}_q(\boldsymbol{\eta})) \, , \text{with } \boldsymbol{M} \in \mathbb{R}^{m \times q} \ . \tag{2.39}$$

Then the Eq. (2.26) can be rewritten as a linear least squares problem

$$\min_{\beta} \|\boldsymbol{y} - \boldsymbol{M}\boldsymbol{\beta}\|^2 \ . \tag{2.40}$$

The vector $\boldsymbol{\beta}$ can be calculated by

$$\boldsymbol{\beta} = \left(\boldsymbol{M}^T \boldsymbol{M}\right)^{-1} \boldsymbol{M}^T \boldsymbol{y} \ . \tag{2.41}$$

Substitute the $\boldsymbol{\beta}$ into the original least squares problem, Eq. (2.26) can be rewritten as

$$\min_{\eta} \left\| \boldsymbol{y} - \sum_{l} \left(\left(\boldsymbol{M}^T \boldsymbol{M}\right)^{-1} \boldsymbol{M}^T \boldsymbol{y} \right)_l \boldsymbol{f}_l(\boldsymbol{\eta}) \right\|^2 \ . \tag{2.42}$$

At last a nonlinear least squares problem for $\boldsymbol{\eta}$ can be solved by the way of Gauss-Newton or Levenberg-Marquardt algorithms. The main advantages of applying the separable nonlinear least squares can be concluded in several points

- Only the vector with nonlinear parameters $\boldsymbol{\eta}$ needs to be iterated for the calculation, which reduces lots of work.
- The linear parameter $\boldsymbol{\beta}$ is obtained from Eq. (2.41), no initial estimation is required.
- The size of the Jacobian matrix is reduced.

2.3 BIRRA - Beer InfraRed Retrieval Algorithm

BIRRA, developed at the Remote Sensing Technology Institute at DLR, is a flexible and robust algorithm written in Fortran. It achieves the processing of level-1b to level-2 data. BIRRA performs a (separable) nonlinear least squares fit with the main objective of retrieving atmospheric trace gas. Two major parts compose the BIRRA algorithm, the forward model and inverse problem solver. The forward model part describing the radiative transfer (Sect. 2.1) is based on Generic Atmospheric Radiation Line-by-Line Infrared Code (GARLIC) algorithm, which is described in detail by Schreier et al. [2014, 2015]. The least squares solver is provided by the PORT library [Gay, 1990].

2.3.1 Input

The input level-1b data is observed radiance spectra after calibration. SCIAMACHY data is arranged according to the orbit number. The measurement for each orbit consists of multiple states and each state is comprised of 70 to 130 observation spectra. BIRRA is optimized for the use on a Linux operating system and it is executed by the following shell-command,

birra < **file.in** > **file.out** ,

where **file.in** is the input file that provides all the information about the data and settings which are processed and **file.out** is the log file of the calculation process. Fig. 2.3 and 2.4 show examples of the input file and forward file. The forward file is required for the forward modeling, which includes the "spaceFile" that provides solar irradiance spectrum. The molecules which are intended to be retrieved would be announced in the forward file. The spectroscopic line parameters of the retrieved molecules are also defined by the forward file. Besides the level-1b input radiance spectra defined in the **file.in**, the input file specifies several quality measures, the specifications for the nonlinear least squares solver (PORT library), and the atmospheric input files including climatological background information.

COSPAR International Reference Atmosphere (CIRA) and National Center for Environmental Prediction (NCEP) provide the a-priori information on the atmospheric

conditions at the time of the observation. CIRA was developed in 1986 [Fleming et al., 1990] by the Committee on Space Research (COSPAR), that provides monthly mean value of temeprature and pressure profiles. The profiles are marked by a latitude dependent grid with a resolution of 5° from −80° to 80°. An alternative climatological database is from the NCEP Reanalysis project (NOAA, 2014) provided by National Oceanic & Atmospheric Adminstration (NOAA). Not only atmospheric temperature and pressure profile but also H_2O content is provided by it. NCEP provides daily average values and is continuously updated. The spatial resolution is 2.5° in latitude and longitude. The NCEP data provides more accurate a-priori estimates for atmospheric temperature, pressure and water vapor concentrations with the help of higher spatial and temporal resolution. Furthermore, The a-priori profile molecular Volume Mixing Ratio (VMR) is read from AFGL (Air Force Geophysics Laboratory) atmospheric constituent database [Anderson et al., 1986].

```
&FLAGS forward='forward_ch4_hitran12.in',
    fitFile='specture.fit', specFile='specture.r',
    IntPol='a', quad='T', verbose='0', nWindows=2 /

 &QUALITY  rcBounds = 3, 6,
        alphaBounds = -1., 3.,
                -1., 3.,
                -1., 3.,
        errorMaxs = 0.5, 0.5, 0.5,
        residuumNormMax = 1.,
        residuumMax = 10.       /

 &PORT  method='port',
        XFtol=1.e-3, RFCtol=1.e-3, Aux='rrr',
        logFile='=.PORT',
        Separable=f,
        UseBounds = f,
        mxIter=-10, mxFCal=60,
        Bounds=0.0001,1000.,
                0.0001,1000.,
                0.0001,1000.,
                0.010,0.500,
                0.00123,0.500                                   /

 &Atmosphere File='/users/xu_ho/home/MA/inversion/ncep_reanalysis_data_0.nml', hgtMax=60.  /
 &FETCH   WHAT='Pres'                                                    /
 &FETCH   WHAT='Temp'                                                    /
 &FETCH                                                                  /
 &Atmosphere File='/home/donau101/mirror/hoch_pi/scia/l1b_to_l2_prototype/ADF_defaults/atm/bias.nml'              /
 &FETCH   WHAT='CH4' ,                                                   /
 &FETCH   WHAT='CO2',                                                    /
 &FETCH                                                                    /
 &Atmosphere File='/users/xu_ho/home/MA/inversion/ncep_reanalysis_data_0.nml'                                  /
 &FETCH   WHAT='H2O',                                                    /
 &FETCH                                                                  /
 &Atmosphere                                                             /


 &Observed  ObsDir='/users/xu_ho/home/MA/level1c/s000_ch6_cl43',
         xLow=5985.5959, 6273.3534,
         xHigh=6138.8971, 6418.9935,
            file='observation_004',   xShift=0.0, unitX='cm-1',  UnitY='erg/s/(cm2.sr.cm-1)', Instrument='Gauss: 2.45 2.64 ', Reflexion=0.1 /
 &Observed  file='observation_005',   xShift=0.0, unitX='cm-1',  UnitY='erg/s/(cm2.sr.cm-1)', Instrument='Gauss: 2.45 2.64 ', Reflexion=0.1 /
 &Observed  file='observation_006',   xShift=0.0, unitX='cm-1',  UnitY='erg/s/(cm2.sr.cm-1)', Instrument='Gauss: 2.45 2.64 ', Reflexion=0.1 /
 &Observed  file='observation_007',   xShift=0.0, unitX='cm-1',  UnitY='erg/s/(cm2.sr.cm-1)', Instrument='Gauss: 2.45 2.64 ', Reflexion=0.1 /
 &Observed  file='observation_008',   xShift=0.0, unitX='cm-1',  UnitY='erg/s/(cm2.sr.cm-1)', Instrument='Gauss: 2.45 2.64 ', Reflexion=0.1 /
 &Observed  file='observation_009',   xShift=0.0, unitX='cm-1',  UnitY='erg/s/(cm2.sr.cm-1)', Instrument='Gauss: 2.45 2.64 ', Reflexion=0.1 /
 &Observed  file='observation_010',   xShift=0.0, unitX='cm-1',  UnitY='erg/s/(cm2.sr.cm-1)', Instrument='Gauss: 2.45 2.64 ', Reflexion=0.1 /
 &Observed  file='observation_011',   xShift=0.0, unitX='cm-1',  UnitY='erg/s/(cm2.sr.cm-1)', Instrument='Gauss: 2.45 2.64 ', Reflexion=0.1 /
 &Observed  file='observation_012',   xShift=0.0, unitX='cm-1',  UnitY='erg/s/(cm2.sr.cm-1)', Instrument='Gauss: 2.45 2.64 ', Reflexion=0.1 /
```

Figure 2.3: Example of BIRRA input file with input options and parameters setting

```
&FORWARD  intPol='3', quad='T', verbose='0',
          contFile='/home/donau101/mirror/IR/data/continua/ckd',
          MFile='/home/donau101/mirror/IR/data/molecules',                    /

&Sources  spaceFile='/home/donau101/data/gime_se/scia/l1b_to_l2/ADF_defaults/solar/ones_IR.dat', vLow=5882., vHigh=6430., yUnit='erg/s/cm^2'         /

&Xsection File='/home/donau101/mirror/IR/data/hitran/2012/lines.NIR', WHAT='line'     /
&Lbl      Molecule='CH4'                                                 /
&Lbl      Molecule='CO2',                                                 /
&Lbl      Molecule='H2O', LineShape='Voigt CKD',                         /
&Lbl                                                                     /

&Xsection /
```

Figure 2.4: Example of the forward file that is called by the input file

2.3.2 Output

The output files include the log file **file.out** and fit file **file.fit**. The final retrieval product is saved in the fit file which is specified in the input file. According to the input settings, BIRRA also has the possibilities to output more information such as model spectrum from forward model, Jacobians of variables in the state vector. The relevant output parameters for methane retrieval are listed in Table. 2.1. The left column gives the parameters' names in the fit output and the right column contains a short discription. For general information about SCIAMACHY data processing and products, see Gottwald and Bovensmann [2011] Chap. 8.

2.4 Product Definition

There are several unconsidered effects that may cause a significant impact on the fitted scaling factors in the retrieval process [Gimeno García et al., 2011]. Firstly, although in the BIRRA forward model scattering is neglected, in practice it is inevitable that a fraction of the measured radiance comes from scattering events in the atmosphere. It results in the deviation of a photon path from the pure geometrical one (from top of atmosphere to the Earth's surface, and reflected from the surface to the satellite). Secondly, the a-priori atmospheric profile is read from the climatological dataset, but the actual meteorological conditions (e.g. pressure, temperature) are unknown. To account for these effects, the vertical column densities are presented as "proxy" normalized vertical column densities instead of directly retrieved VCDs. In case of CH_4 retrievals from SCIAMACHY channel 6, carbon dioxide is chosen as the proxy. The amount of CO_2 can be determined with high accuracy due to strong absorption lines across the CO_2 fitting window.

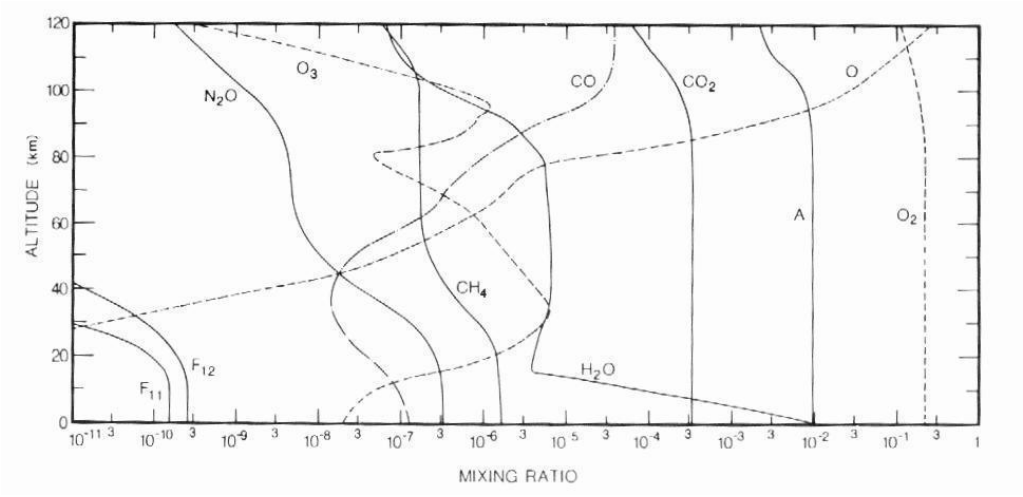

Figure 2.5: Vertical volume mixing ratio profiles of molecular species in the Earth's atmosphere (Credit: Goody and Yung [1989])

Table 2.1: A subset of parameters contained in BIRRA fit file for CH_4 retrieval

name	remark
S	number of the state in the orbit
s	number of the observed spectrum in the state
subLat	geographic latitude of the observation (in degree)
subLon	geographic longitude of the observation (in degree)
LatA	corner latitude of the ground pixel (in degree)
LonA	corner longitude of the ground pixel (in degree)
LatB	corner latitude of the ground pixel (in degree)
LonB	corner longitude of the ground pixel (in degree)
LatC	corner latitude of the ground pixel (in degree)
LonC	corner longitude of the ground pixel (in degree)
LatD	corner latitude of the ground pixel (in degree)
LonD	corner longitude of the ground pixel (in degree)
zenith	zenith angle (in degree)
sza	solar zenith angle (in degree)
azimuth	azimuth angle (in degree)
height	altitude above sea level (in m)
cf	cloud fraction (in %)
rc	PORT return code indicating convergence
normRes	norm of residuals final estimation, difference of observed and modeled spectrum
normRes0	norm of residuals initial guess
VCD	methane vertical column densities (in molecules/cm^2)
errVCD	error of retrieved VCD
CH_4	scale factor for methane α_{CH_4}
errCH_4	error of α_{CH_4}
CO_2	scale factor for carbon dioxide α_{CO_2}
errCO_2	error of α_{CO_2}
H20	scale factor for water vapor α_{H_2O}
errH2O	error of α_{H_2O}
width	slit function half-width (in cm^{-1})
errwidth	error of the slit function half width (in cm^{-1})
shift	wavenumber shift (in cm^{-1})
errshift	error of the wavenumber shift (in cm^{-1})
refl0	surface reflectivity zero order coefficient
errRefl0	error of the surface reflectivity zero order coefficient
refl1	surface reflectivity first order coefficient
errRefl1	error of the surface reflectivity first order coefficient
refl2	surface reflectivity second order coefficient
errRefl2	error of the surface reflectivity second order coefficient
air	air density (in molecules/cm^2)
CH_4ref	CH_4 a-priori estimate
CO2ref	CO_2 a-priori estimate
H2Oref	H_2O a-priori estimate

Additionally, from Fig. 2.5 it can be seen, that the concentration level of CO_2 is spatially stable, consequently, CO_2 has quite homogeneous global distributions. These factors make CO_2 a suitable proxy for methane retrieval. So, the proxy-normalized CH_4 vertical column density is defined as

$$\mathrm{xCH_4} \equiv N_{\mathrm{CH_4}}^{\mathrm{prior}} \times \frac{\alpha_{\mathrm{CH_4}}}{\alpha_{\mathrm{CO_2}}} , \tag{2.43}$$

where $N_{\mathrm{CH_4}}^{\mathrm{prior}}$ is the a-priori vertical column density of CH_4, and α_{CH4}, α_{CO2} are the scaling factors of CH_4 and CO_2, respectively.

Chapter 3

Sensitivity Studies

3.1 Jacobians and Altitude Sensitivity

In SCIAMACHY channel 6, two fitting windows are selected with the spectral range 5986 to 6139 cm^{-1} and 6273 to 6419 cm^{-1} for the CH_4 retrieval. Fig. 3.1 shows the absorption spectral radiance of three single molecules after simulation by the forward model. In the calculation NECP provides the atmospheric temperature and pressure as well as the VMR profile of water vapor. CH_4 and CO_2 profiles are given by AFGL (Air Force Geophysics Laboratory) standard. A Gaussian slit function with $\gamma = 2.45\,\mathrm{cm}^{-1}$ and $\gamma = 2.64\,\mathrm{cm}^{-1}$ are set for the two fitting windows, respectively. In the first spectral interval, three different molecules represented by three colors make the main contributions to the radiance spectra, they are CH_4, CO_2 and H_2O as the background, respectively. In the second spectral interval, CO_2 and water vapor are dominant. According to Eq. (2.43), for an accurate retrieval of CH_4, it is necessary to obtain the concentration information of CO_2. Therefore, in practice, the second fitting window is utilized for the retrieval of CO_2 as the measured signal is not dominated by other interfering gases.

At the beginning, a study of the altitude sensitivity of the trace gases is processed. The Jacobian, $J \equiv \partial \boldsymbol{F}/\partial \mathrm{VMR}(z)$, the partial derivatives of the model function with repect to the molecular volume mixing ratio delivers insight into the sensitivity of the trace gases' retrievals to different altitude regions and also verifies the superiority of selected spectral interval.

The derivativies were calculated using GARLIC (Generic Atmospheric Radiation Line-By-Line Infrared Code) [Schreier et al., 2014] for a standard AFGL midlatitude summer atmosphere [Anderson et al., 1986] up to 80 km, a Gaussian slit function with $\gamma = 1\,\mathrm{cm}^{-1}$, and vertical downlooking at 870 km. As Fig. 3.2 shows, the signal is sensitive to CH_4 at the spectral interval $5986 - 6139\,\mathrm{cm}^{-1}$, to CO_2 at the spectral interval $6050 - 6110\,\mathrm{cm}^{-1}$ and $6320 - 6375\,\mathrm{cm}^{-1}$, and to H_2O mainly at the interval $5986 - 6139\,\mathrm{cm}^{-1}$. Obviously, CO_2 is dominant at the interval $6273 - 6419\,\mathrm{cm}^{-1}$,

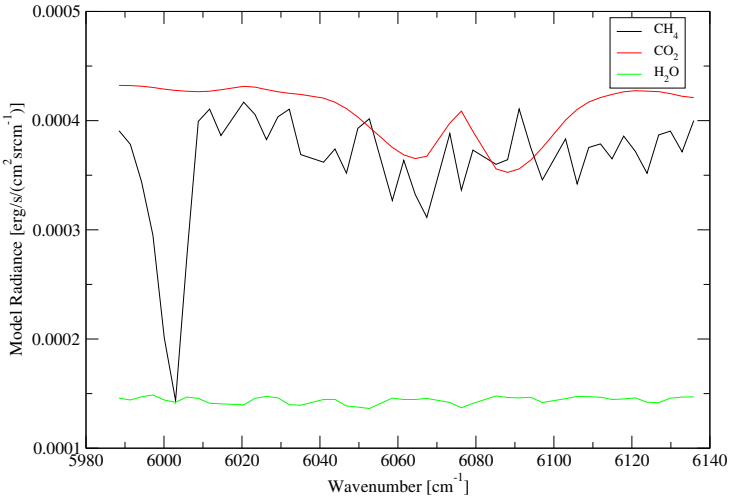

(a) Model radiance in the spectral range between 5986 and 6139 cm^{-1}

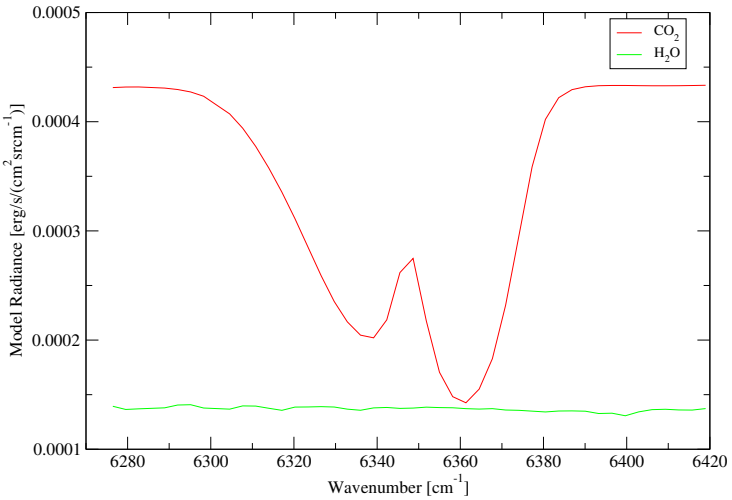

(b) Model radiance in the spectral range between 6273 and 6419 cm^{-1}, $I_{CH_4} \leqslant 10^{-4}$.

Figure 3.1: Model radiance in spectral interval of two fitting windows

confirming the reason of selecting the second fitting window for the CO_2 retrieval.

For the altitude sensitivity of retrieval, it can be seen that CH_4 is sensitive for the altitude region below 10 km in the troposphere and the highest sensitivity is located

between 1.2 and 2.5 km. The sensitive region for CO_2 extends to the height 18 km and at 3 km it is most sensitive. H_2O has a wider sensitive altitude region up to 20 km. According to the sensitivity studies in respect to the spectral range and altitude, CH_4 retrieval in the selected spectral range is theoretically feasible.

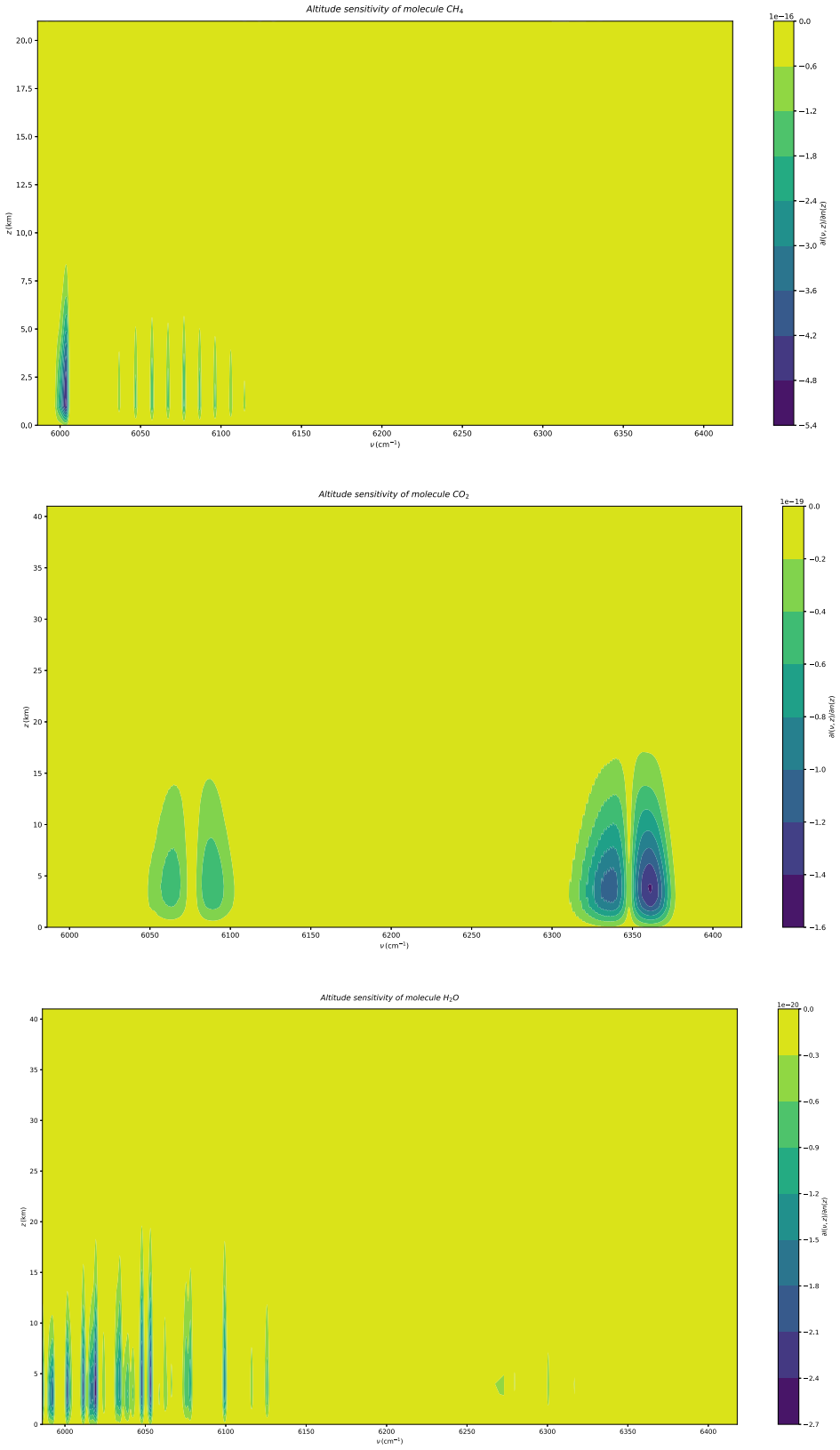

Figure 3.2: Jacobians [erg/s/(cm^2 sr cm^{-1})/ppm] for molecular concentration profile retrieval in SCIAMACHY channel 6: CH_4, CO_2, H_2O. (Note: Altitude range is different for three figures.)

3.2 The Spectroscopic Database

Accurate spectroscopic information on radiatively active molecules in the atmosphere is essential for trace gas retrieval, it is used to predict and simulate the transmission and emission of light in the atmosphere. The line parameters, i.e line position $\hat{\nu}$, line strength S, line width γ (air- and self-broadened HWHM) and so on, are required for radiative transfer calculations. Such spectroscopic information are read from the molecular absorption database which plays an important role in the radiative transfer model. HITRAN is an acronym for high-resolution transmission molecular absorption database, which is maintained and developed at the Harvard-Smithsonian Center for Astrophysics. HITRAN was known as AFCRL (Air Force Cambridge Research Laboratory) in the early seventies. Then it has been continuously updated since 1987 [Rothman et al., 1987, 1992, 1998, 2003, 2005, 2009, 2013]. More information on HITRAN is available at `https://www.cfa.harvard.edu/hitran/`. Besides HITRAN, the GEISA (Gestion et Etude des Informations Spectroscopiques Atmosphériques) database is another spectroscopic database, designed to facilitate accurate forward radiative transfer calculations using a line-by-line approach. It is developed by the AMD (Atmospheric Radiation Analysis) working group at LMD (Laboratoire de Mét'eorologie Dynamique, France). Since the publication of the first version in 1982 by Chédin et al. multiple updates have been released [Husson et al., 1992; Jacquinet-Husson et al., 1999, 2008, 2011, 2016].

In order to find out the impacts on the retrieval results by using different databases and to check whether the more recently released version would yield better retrieval results, three different databases are utilized as molecular absorption inputs for the trace gases retrieval, two most recent compilations HITRAN 2012, GEISA 2015 and the earliest edition HITRAN 1986. For the GOSAT analysis only HITRAN 2012 and GEISA 2015 are compared.

3.3 Line Parameter Comparison for the SWIR

For assessing the impact of spectroscopic information on radiative transfer calculation, a comparison of the spectroscopic information between the different databases is conducted at first. These parameters are extracted from the databases mentioned before and the spectral windows are specified for methane retrieval in the SWIR.

Fig. 3.3 shows the spectral line strength S of CH_4, CO_2 and H_2O in the first spectral interval $5986 - 6139\,\mathrm{cm}^{-1}$ which lies in the range of SCIAMACHY channel 6. Three subfigures represent three different databases, respectively. At first sight, the two most recent compilations reveal very similar appearance for the line strength of three molecules. By contrast, the old version HITRAN 1986 has much less lines

and many more weak lines are identifiable in the new databases. Table 3.1 shows the minimal and maximal line strength detected in each databases. By HITRAN 2012 and GEISA 2015, the maximum line strengths for three molecules are in fairly good agreement with each other. HITRAN 1986 provides a smaller range of the line strength.

Table 3.1: The range of line strength S [$\mathrm{cm}^{-1}/(\mathrm{molec\ cm}^{-2})$] for different molecules extracted from three databases.

	HITRAN 1986	HITRAN 2012	GEISA 2015
CH_4	$[3.07{\cdot}10^{-24}, 1.17{\cdot}10^{-21}]$	$[3.75{\cdot}10^{-27}, 1.5{\cdot}10^{-21}]$	$[3.75{\cdot}10^{-27}, 1.5{\cdot}10^{-21}]$
CO_2	$[3.71{\cdot}10^{-27}, 2.02{\cdot}10^{-24}]$	$[1{\cdot}10^{-30}, 1.73{\cdot}10^{-24}]$	$[1{\cdot}10^{-30}, 1.74{\cdot}10^{-24}]$
H_2O	$[3.35{\cdot}10^{-27}, 8.94{\cdot}10^{-25}]$	$[1.02{\cdot}10^{-29}, 1.1{\cdot}10^{-24}]$	$[1.02{\cdot}10^{-29}, 1.1{\cdot}10^{-24}]$

As Table 3.2 indicates, in the first spectral interval the number of lines for CH_4 increased from 130 (HITRAN 1986) to 5317 (HITRAN 2012), CO_2 increased from 335 to 7159, H_2O has been also raised by a factor of six against 1986 approximately. Due to the advanced spectral measurement techniques and the possibility of more sophisticated theoretical treatment much more molecule lines are identified in the latest database version. The amount of lines detected in GEISA 2015 is close to the HITRAN 2012.

Table 3.2: The number of lines for investigated molecules (CH_4, CO_2, H_2O) extracted from three databases with respect to the first spectral interval and the total number of molecules and spectral lines listed in the databases.

	CH_4	CO_2	H_2O	number of molecules	total lines
HITRAN 1986	130	335	122	28	398043
HITRAN 2012	5317	7159	748	47	7900447
GEISA 2015	5318	7611	806	52	5067351

Fig. 3.4 shows the air broadening HWHM γ_{air} extracted from three databases. γ_{air} of CO_2 and H_2O extracted from HITRAN 2012 and GEISA 2015 are similar, whereas for CH_4, significant differences can be found when γ_{air} ranging between 0.05 and $0.06\,\mathrm{cm}^{-1}$. Table 3.3 shows the extreme values of γ_{air} for the three databases, HITRAN 2012 has a smaller minimum and a bigger maximum than GEISA 2015 for the air broadening HWHM of CH_4. For the other two molecules the values are close to each other by HITRAN 2012 and GEISA 2015.

Fig. 3.5 displays the total optical depth calculated with Py4CAtS (Python for Computational ATmospheric Spectroscopy) [Schreier and Gimeno García, 2013]. It is

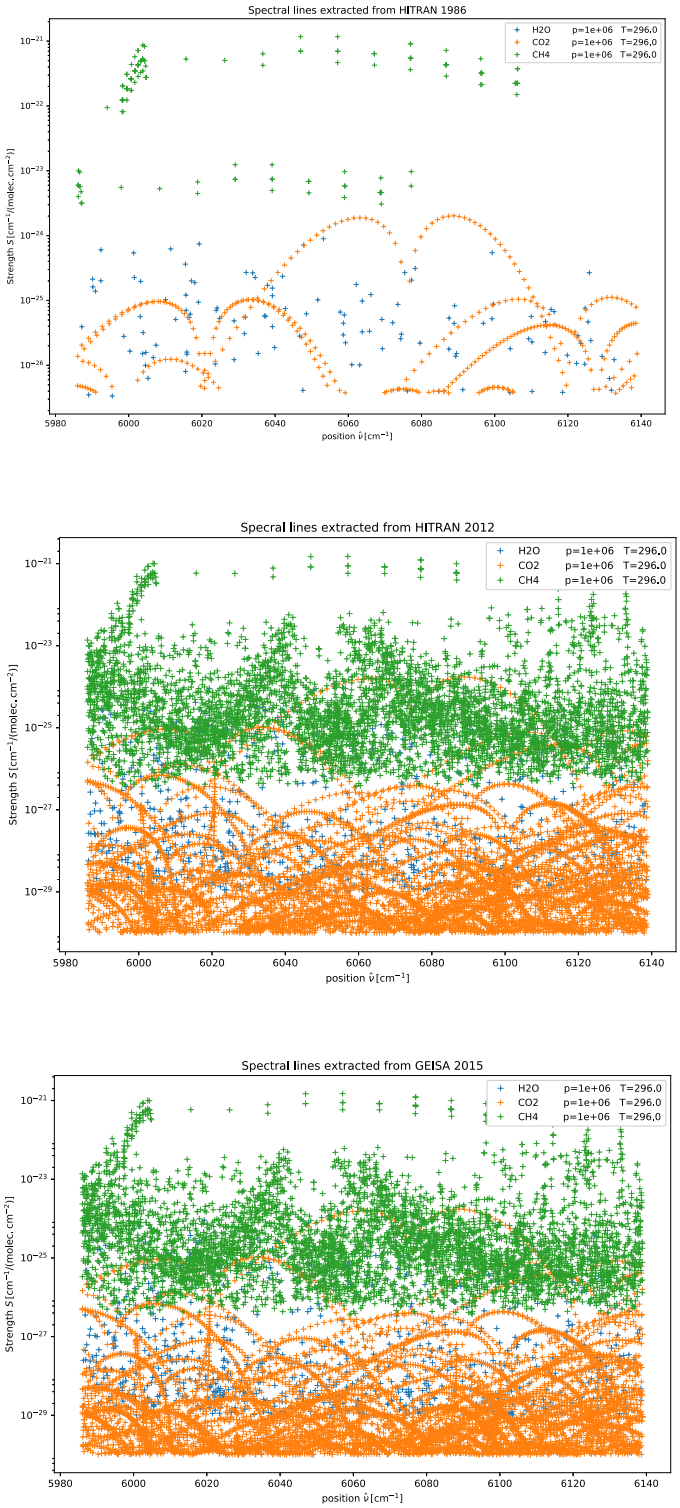

Figure 3.3: Spectral lines in the first spectral interval for CH_4, CO_2 and H_2O extracted from HITRAN 1986, HITRAN 2012 and GEISA 2015 databases. (Note: the different range of the y=S axis.)

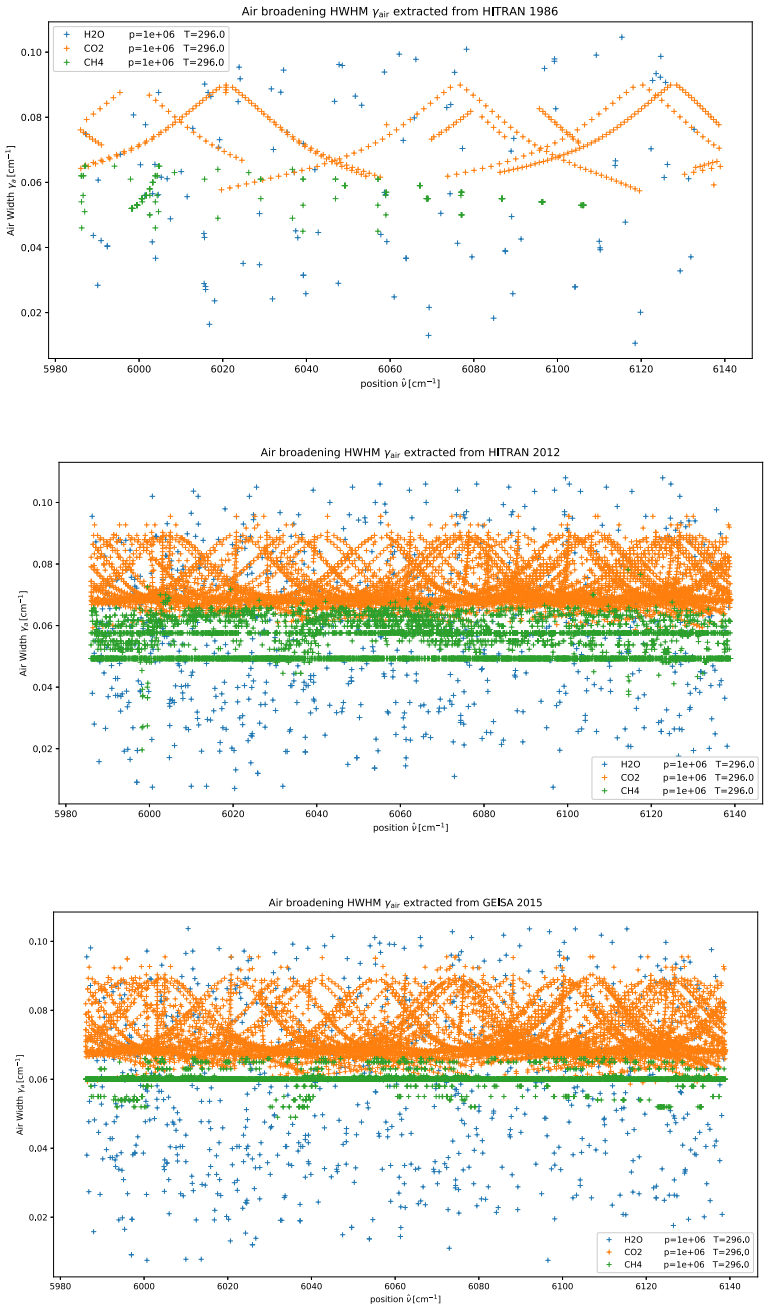

Figure 3.4: Air broadening HWHM of the spectral lines in the first spectral interval for CH_4, CO_2 and H_2O, which are extracted from HITRAN 1986, HITRAN 2012 and GEISA 2015 databases.

Table 3.3: The range of air broadening HWHM γ_{air} [cm^{-1}] for different molecules extracted from three databases.

	HITRAN 1986	HITRAN 2012	GEISA 2015
CH_4	$[4.5{\cdot}10^{-2}, 6.5{\cdot}10^{-2}]$	$[2.0{\cdot}10^{-2}, 7.8{\cdot}10^{-2}]$	$[4.9{\cdot}10^{-2}, 6.6{\cdot}10^{-2}]$
CO_2	$[5.7{\cdot}10^{-2}, 9.0{\cdot}10^{-2}]$	$[5.9{\cdot}10^{-2}, 9.6{\cdot}10^{-2}]$	$[5.9{\cdot}10^{-2}, 9.6{\cdot}10^{-2}]$
H_2O	$[1.1{\cdot}10^{-2}, 1.0{\cdot}10^{-1}]$	$[7{\cdot}10^{-3}, 1.1{\cdot}10^{-1}]$	$[7{\cdot}10^{-3}, 1.0{\cdot}10^{-1}]$

the sum of the layer optical depths of the three molecules, using the line parameters provided by the databases and a coarse 20 layer version of the US Standard Atmosphere. The optical depth τ is closely related to monochromatic transmission $\mathcal{T}$ and absorption cross section k_m of molecule m (refers to Eq. (2.9)). In the first fitting window for retrieval ($5986-6139\,\text{cm}^{-1}$), the largest value of the optical depth for CH_4 is around 1.6 achieved by HITRAN 1986, the maximal optical depth for the new databases is around 1.4, which are approximately located at $6060\,\text{cm}^{-1}$. The distinct optical depths for the methane molecule are evenly distributed over the range between $6000 - 6115\,\text{cm}^{-1}$. Additionally, different from HITRAN 2012 and GEISA 2015, the optical depth for CH_4 only exists within $6106\,\text{cm}^{-1}$ for HITRAN 1986. For CO_2, the curves of the optical depths calculated with HITRAN 2012 and GEISA 2015 are quite similar. Overall, the result from HITRAN 1986 is larger than the other two datasets. The largest value of the optical depth in HITRAN 1986 is around 0.23 which is located at $6090\,\text{cm}^{-1}$, however for HITRAN 2012 and GEISA 2015 the peak value amounts 0.18. Water vapor is distributed throughout the complete spectral range and the information on optical depths are in good agreement for all three databases. In generally, the calculated optical depth with respect to these three databases conforms to each other. Compared to the most recently released versions HITRAN 2012 and GEISA 2015, the result from the old version HITRAN 1986 shows some differences.

For the second fitting window $6273 - 6419\,\text{cm}^{-1}$, the statistics of line strength, the air broadening HWHM and the number of lines are displayed in Table 3.4. By HITRAN 1986, no spectral lines for methane are identified. The number of lines for CH_4 in HITRAN 2012 is more than twice as many as GEISA 2015. The weakest line strength is detected in HITRAN 2012, which amounts $3.53{\cdot}10^{-30}$. For CO_2, HITRAN 2012 and GEISA 2015 both have more than 6700 lines, which are much more than HITRAN 1986 with 515 lines. The extreme value by the two most recent compilations are similar. For water vapor, only 109 lines are identified by HITRAN 1986 and around 1000 lines by HITRAN 2012 and GEISA 2015. The minimal line strength is $1.58{\cdot}10^{-30}$ by GEISA 2015, and the maximal values for all the three databases are nearly the same. The widest and narrowest air broadening HWHM γ_{air} for CH_4 exsit in HITRAN 2012. For CO_2, γ_{air} of three databases are similar with each other. The γ_{air} of H_2O varies from $5{\cdot}10^{-3}$ to $1.0{\cdot}10^{-1}$ for HITRAN 2012

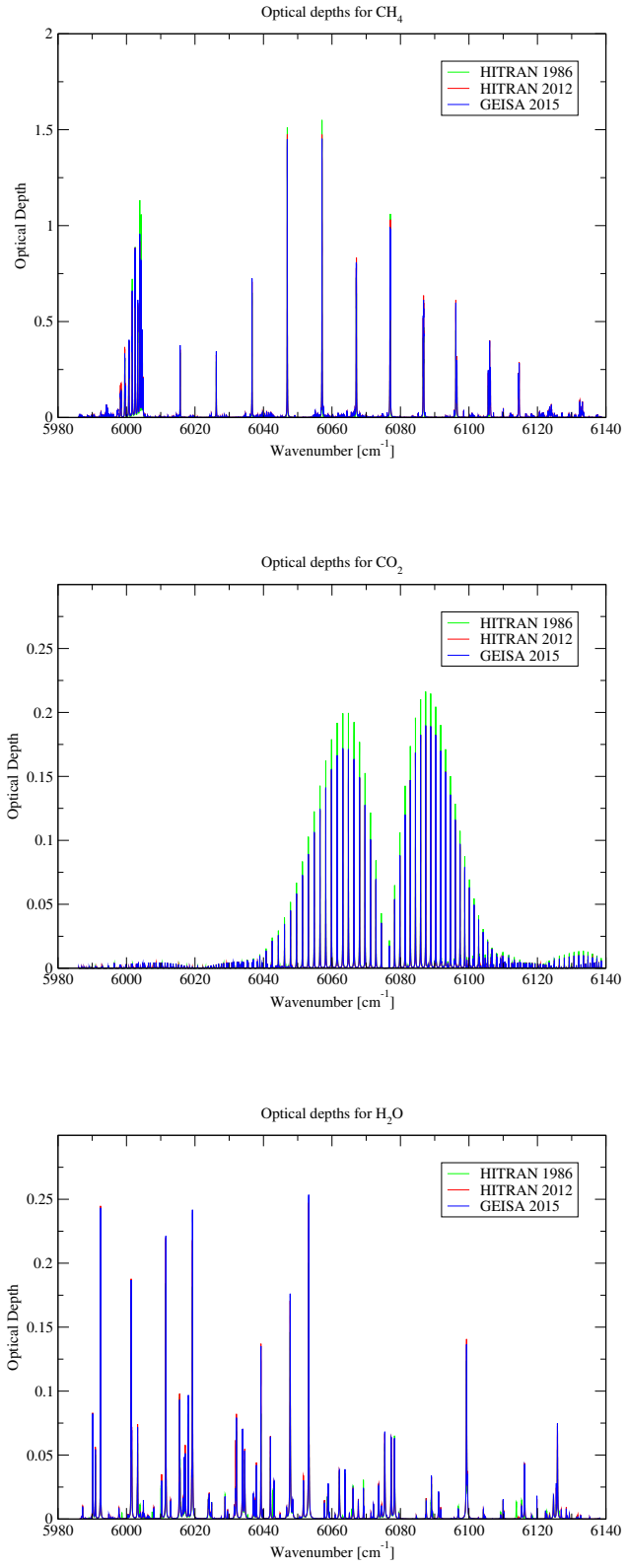

Figure 3.5: Total optical depth for CH_4, CO_2, and H_2O calculated using HITRAN 1986, HITRAN 2012 and GEISA 2015 databases with respect to the first spectral interval.

and GEISA 2015 and from $1.1{\cdot}10^{-2}$ to $9.8{\cdot}10^{-2}$ for HITRAN 1986.

Table 3.4: The number of lines N, the range of line strength S [$\mathrm{cm^{-1}/(molec\ cm^{-2})}$] and air broadening HWHM γ_{air} [$\mathrm{cm^{-1}}$] for different molecules extracted from three databases with respect to the second spectral interval.

	HITRAN 1986	HITRAN 2012	GEISA 2015
N			
CH_4	0	7447	3574
CO_2	515	6742	6965
H_2O	109	1020	981
S			
CH_4	0	$[3.53{\cdot}10^{-30}, 1.16{\cdot}10^{-25}]$	$[2.4{\cdot}10^{-29}, 1.16{\cdot}10^{-25}]$
CO_2	$[3.7{\cdot}10^{-27}, 1.77{\cdot}10^{-23}]$	$[1{\cdot}10^{-30}, 1.74{\cdot}10^{-23}]$	$[1{\cdot}10^{-30}, 1.77{\cdot}10^{-23}]$
H_2O	$[3.01{\cdot}10^{-27}, 3.63{\cdot}10^{-25}]$	$[1{\cdot}10^{-29}, 3.95{\cdot}10^{-25}]$	$[1.58{\cdot}10^{-35}, 3.95{\cdot}10^{-25}]$
γ_{air}			
CH_4	0	$[3.7{\cdot}10^{-2}, 7.1{\cdot}10^{-2}]$	$[4.8{\cdot}10^{-2}, 6.6{\cdot}10^{-2}]$
CO_2	$[5.6{\cdot}10^{-2}, 9.0{\cdot}10^{-2}]$	$[5.9{\cdot}10^{-2}, 9.6{\cdot}10^{-2}]$	$[5.9{\cdot}10^{-2}, 9.6{\cdot}10^{-2}]$
H_2O	$[1.1{\cdot}10^{-2}, 9.8{\cdot}10^{-2}]$	$[5{\cdot}10^{-3}, 1.1{\cdot}10^{-1}]$	$[5{\cdot}10^{-3}, 9.9{\cdot}10^{-2}]$

The optical depth for the three molecules with repect to the second fitting window are displayed in Fig. 3.6. Compared with the first fitting window, the optical depth for CH_4 in the range of wavenumber 6273 to 6419 $\mathrm{cm^{-1}}$ is extremely small, that is revealed by all the three databases. The optical depth for CO_2 has a high value over the spectral range of 6300 to 6380 $\mathrm{cm^{-1}}$. The curve of optical depth have one maximal crest value which ranges to 1.9 located at 6360 $\mathrm{cm^{-1}}$ by GEISA 2015. Same as the first spectral interval, the values of optical depth for water vapor are variable along the wavenumbers, mostly are under 0.05.

According to the figures of optical depth, it can be found that the contribution of methane to the measured radiance is high in the first spectral interval but low for the second interval. CO_2 is dominant for the radiance in the second spectral range and as an interfering gas in the first spectral range. Water contributes along the whole range of the spectra with a low level of value. These findings are consilient with the analysis of altitude sensitivity in Sect. 3.1.

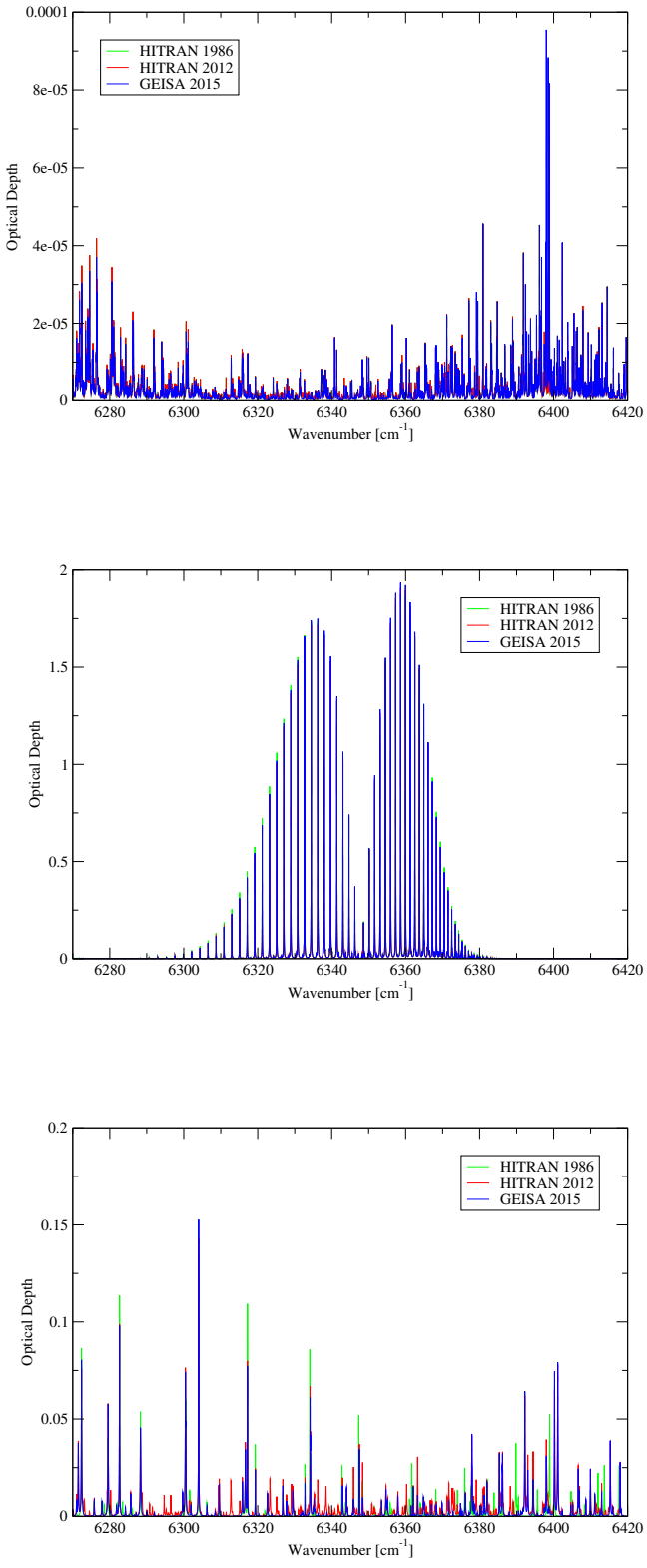

Figure 3.6: Total optical depth for CH_4, CO_2, and H_2O calculated using HITRAN 1986, HITRAN 2012 and GEISA 2015 databases with respect to the second spectral interval.

Chapter 4

SCIAMACHY Channel 6 Data Retrieval

The following chapters show the result of the methane retrieval using different input parameters such as spectroscopic database. For the purpose of revealing the impact of different databases on the retrieval results, three databases are used for the investigation, HITRAN 1986, HITRAN 2012 and GEISA 2015. In this way the comparison is made between HITRAN and GEISA and the earliest version of spectroscopic database HITRAN 1986 is chosen as a contrast for the two most recent compilations whose line parameters are similar. The retrieval of SCIAMACHY channel 6 observations is proceeded in two cases: orbit 8663 and the Sahara region, respectively. Furthermore, the retrieval work towards to the simulated GOSAT observation is also presented.

4.1 Retrieval Analysis: Orbit 8663

4.1.1 VCD Analysis

The observed signal for the trace gas CH_4 (or CO) in the SWIR spectra is not strong enough for retrieving an altitude dependent concentration profile. Therefore, the vertical column density VCD (introduced in Sect. 1.4) which provides the total concentration right above the footpoint (the point on the Earth's surface the satellite is looking at) is analysed as the final product. It is an useful and directly interpretable information on the distribution and concentration of trace gases.

In SCIAMACHY the orbit is divided into so called "states" which form the smallest functional sequence of measurements and each state has a certain amount of observed spectra. Fig. 4.1 shows the orbit 8663 measured on 27 October 2003, which is taken as the first retrieval object. The green cells in the picture are nadir-viewing states observed by SCIAMACHY. One state in orbit 8663 may consist of 57 to 416 observation spectra.

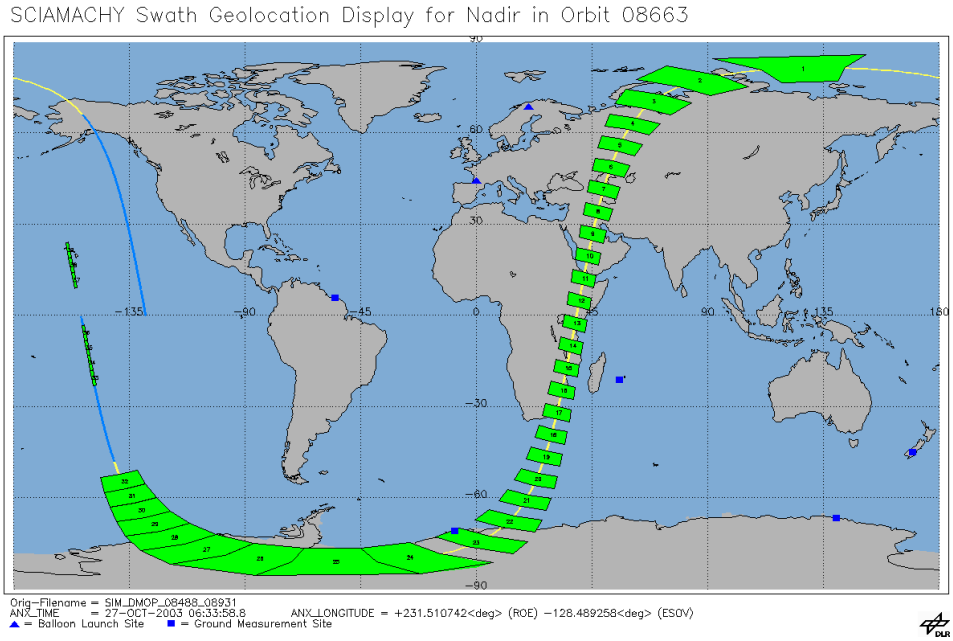

Figure 4.1: Nadir states of SCIAMACHY Orbit 8663, 27 October 2003 (Credit: `http://atmos.caf.dlr.de/projects/scops/`.)

Fig. 4.2(a) shows the vertical column densities of CH_4 at different latitudes calculated by BIRRA using the spectroscopic databases HITRAN 1986, HITRAN 2012 and GEISA 2015. It can be seen that the VCD values are well distributed along the latitudes. According to the statistics, 99 % of the values lie in the interval of $0-10\cdot10^{19}$ molecules cm^{-2}. A small number of negative VCD values, occupying only 0.38 %, have no physical meaning. They are generated by the numerical calculation during the inversion process. It can be found with interest, that all the negative VCD values show up only for certain latitudes, e.g. around $+70°$, $+20°$, $-35°$ and $-75°$. The areas corresponding to these latitudes on the orbit 8663 are state No. 3, 10, 17 and 23, respectively. The common point of these states is the mixed terrain. As Fig. 4.1 shows, in state No. 3, 10 and 17 there are land and ocean and No. 23 state is in the Antarctica, which is a mixture of ice and land. Because of the albedo difference between land, ocean or ice, it can lead to an uncertainty of the albedo value by retrieval, consequently an inaccurate result like negative values. This assumption can be also verified by the retrieval coefficients of the albedo quadratic polynomial, the reflectivity coefficients of different order terms are quite variable in the polar region. Fig. 4.3 gives an example of the result of three albedo polynomial coefficients, using HITRAN 2012. The results for the remaing two databases are similar.

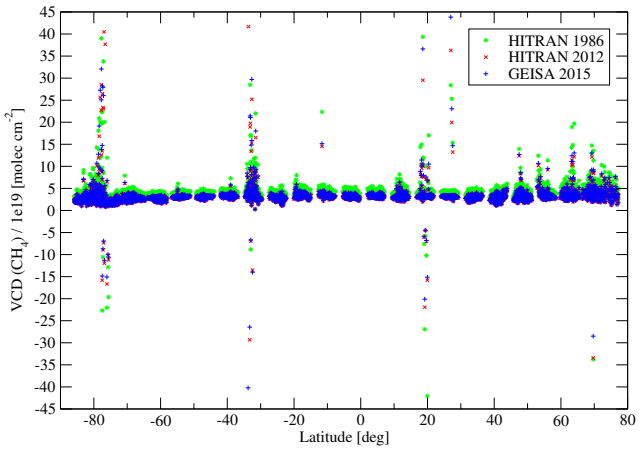

(a)

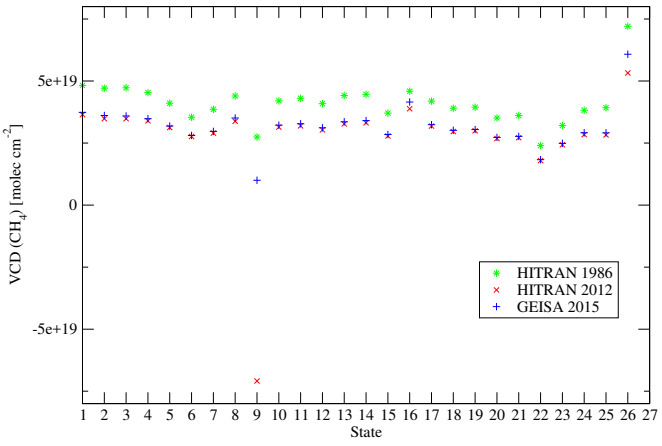

(b)

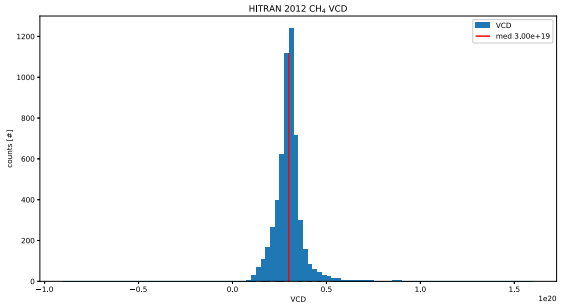

(c)

Figure 4.2: CH_4 VCD retrieval data for orbit 8663 using spectroscopic data from HITRAN 1986, HITRAN 2012 and GEISA 2015. (a) VCD data with respect to the latitude. (b) Average VCD values of different states in orbit 8663. (Note: State 1-12 are in the Northern Hemisphere,13-26 locate in the South.) (c) Histogram of the VCD using HITRAN 2012.

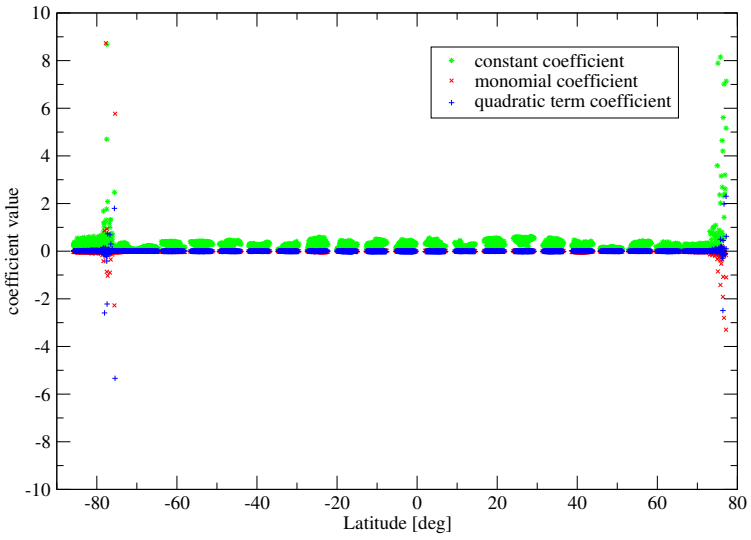

Figure 4.3: Retrieval albedo coefficients of different order terms with respect to the latitudes using HITRAN 2012.

According to the degree of overlap of the VCD value, the retrieval results using HITRAN 2012 and GEISA 2015 show a very high similarity. The results from HITRAN 1986 are higher in comparison with the two latest versions with respect to the same latitude. It is really interesting, that the HITRAN 1986 yield the results which are always higher. The high VCD is derived from the big number density of CH_4. From Eq. (2.11) and (2.12), the radiative transfer equation is associated with the product of line strength S and the number density n. For the same retrieval, the two parameters are inversely proportional. Taking a closer look at the line parameter comparison in Sect. 3.3, the CH_4 line strength listed in HITRAN 1986 is much weaker than HITRAN 2012 and GEISA 2015. This can be the reason for the enhancement of the VCD yielded by HITRAN 1986.

The distribution of individual VCD values retrieved from single spectra has large influence of noise. Fig. 4.2(b) displays the average VCD value for each observation state, giving a more meaningful illustration. In orbit 8663 26 states are measured. The view of the average value shows the distribution of the retrieval results more clearly. On the one hand, the level of VCD for CH_4 which floats around $3.0 \cdot 10^{19}\,\mathrm{molecules\,cm^{-2}}$ is stable along the states of orbit 8663. State 26 with latitude around $-80°$ shows elevated CH_4 concentrations. On the other hand, it also reveals that the retrieval results using HITRAN 1986 are higher than the other two databases.

Fig. 4.2(c) shows a histogram exemplified by the HITRAN 2012 result. Statistics shows that 97 % of the results are located in the range of $0 - 5 \cdot 10^{19}$ molecules cm^{-2} by HITRAN 2012, 96 % by GEISA 2015 and 90 % by HITRAN 1986. The median value of the distribution is indicated with a red line and amounts to $3.0 \cdot 10^{19}$ molecules cm^{-2}. The remaning two histograms look alike and are therefore not displayed. The minimum and maximum values locate further from the median for the three databases, which is also indicated by the range of the distributions listed in Table 4.1.

Table 4.1: Minimum, maximum, median and mean VCD values of orbit 8663 are shown for each spectroscopic databases.

Database	Minimum	Maximum	Median	Mean
HITRAN 1986	$-2.55 \cdot 10^{22}$	$1.49 \cdot 10^{21}$	$3.99 \cdot 10^{19}$	$4.00 \cdot 10^{19}$
HITRAN 2012	$-1.15 \cdot 10^{21}$	$4.17 \cdot 10^{20}$	$3.00 \cdot 10^{19}$	$2.68 \cdot 10^{19}$
GEISA 2015	$-1.51 \cdot 10^{21}$	$5.61 \cdot 10^{20}$	$3.06 \cdot 10^{19}$	$3.07 \cdot 10^{19}$

4.1.2 Residual Analysis: The Norm Residuals

This subsection aims at investigating the norm of the residuals. The residual indicates the difference between the model spectra after the iterative calculation and the real measured spectra. The norm of the residual vector is defined as:

$$\|\boldsymbol{r}\| = \sqrt{\sum_{i=1}^{m} \left(y_i - \boldsymbol{F}(\boldsymbol{x})_i\right)^2}\,, \tag{4.1}$$

where y is the measured spectral radiation intensity, $\boldsymbol{F}(\boldsymbol{x})$ denotes the spectra derived from the forward model and m represents the number of sampling points in the spectral interval of interest. It is an important quality feature to evaluate the retrieval calculations, i.e. the smaller it is the better the retrieval results are assumed to be. For a short notation, the norm of residuals will be abbreviated by normRes or it will just be called residual in the following.

Fig. 4.4(a) shows the results of residuals achieved by using the three spectroscopic databases HITRAN 1986, HITRAN 2012 and GEISA 2015 with respect to the latitudes. From the figure, it can be seen that the residuals calculated by the HITRAN 2012 and GEISA 2015 databases are overlapped in a high percentage. On the contrary, the values yielded by HITRAN 1986 are obviously bigger than the others, which are represented by the green stars. According to this point, it can be concluded that HITRAN 2012 and GEISA 2015 as the spectroscopic input have a better

retrieval result than the HITRAN 1986. Taking a closer look between the two most recent versions of the databases, out of total 5591 data points 4617 (83 % of them) have a smaller residuum derived from GEISA 2015. In other words, GEISA 2015 yields the best residuals results from the point of view of norm residuals, HITRAN 2012 next, finally HITRAN 1986. These findings are supported by Fig 4.4(b) as well, the view of state average values indicates that HITRAN 2012 and GEISA 2015 have much better retrieval performance than HITRAN 1986.

Furthermore, the residuals are generally smaller at Arctic and Antarctic latitudes, which can be seen at both ends of the residual exhibition. In the tropical and temperate zone the values are somewhat higher. In the polar region of the Earth the composition of the atmosphere is more stable than the mid-latitudes and the Equator. Compared with the tropic and subtropic region, the polar atmosphere is relatively dry. The equatorial climate is more humid and the atmosphere contains more water vapor. Retrievals in a humid atmosphere are always somewhat more difficult because of the large variability of H_2O concentrations, even on a "local" scale (e.g. within a SCIAMACHY state). This distinction can explain the bigger residuals in the tropical and temperate zone. On the other hand, in October the sun is somewhere in the South, hence the solar zenith angle (SZA) is smaller for the southern states and larger for the northern states. For this reason the radiation signal is weaker for the northern states, that results in the difficulty by retrieval. In Fig. 4.4, it can be seen that larger residuals exist in the north.

Taking GEISA 2015 as an example of three databases, Fig. 4.4(c) shows the histogram of the residuals, which indicates the distribution of the values. Table. 4.2 gives a overview of minimal, maximal, median and mean values of the residuals.

Table 4.2: Minimum, maximum, median and mean residual values of orbit 8663 are shown for each spectroscopic databases.

Database	Minimum	Maximum	Median	Mean
HITRAN 1986	$6.88 \cdot 10^{-4}$	$1.37 \cdot 10^{-2}$	$3.83 \cdot 10^{-3}$	$4.32 \cdot 10^{-3}$
HITRAN 2012	$6.99 \cdot 10^{-4}$	$8.18 \cdot 10^{-3}$	$2.81 \cdot 10^{-3}$	$2.94 \cdot 10^{-3}$
GEISA 2015	$6.93 \cdot 10^{-4}$	$8.07 \cdot 10^{-3}$	$2.79 \cdot 10^{-3}$	$2.91 \cdot 10^{-3}$

4.1.3 Error Analysis

The retrieval error of the proxy normalized vertical column density for CH_4 (errVCD) is derived from the errors of the scaling factors α_{CH_4} (errCH_4) and α_{CO_2} (errCO_2),

$$\text{errVCD} = N_{CH_4}^{\text{prior}} \times \frac{\text{err}CH_4 \cdot \alpha_{CO_2} + \text{err}CO_2 \cdot \alpha_{CH_4}}{\alpha_{CO_2}^2} \ . \tag{4.2}$$

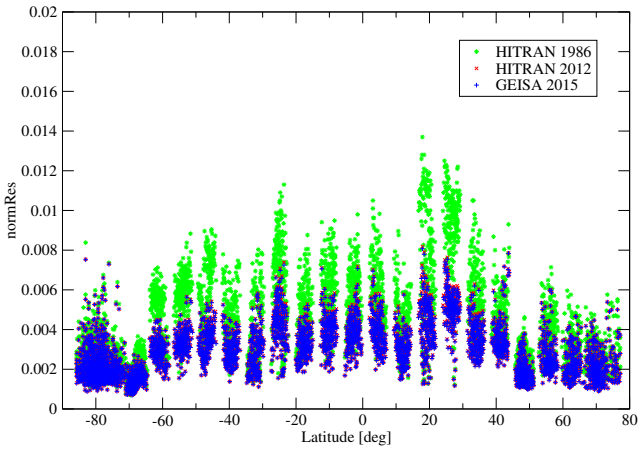

(a)

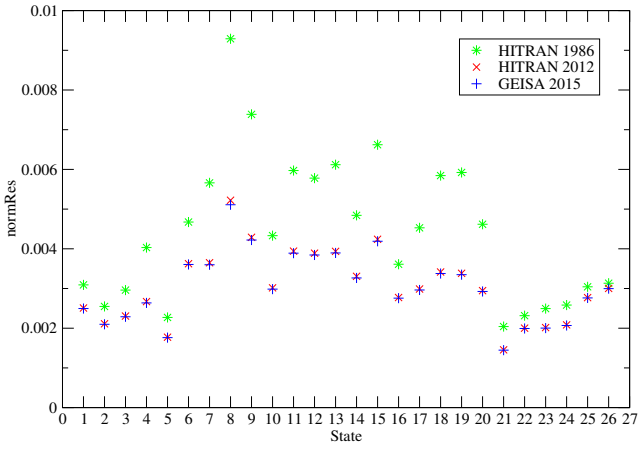

(b)

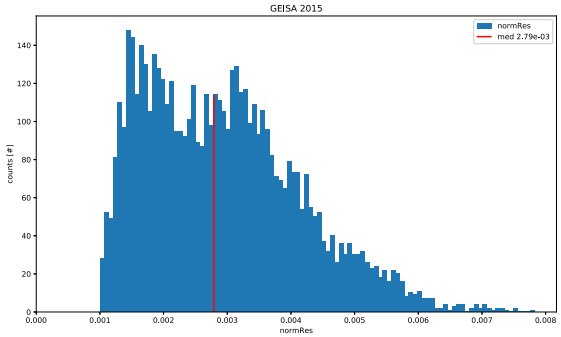

(c)

Figure 4.4: Norm of residuals by CH_4 retrieval for orbit 8663 using spectroscopic data from HITRAN 1986, 2012 and GEISA 2015. (a) Residuals with respect to latitude. (b) Average residual values of different states in orbit 8663. (Note: State 1-12 are in the Northern Hemisphere,13-26 locate in the South.) (c) Histogram of the retrieval residuals using GEISA 2015.

The errCH$_4$ and errCO$_2$ are obtained from the diagonal elements of the least squares covariance matrix defined by [Gimeno García et al., 2011],

$$\text{error}\,\varepsilon_{\text{i}} = \sqrt{\text{cov}_{\text{ii}}} \qquad \text{with} \quad \text{cov} = \left(J^T\,J\right)^{-1}\,, \tag{4.3}$$

where J denotes the Jacobian, and cov is for the covariance matrix with dimensions $n \times n$. The error is another quality feature for the retrieval.

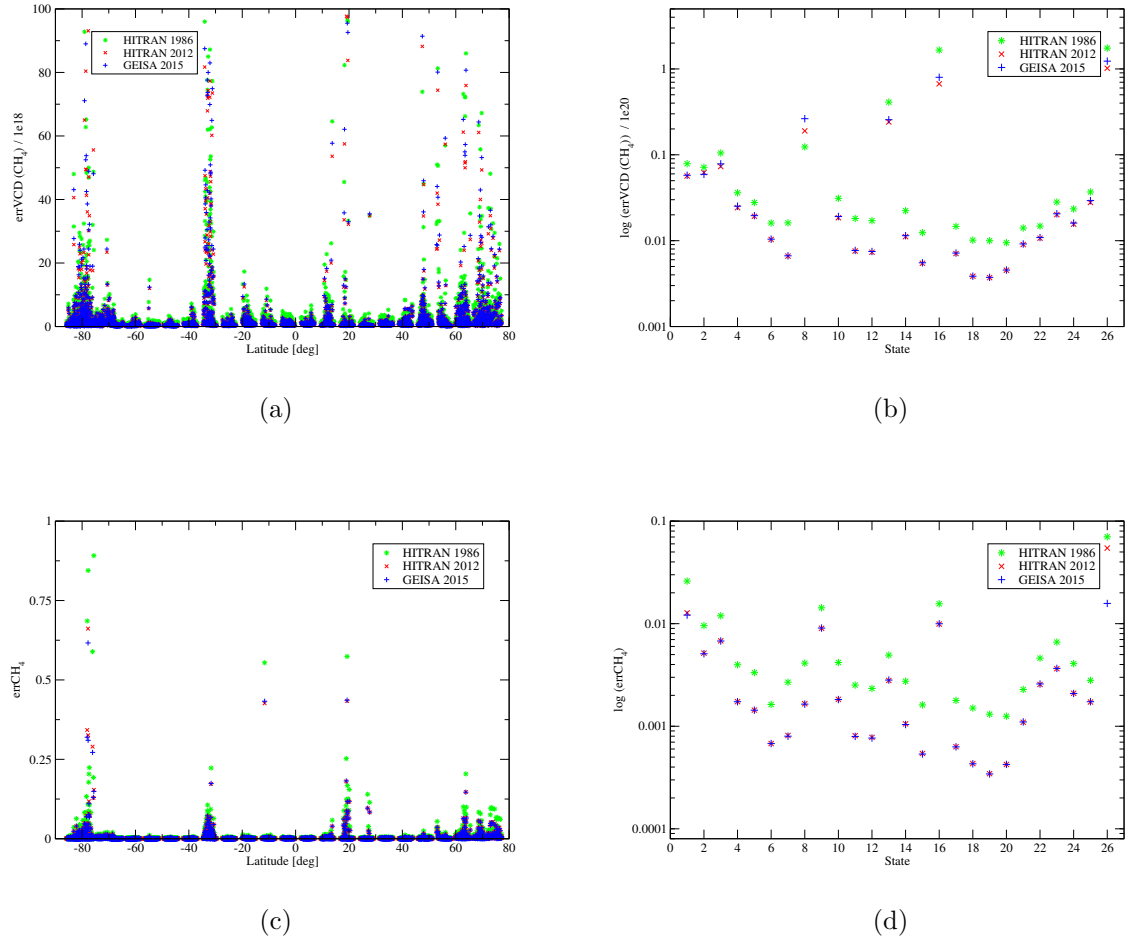

Figure 4.5: Retrieval errors of CH$_4$ VCD (errVCD) and scaling factor α_{CH_4} (errCH$_4$) for orbit 8663. (a) errVCD versus latitude. (b) Average errVCD values of different states in orbit 8663. (c) errCH$_4$ versus latitude. (d) Average errCH$_4$ values of different states in orbit 8663.

Fig. 4.5(a) shows the errors of VCD for CH$_4$, the distribution of all the values shows some dependency on the latitudes. Errors become large and variable at the same latitude bands as for the negative VCD values in Fig. 4.2(a), e.g. between $-35°$ and

$-30°$, $10°$ and $20°$ and the poles (around $-80°$ and $+80°$). For the average values shown in the Fig. 4.5(b), the levels of states No. 9, 16 and 26 which correspond to the latitudes mentioned before are much higher than the others. Fig. 4.5(c) displays the errors of the scaling factor α_{CH_4}. The values are generally quite small, approaching zero, which indicates the good retrieval performance for the α_{CH_4}. With the help of the view of the average values with logarithmic y-axis on the right side, it can be seen that states No. 1, 9, 16, 26 have bigger errors. Within the three databases, the results for HITRAN 1986 reveals the largest errors for both errVCD and errCH_4. Comparing the two lastest data versions, 69 % of the errVCD values calculated with HITRAN 2012 are smaller than GEISA 2015. For the errCH_4, GEISA 2015 provides smaller retrieval errors in general, 66 % of them are lower than HITRAN 2012.

The following diagrams exhibit the retrieval errors of the scaling factor α_{CO_2} (errCO_2) and α_{H_2O} (errH_2O) for the orbit 8663. Fig. 4.6(a) and Fig. 4.6(b) give the information on errCO_2. Except several data at certain latitudes (around $-35°$ and $+20°$), the level of the errCO_2 is stable. The states No. 9, 16 and 26 have higher average values and the others are all under 0.1. The diagrams in the second row are with regard to errH_2O. The retrieval error for water vapor is stable over the large latitude range. There is a peak value between $-80°$ and $-70°$, corresponding to the states from No. 22 to 26. By comparison, in contrast to errVCD and errCH_4, HITRAN 1986 shows a closer similarity with HITRAN 2012 and GEISA 2015 for errCO_2 and errH_2O. According to the distribution shown in the plots, the retrieval errors by HITRAN 1986 are still the biggest overall. In comparison with the other two databases, out of total 5591 error data for scaling factor CO_2 there 5571 from GEISA 2015 (almost 100 %) are smaller. However, 95 % of errH_2O derived from HITRAN 2012 are smaller than GEISA 2015.

4.1.4 Scaling Factor Analysis

The molecular scaling factor $\boldsymbol{\alpha}$ are estimated by nonlinear least squares fit. The retrieved scaling factors for methane α_{CH_4}, carbon dioxide α_{CO_2} and water vapor α_{H_2O} as well as the ratio of methane to carbon dioxide $\alpha_{CH_4}/\alpha_{CO_2}$ (see Eq. 2.43) are investigated.

After the retrieval with the spectroscopic databases HITRAN 1986, HITRAN 2012 and GEISA 2015 respectively, the average scaling factors of the orbit states are displayed in the Fig. 4.7. The x axis corresponds to the mean latitude of each state. For the scaling factor of methane, HITRAN 2012 and GEISA 2015 have an analogous distribution. HITRAN 1986 yields bigger values overall. The lowest value is at latitude $-80°$ near the south pole, whereas the highest one is at latitude $+20°$ corresponding to the state No. 11, which locates in east Africa. In general, α_{CH_4} is relatively low near the two poles of the Earth and has an increase in the tropic and

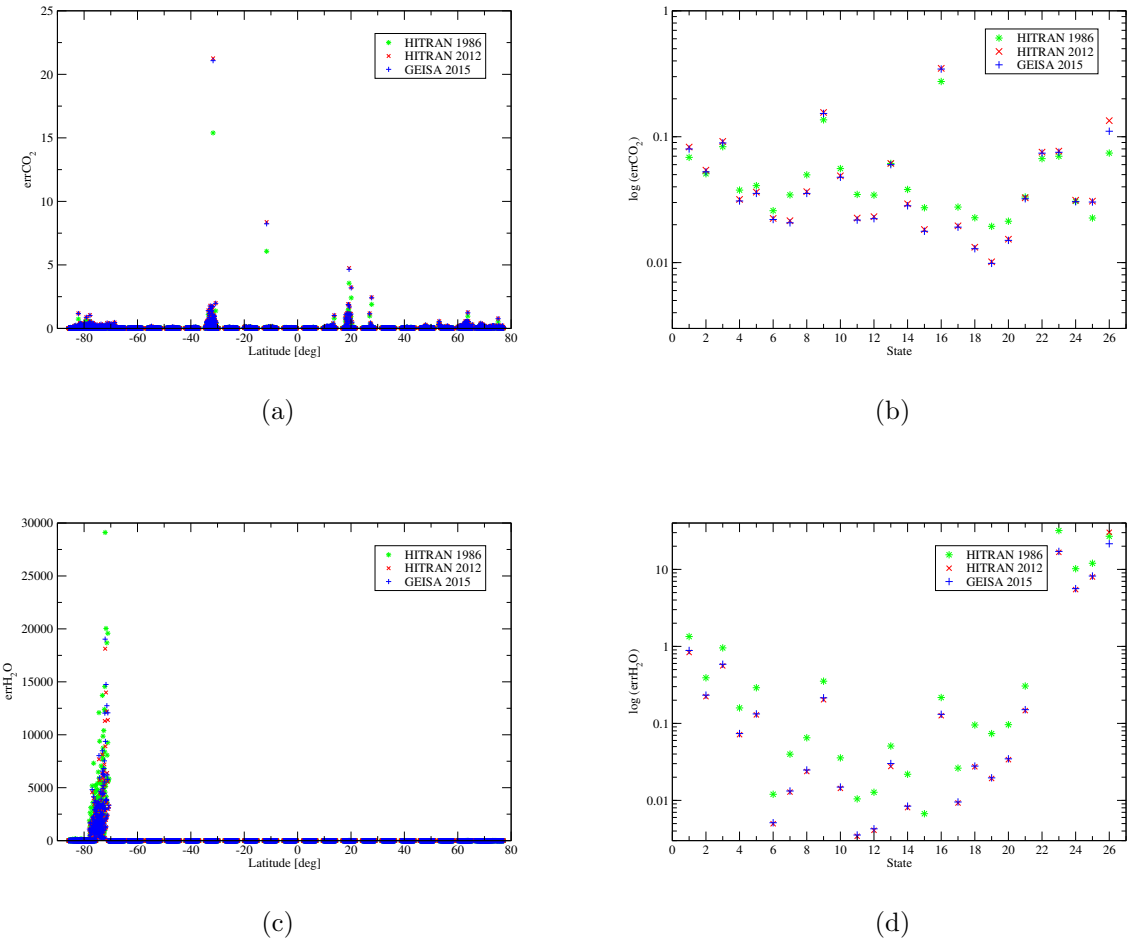

(a) (b)

(c) (d)

Figure 4.6: Retrieval errors of scaling factor α_{CO_2} ($errCO_2$) and α_{H_2O} ($errH_2O$) for orbit 8663. (a) $errCO_2$ versus latitude. (b) Average $errCO_2$ values of different states in orbit 8663. (c) $errH_2O$ versus latitude. (d) Average $errH_2O$ values of different states in orbit 8663.

subtropic region where the majority of sources creating methane emissions exist. The average scaling factor for carbon dioxide in the polar regions is lower than the mid-latitude and equatorial areas except at latitude around $-70°$. From another point of view, the highest level of the average α_{CO_2} is yielded by HITRAN 2012, GEISA 2015 in the next place and lastly HITRAN 1986. According to Eq. 4.2 for errVCD calculation, the reason why the errors of VCD yielded by HITRAN 2012 is smaller than GEISA 2015 can be attributed to the larger scaling factor α_{CO_2}.

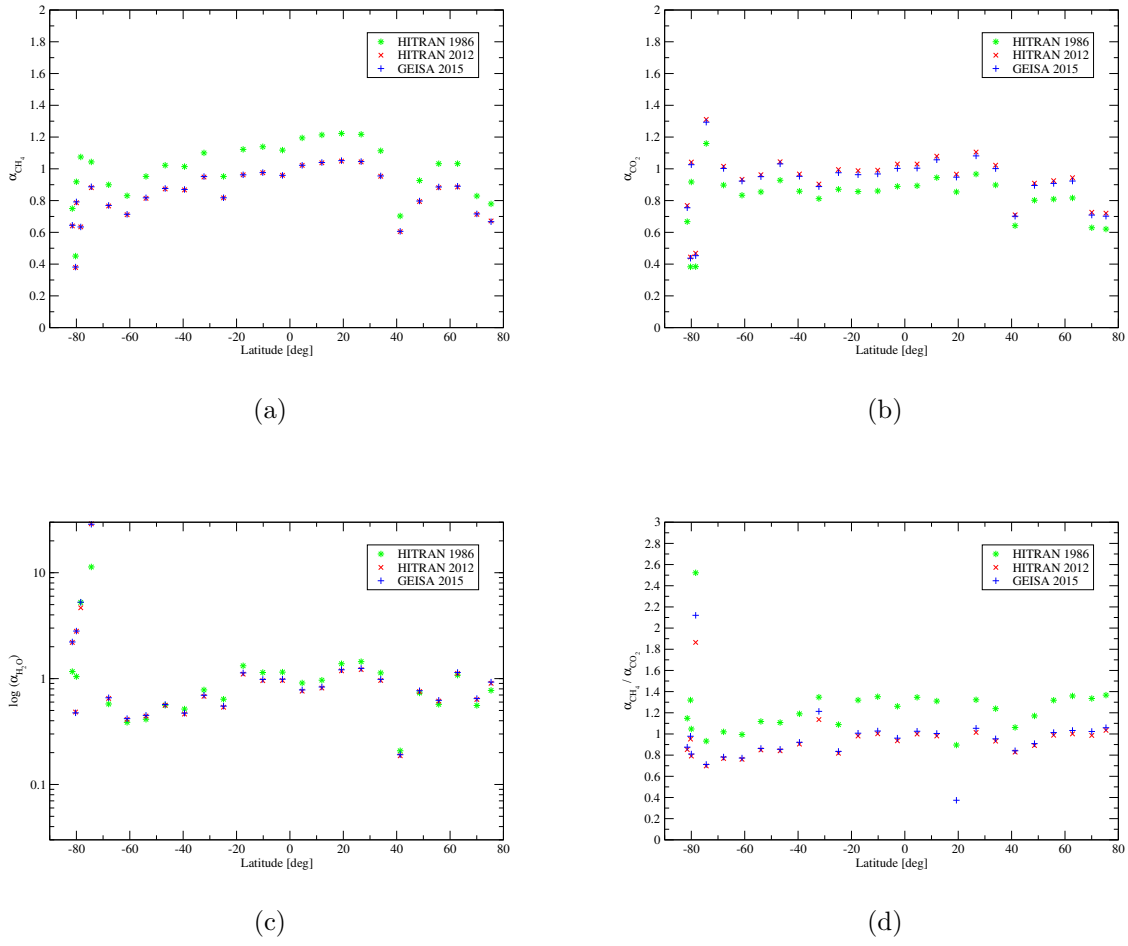

Figure 4.7: Average scaling factors of different latitudes by CH_4 retrieval for orbit 8663 using HITRAN 1986, HITRAN 2012 and GEISA 2015. (a) Average α_{CH_4}. (b) Average α_{CO_2}. (c) Average α_{H_2O}. (d) Average value of ratio of methane to carbon dioxide $\alpha_{CH_4}/\alpha_{CO_2}$.

The average scaling factor of water reveals that high values locate at the latitude between $-80°$ and $-70°$. α_{H_2O} yielded by the three spectroscopic databases are

close to each other. Except one state locating around $-80°$, the level of the ratio $\alpha_{CH_4}/\alpha_{CO_2}$ is generally stable, floating between 0.6 to 1.2. HITRAN 1986 has a higher level than HITRAN 2012 and GEISA 2015, which corresponds with the retrieved VCD result.

Conclusion

Concerning the impact of the spectroscopic databases to the retrieval performance of the orbit 8663 observed by SCIAMACHY, a conclusion can be drawn according to above analysis. Table 4.3 summarizes the comparisons between the three databases with respect to several aspects, namely norm residuals, retrieval error for the methane VCD, retrieval error for the scaling factor of CH_4, retrieval error for the scaling factor of CO_2, and retrieval error for the scaling factor of H_2O.

Table 4.3: Mark for the spectroscopic database which achieves the most data with the smallest value for the normRes, errVCD, errCH_4, errCO_2 and errH_2O.

Database	norm residuals	errVCD	errCH_4	errCO_2	errH_2O
HITRAN 1986					
HITRAN 2012		•			•
GEISA 2015	•		•	•	

According to the Table 4.3, the retrieval processed with HITRAN 2012 and GEISA 2015 have relatively better performance. For the estimation of the norm residuals, errCH_4 and errCO_2, the database GEISA 2015 achieves the lowest values upon most occasions. HITRAN 2012 yields the lowest errVCD and errH_2O most often. Because of the same retrieval settings except for the different spectroscopic data inputs, from the experiment results it can be concluded that the spectral line data has great impact on the trace gases retrieval. On the other hand, it also proves that a more recently released version of the database can be considered as a factor to achieve a better retrieval performance. Due to the advanced laboratory techniques and improved theoretical knowledge, more weak lines are identifiable in the new spectroscopic database. For instance, as mentioned in Sect. 3.3 in HITRAN 1986 much less spectral lines of the trace gases with weak line strength are identified in the spectral range than the other two databases.

4.2 Retrieval Analysis: Sahara Region

The investigation on the methane retrieval is also performed towards to a specific region of the Earth. The Sahara desert, which is characterized as a relatively homogeneous terrain with the high surface reflectivity due to the landform of sand and rock, has been chosen as the test object. Because of the proximity to the equator, observations are characterized by small solar zenith angles (SZA). Furthermore, it is expected to be largely free of clouds on account of the desert climate. These two conditions lead to more solar insolation and hence a higher signal to noise ratio.

The observation data measured by SCIAMACHY within a period of one month (October 2003) is utilized for the analysis. Compared with the retrieval for orbit 8663, there are much more calculations. That is why a variety of quality criteria are fulfilled at first in order to extract the useful data among a large amount of retrieval results. The investigated area for the Sahara covers longitudes from -5° to 27° and latitudes from 18° to 30°. At last 65 states in total are extracted from the data. Furthermore, retrievals with high fit errors are rejected (typically error of scaling factor for CH_4: $0 < \mathrm{err}CH_4 < 0.01$). Because of the inferior position of the HITRAN 1986 in the orbit analysis mentioned in the previous section, only HITRAN 2012 and GEISA 2015 are used for the retrieval. The spatial distributions of the fit products include the VCD for CH_4, the norm residuals, the scaling factors for CH_4, CO_2 and H_2O and the corresponding errors are investigated. For a meaningful illustration the average value of the investigated parameters with respect to each orbit state recorded in the Sahara region is taken into consideration.

4.2.1 VCD Analysis

As Fig. 4.8 shows, the retrieved methane vertical column densities are relatively homogenous above the Sahara. The x-axis corresponds to the mean latitude of each state. The latitudinal variation is not as strong as for the orbit 8663. The VCD values are distributed in the range of $2.5 - 3.5 \cdot 10^{19}$ molecules cm^{-2}. It can be seen in both of the plots that GEISA 2015 yields bigger values than HITRAN 2012 on average. Table 4.4 gives the information on extreme, median and mean values.

Table 4.4: Minimum, maximum, median and mean VCD values of the Sahara region are shown for each spectroscopic databases.

Database	Minimum	Maximum	Median	Mean
HITRAN 2012	$2.64 \cdot 10^{19}$	$3.91 \cdot 10^{19}$	$2.93 \cdot 10^{19}$	$2.98 \cdot 10^{19}$
GEISA 2015	$2.69 \cdot 10^{19}$	$4.01 \cdot 10^{19}$	$2.99 \cdot 10^{19}$	$3.05 \cdot 10^{19}$

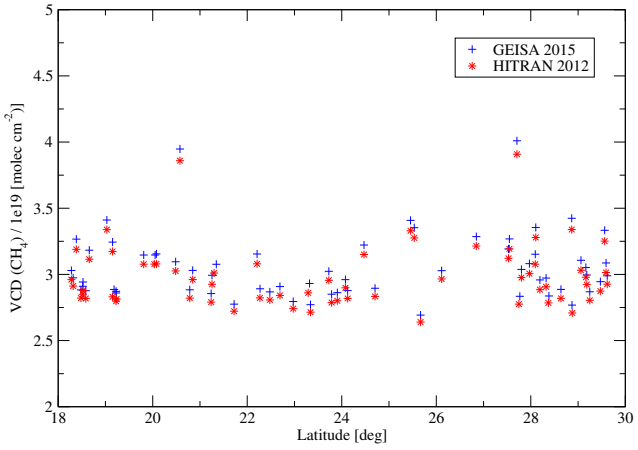

(a)

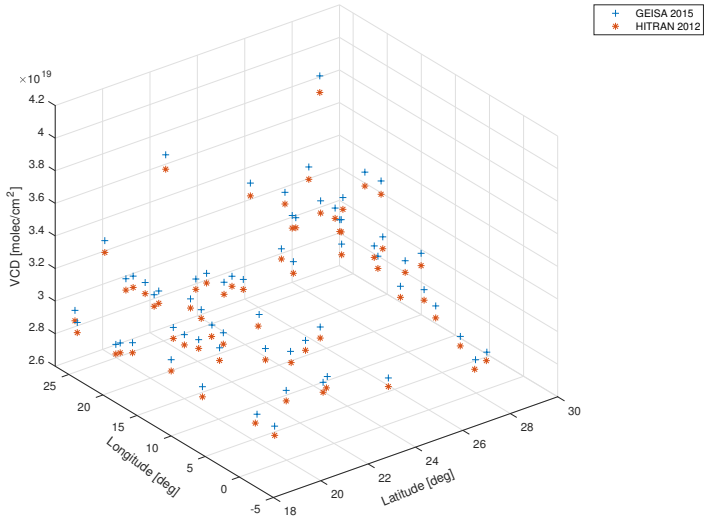

(b)

Figure 4.8: CH_4 VCD retrieval data for the Sahara region using HITRAN 2012 and GEISA 2015. (a) Average VCDs with respect to the mean latitude of 65 states. (b) 3D plot for the spatial distribution for average VCDs of 65 observed states in the Sahara.

4.2.2 Residual Analysis: The Norm Residuals

The spatial distribution of the norm residuals is displayed in Fig. 4.9. Similar to the orbit analysis, the residuals yielded by HITRAN 2012 and GEISA 2015 are close to each other. As Table 4.5 shows, the maximum, minimum, median and mean values of the norm residuals yielded by GEISA 2015 are smaller than HITRAN 2012. And 88% of all the average residuals yielded by GEISA 2015 are lower by comparing them point by point with HITRAN 2012. It can be concluded, that GEISA 2015 has a superiority in retrieval performance with respect to the norm residuals.

Table 4.5: Minimum, maximum, median and mean residual values for the Sahara region are shown for each spectroscopic database.

Database	Minimum	Maximum	Median	Mean
HITRAN 2012	$4.32 \cdot 10^{-3}$	$1.69 \cdot 10^{-2}$	$6.34 \cdot 10^{-3}$	$7.04 \cdot 10^{-3}$
GEISA 2015	$4.24 \cdot 10^{-3}$	$1.69 \cdot 10^{-2}$	$6.25 \cdot 10^{-3}$	$6.97 \cdot 10^{-3}$

4.2.3 Error Analysis

In analogy to Sect. 4.1.3, Fig. 4.10 indicates that the retrievals using HITRAN 2012 and GEISA 2015 produce similar errors. As compared to the GEISA 2015 results, about half of the VCD errors using HITRAN 2012 are smaller. The proportion of smaller errors of α_{CH_4}, α_{CO_2}, and α_{H_2O} using HITRAN 2012 are 45 %, 42 %, and 51 %, respectively. In conclusion, both spectroscopic databases HITRAN 2012 and GEISA 2015 perform very well as demonstrated by the retrieval errors, which would be fundamental for a reliable methane retrieval. Table 4.6 gives the information on the median values for the errors of the scaling factor.

Table 4.6: Median values of the retrieved errors of VCD and scaling values for α_{CH_4}, α_{CO_2}, α_{H_2O} for the Sahara region using the spectroscopic databases HITRAN 2012 and GEISA 2015.

Database	errVCD	errCH_4	errCO_2	errH_2O
HITRAN 2012	$4.02 \cdot 10^{17}$	$5.93 \cdot 10^{-4}$	$1.56 \cdot 10^{-2}$	$6.34 \cdot 10^{-3}$
GEISA 2015	$3.91 \cdot 10^{17}$	$5.80 \cdot 10^{-4}$	$1.46 \cdot 10^{-2}$	$6.72 \cdot 10^{-3}$

4.2.4 Scaling Factor Analysis

The analysis of the scaling factor α_m follows the same pattern as the previous parameters. α_{CH_4}, α_{CO_2} and α_{H_2O} as well as the ratio of methane to carbon dioxide $\alpha_{CH_4}/\alpha_{CO_2}$ are analyzed. The results are plotted and shown in Fig. 4.11.

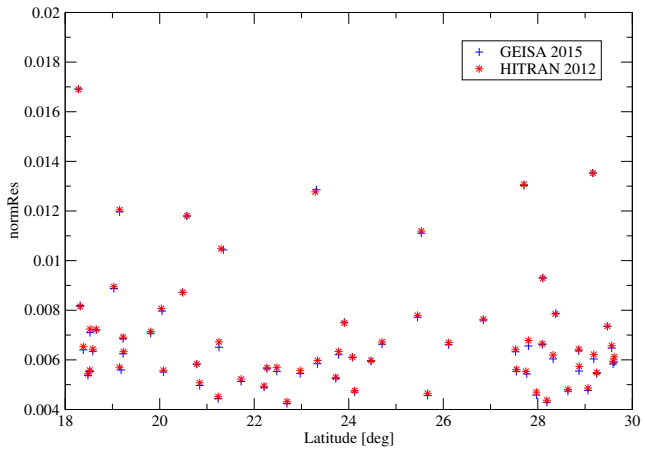

(a)

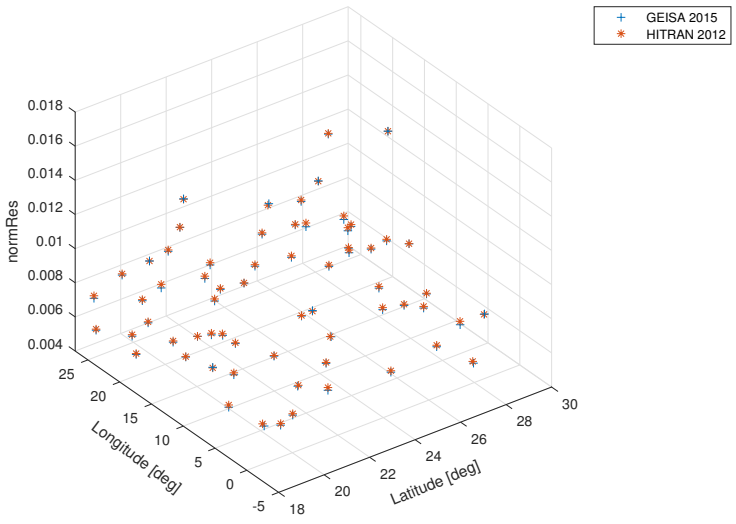

(b)

Figure 4.9: Norm of residuals for the CH_4 retrieval for the Sahara region using HITRAN 2012 and GEISA 2015. (a) Average residuals with respect to the mean latitude of 65 states. (b) 3D plot for the spatial distribution for average residuals of 65 observed states in the Sahara.

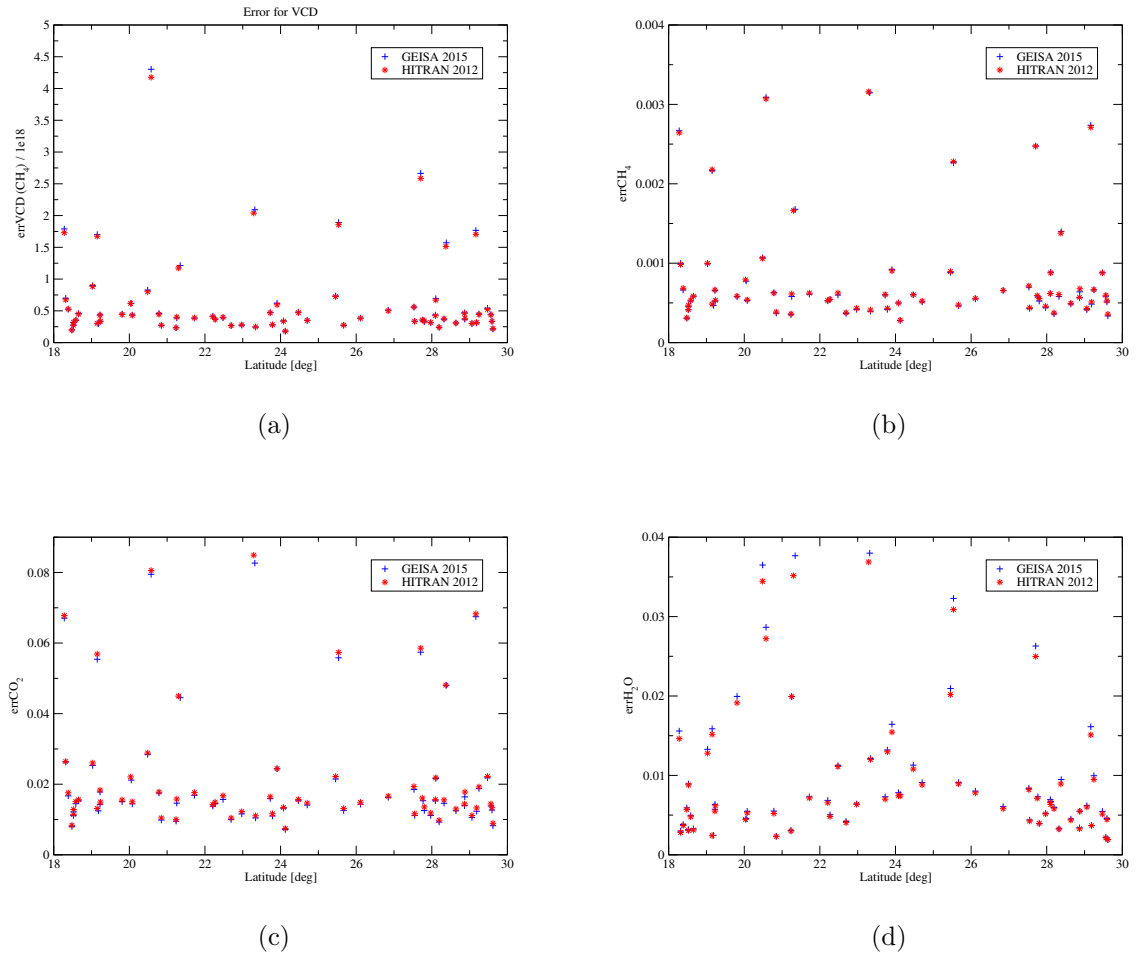

Figure 4.10: Errors versus latitude by CH_4 retrieval in the Sahara region using HITRAN 2012 and GEISA 2015. (a) Average errVCD. (b) Average errCH_4. (c) Average errCO_2. (d) Average errH_2O.

As Table 4.7 shows, for HITRAN 2012 the value of α_{CH_4} varies from $0.80 - 1.09$. Most of the data are distributed around one. The scaling factor α_{CO_2} for the proxy gas CO_2 has a similar distribution, whose mean value amounts 1.18. With the utilized a-priori volume mixing ratio of CO_2 amounting 330 ppm, the actual VMR of CO_2 can be roughly estimated around 380 ppm. This value is close to the historical monthly mean data at the surface level with the amount of 375 ppm for October 2003. It was measured by the World Data Center for Greenhouse Gases (WDCGG) Assekrem Station, which conducts the air sampling observation at a stationary platform located in the center of the Sahara. The scaling factor in our case does not aim at the retrieval of profile for the VMR, whereas for the VCD. The product of a-priori volume mixing ratio and scaling factor can just provide a rough estimation range, which has no sense for the validation. Water vapor has a large uncertainty in tropical regions and is highly variable. The scaling factor of water is up to 2.15 and goes down to 0.38 somewhere. The values of ratio $\alpha_{CH_4}/\alpha_{CO_2}$ are mostly close to one. The results yielded by GEISA 2015 have no big differences.

On the other hand, the mean scaling factor of the proxy gas CO_2 is 1.18 by HITRAN 2012 and 1.16 by GEISA 2015, which also confirms the assumption of the low cloud coverage above the Sahara. There are only few deviations of a photon path owing to the hindrance like cloud or aerosol in the atmosphere. And the size of ratio $\alpha_{CH_4}/\alpha_{CO_2}$, which varies between 0.8 to 1.2, reflects the fact that the actual vertical column density of CH_4 is close to the a-priori VCD in the Sahara region. It is also resonable, because in a desert there are neither wetland nor other anthropogenic emission source of methane, e.g. biomass burning, rice cultivation and so on.

Table 4.7: Minimum, maximum, median and mean values of the different scaling factors for each spectroscopic database.

	Database	Minimum	Maximum	Median	Mean
α_{CH_4}	HITRAN 2012	0.80	1.09	1.06	1.05
	GEISA 2015	0.80	1.08	1.06	1.05
α_{CO_2}	HITRAN 2012	0.86	1.31	1.20	1.18
	GEISA 2015	0.84	1.29	1.18	1.16
α_{H_2O}	HITRAN 2012	0.38	2.15	0.97	1.03
	GEISA 2015	0.39	2.21	0.99	1.06
$\alpha_{CH_4}/\alpha_{CO_2}$	HITRAN 2012	0.80	1.18	0.87	0.89
	GEISA 2015	0.82	1.21	0.89	0.91

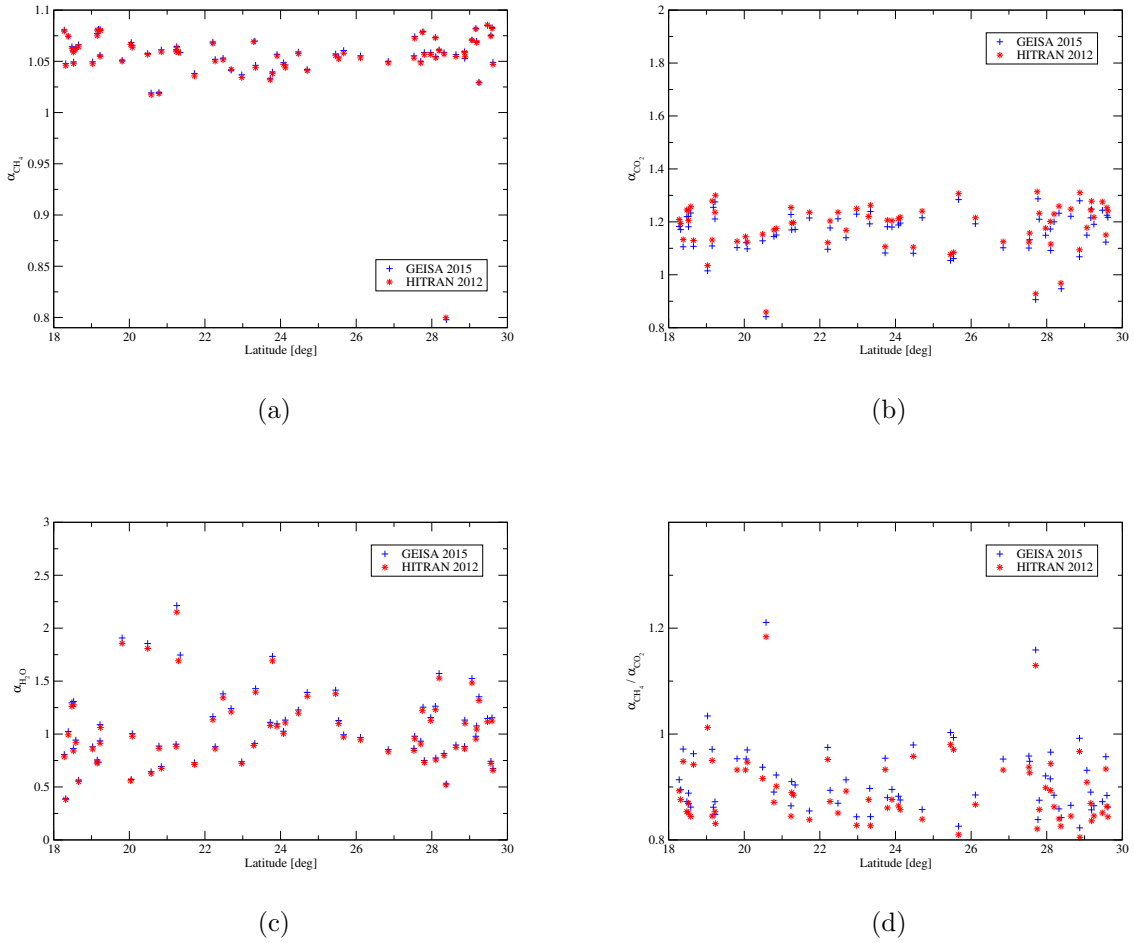

Figure 4.11: Average scaling factors versus latitude for different trace gases. (a) Scaling factor for methane α_{CH_4}. (b) Scaling factor for carbon dioxide α_{CO_2}. (c) Scaling factor for water vapor α_{H_2O}. (d) ratio of methane to carbon dioxide $\alpha_{CH_4}/\alpha_{CO_2}$.

Chapter 5

Simulated GOSAT Data Retrieval

5.1 Simulated GOSAT Observation

Besides SCIAMACHY observation data, the simulated GOSAT data is also used for the retrieval analysis. The Greenhouse Gases Observing Satellite (GOSAT) (see Sect. 1.3) also monitors the methane globally from space using short wave infrared (SWIR) radiance [Kuze et al., 2009].

The instrument response function $\mathrm{sinc}(\nu)$ simulates the smoothing of spectral radiance by the FTS instrument on GOSAT. The atmospheric profile characteristics in terms of mean atmospheric temperature, and concentration for the investigated trace gases (H_2O, CO_2, CH_4) are provided by an ensemble of 42 diverse profiles [Garand et al., 2001]. The first six are standard profiles, namely tropical (tro), mid-latitude summer (mls) and winter (mlw), subarctic summer (sas) and winter (saw), and U.S. standard atmosphere (uss) [Anderson et al., 1986]. The remaining 36 profiles were selected from a bank of profiles defined by Turner [1995]. Profiles 7−18 are ranked by increasing mean (mass weighted) atmospheric temperature. The next 12 (19−30) are ranked by increasing integrated water vapor, the last 12 (31−42) by increasing total ozone. All profiles were defined on 43 standard pressure levels. Lastly, some noise is added to the signal with the signal-to-noise ratio of 1000 (more than 320 according to the GOSAT specification).

Additionally, the geometry parameters used for the simulation are listed in Table 5.1. The satellite is supposed to observe the backscattered sunlight in the nadir viewing geometry. The observation simulation for each atmospheric profile is processed with two solar zenith angles (SZA) 20° and 60°, respectively. Therefore, 84 simulated observation of GOSAT data are obtained in total.

There is one point which needs attention that analysis for the last 12 profiles with increasing total ozone are not displayed, because ozone is irrelevant to the methane retrieval in our spectral range.

Table 5.1: Geometry parameters used for the observation data simulation.

Satellite height	800 km
Earth radius	6368 km
Viewing zenith angle	0°
Solar zenith angle	20° and 60°

The simulated observations are created by means of the spectroscopic database HITRAN 2012 which is responsible for the calculation of the molecular absorption cross section. In order to analyze the impact of molecular absorption spectroscopy data on methane retrieval, the retrievals are conducted with the spectroscopic databases HITRAN 2012 and GEISA 2015, respectively.

Table 5.2 shows the statistics of the number of lines, the range of line strength and air broadening HWHM for CH_4, which are extracted from HITRAN 2012, GEISA 2015 and GOSAT-2014 methane spectral line list [Nikitin et al., 2015]. More specteal lines are detected by HITRAN 2012 in the spectral interval (5900−6200 cm^{-1}) and the lower limit of the line strength by HITRAN 2012 is smaller than GOSAT 2014 line list. Compared to HITRAN 2012, GEISA 2015 has similar line number and line strength range but varies for the air broadening HWHM. Fig. 5.1 displays the cross sections of CH_4, which are calculated by Eq. (2.12). The Voigt line shape function is applied for all. It can be found that the line data from HITRAN 2012 is similar with the actual line data used by GOSAT. From this point, it is reasonable to simulate the GOSAT observations with HITRAN 2012. From the magnified picture (selected for the ν range of 6075−6100 cm^{-1}, k(ν) range of 1−5·10^{-23} cm^2/molec) , it is clear that the cross section of GOSAT line data is slightly smaller than the other two databases.

Table 5.2: The number of lines N, the range of line strength S [cm^{-1}/(molec cm^{-2})] and air broadening HWHM γ_{air} [cm^{-1}] for CH_4 extracted from two databases with respect to the spectral interval (5900−6200 cm^{-1}).

	N	S	γ_{air}
GOSAT line list	4754	[2.0·10^{-25}, 1.52·10^{-21}]	[1.9·10^{-2}, 8.6·10^{-2}]
HITRAN 2012	10207	[1.13·10^{-27},1.5·10^{-21}]	[2.0·10^{-2}, 7.8·10^{-2}]
GEISA 2015	10208	[1.13·10^{-27},1.5·10^{-21}]	[4.9·10^{-2}, 6.6·10^{-2}]

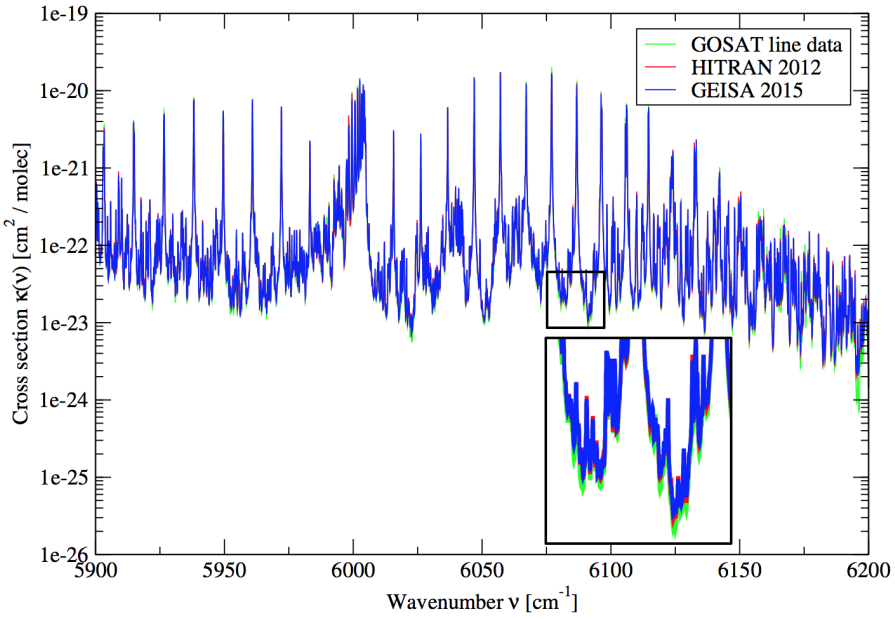

Figure 5.1: Comparison for CH_4 absorption cross section using GOSAT line database, HITRAN 2012 and GEISA 2015.

5.2 Retrieval Analysis: Data Using Standard Atmospheric Profiles

The retrieval of the observations simulated by the set of 6 standard atmospheric profiles is introduced in this section. The atmospheric characteristics of the selected profiles are listed in the Table 5.3. It can be seen, that the CH_4 and CO_2 a-priori estimates are almost identical and the a-priori estimation for H_2O is directly proportional to the integrated water content.

Retrieval Fit Parameter

VCD For CH_4

Fig. 5.2 shows the retrieved result of VCD for methane. The two diagrams represent the results for different solar zenith angles. Among the 12 observations only the retrieval VCD by SZA of 60°, using tropical standard profile as the climatological input data, is smaller yielded by GEISA 2015. For the others GEISA 2015 yielded bigger VCD values than HITRAN 2012. The results have no big variances. The tropical region has the lowest value around 3.50×10^{19} molec/cm^2, the highest VCD of 3.52×10^{19} is in winter of subarctic region. On the other hand, for the same region (mid-latitude, subarctic), the retrieved VCD for winter is higher than summer.

Table 5.3: Atmospheric profile characteristics in terms of mean atmospheric temperature T, integrated water content IWC, integrated ozone amount IOC, and the a-priori vertical column density for the investigated trace gases.

Profile	T_m [K]	IWC [kg/m^2]	IOC [DU]	$N^{\text{prior}}_{\text{CH}_4}$ [molec/cm^2]	$N^{\text{prior}}_{\text{CO}_2}$ [molec/cm^2]	$N^{\text{prior}}_{\text{H}_2\text{O}}$ [molec/cm^2]
1 (tro)	258.3	40.7	276.3	$3.52{\cdot}10^{19}$	$7.69{\cdot}10^{21}$	$1.36{\cdot}10^{23}$
2 (mls)	258.1	29.1	330.5	$3.52{\cdot}10^{19}$	$7.70{\cdot}10^{21}$	$9.70{\cdot}10^{22}$
3 (mlw)	244.6	8.3	373.7	$3.53{\cdot}10^{19}$	$7.71{\cdot}10^{21}$	$2.79{\cdot}10^{22}$
4 (sas)	254.0	21.0	343.5	$3.52{\cdot}10^{19}$	$7.71{\cdot}10^{21}$	$7.02{\cdot}10^{22}$
5 (saw)	237.6	4.1	371.2	$3.54{\cdot}10^{19}$	$7.72{\cdot}10^{21}$	$1.36{\cdot}10^{22}$
6 (uss)	250.4	14.1	340.2	$3.53{\cdot}10^{19}$	$7.70{\cdot}10^{21}$	$4.71{\cdot}10^{22}$

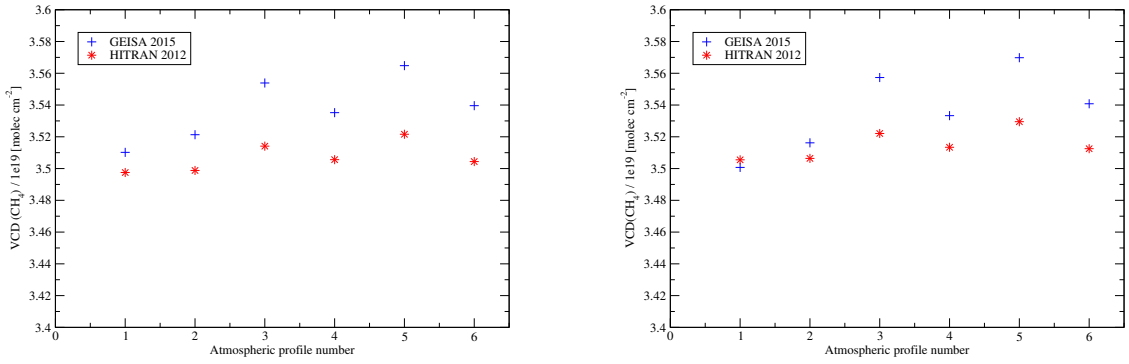

(a) (b)

Figure 5.2: Retrieved CH_4 VCD of simulated GOSAT data using 6 standard atmospheric profiles. (a) VCD result for solar zenith angle 20°. (b) VCD result for solar zenith angle 60°.

The Norm Residuals

As Fig. 5.3 reveals, HITRAN 2012 yielded smaller residuals than GEISA 2015. And the residuals retrieved from the simulated data with SZA of 60° is slightly smaller than data with SZA of 20°. The residuals by HITRAN 2012 has a similar distribution as the VCD result, whereas the residuals by GEISA 2015 become roughly constant.

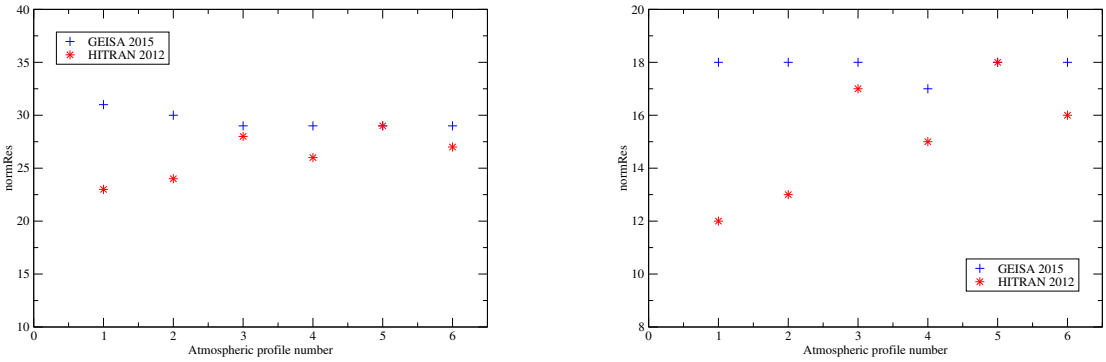

(a) (b)

Figure 5.3: CH_4 retrieval residuals of simulated GOSAT data using 6 standard atmospheric profiles. (a) The norm residuals for solar zenith angle 20°. (b) The norm residuals for solar zenith angle 60°.

Scaling Factor

Fig. 5.4 gives the information on scaling factors of the trace gases. Because of the similarity between the results of SZA 20° and 60°, here we only display the retrieval of the observation with SZA 20°. All the three scaling factors and the ratio retrieved with HITRAN 2012 are stable around 1. The results by GEISA 2015 are slightly floating, however they are also close to 1. The simulated GOSAT observations were created with HITRAN 2012, that is why the retrieved scaling factors of different trace gases yielded by HITRAN 2012 show a steady level of 1, which also reflects the accurate retrieval performance. From the distinction of the retrieved scaling factors, the difference of the two recent released spectroscopic databases can be detected.

Retrieval Error

Fig. 5.5 displays the errors of scaling factors. The errors of the retrieval using HITRAN 2012 are smaller than GEISA 2015. It is predictable because HITRAN 2012 was applied for the observation simulations.

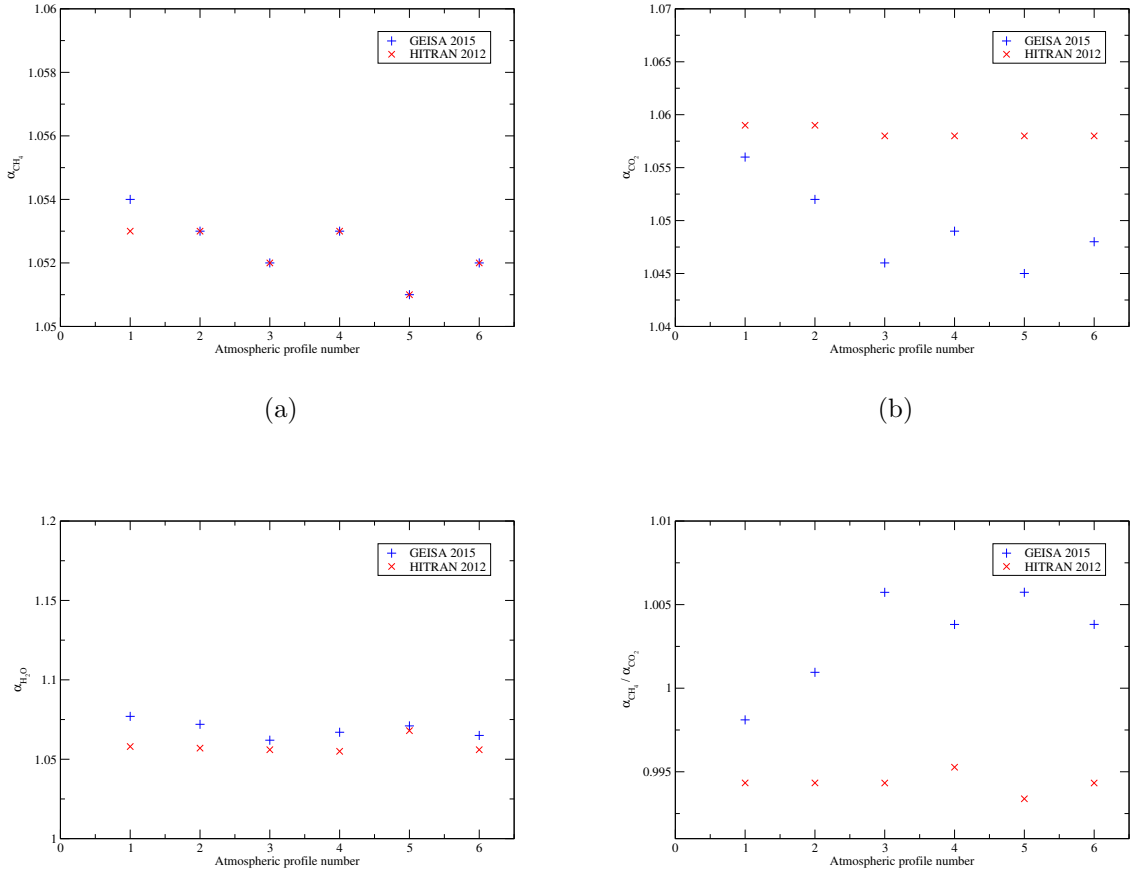

Figure 5.4: Scaling factors versus atmospheric profiles for different trace gases (SZA 20°). (a) Scaling factor for methane α_{CH_4}. (b) Scaling factor for carbon dioxide α_{CO_2}. (c) Scaling factor for water vapor α_{H_2O}. (d) Ratio of methane to carbon dioxide $\alpha_{CH_4}/\alpha_{CO_2}$.

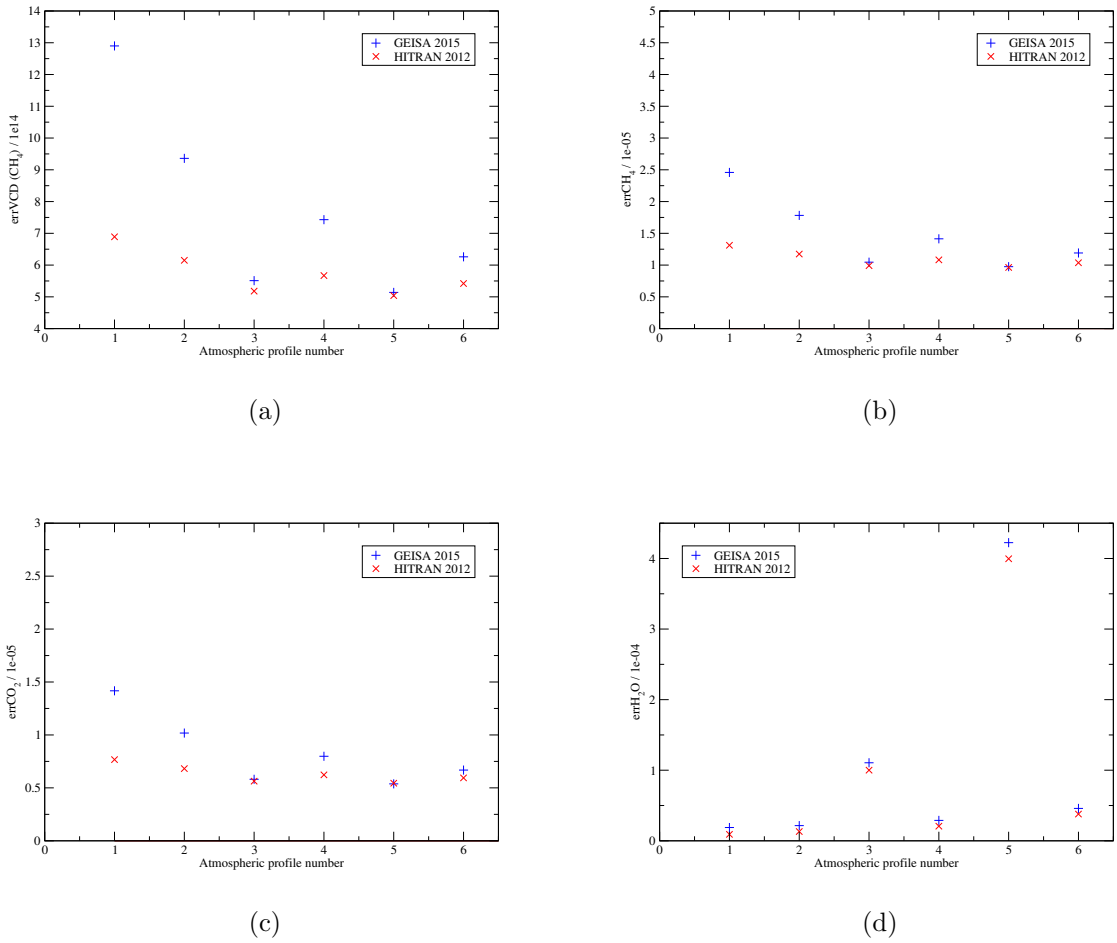

Figure 5.5: Errors versus different atmospheric profiles by CH_4 retrieval using HITRAN 2012 and GEISA 2015. (SZA 20°) (a) Error of VCD. (b) Error of scaling factor α_{CH_4}. (c) Error of scaling factor α_{CO_2}. (d) Error of scaling factor α_{H_2O}.

5.3 Retrieval Analysis: Data Using Atmospheric Profiles With Increasing Temperature

The atmospheric characteristics of the selected profiles are listed in the Table. 5.4. The set of profiles is ranked by increasing mean atmospheric temperature.

Table 5.4: Atmospheric profile characteristics in terms of mean atmospheric temperature T, integrated water content IWC, integrated ozone amount IOC, and the a-priori vertical column density for the investigated trace gases.

Profile	T_m [K]	IWC [kg/m^2]	IOC [DU]	$N_{CH_4}^{prior}$ [molec/cm^2]	$N_{CO_2}^{prior}$ [molec/cm^2]	$N_{H_2O}^{prior}$ [molec/cm^2]
7	227.5	3.1	205.8	$3.56{\cdot}10^{19}$	$7.72{\cdot}10^{21}$	$7.57{\cdot}10^{21}$
8	232.2	0.6	484.0	$3.55{\cdot}10^{19}$	$7.73{\cdot}10^{21}$	$2.08{\cdot}10^{21}$
9	236.8	8.3	334.2	$3.55{\cdot}10^{19}$	$7.71{\cdot}10^{21}$	$1.96{\cdot}10^{22}$
10	238.2	3.0	320.6	$3.5{\cdot}10^{19}$	$7.72{\cdot}10^{21}$	$1.01{\cdot}10^{22}$
11	242.5	7.0	355.7	$3.53{\cdot}10^{19}$	$7.71{\cdot}10^{21}$	$2.34{\cdot}10^{22}$
12	243.1	9.7	343.7	$3.53{\cdot}10^{19}$	$7.70{\cdot}10^{21}$	$3.26{\cdot}10^{22}$
13	246.1	9.9	272.4	$3.53{\cdot}10^{19}$	$7.70{\cdot}10^{21}$	$3.33{\cdot}10^{22}$
14	251.6	15.2	364.1	$3.52{\cdot}10^{19}$	$7.71{\cdot}10^{21}$	$5.09{\cdot}10^{22}$
15	254.0	26.0	262.7	$3.52{\cdot}10^{19}$	$7.70{\cdot}10^{21}$	$8.68{\cdot}10^{22}$
16	256.5	16.6	242.3	$3.52{\cdot}10^{19}$	$7.70{\cdot}10^{21}$	$5.55{\cdot}10^{22}$
17	259.8	51.1	235.9	$3.52{\cdot}10^{19}$	$7.69{\cdot}10^{21}$	$1.70{\cdot}10^{23}$
18	263.9	33.1	271.3	$3.51{\cdot}10^{19}$	$7.69{\cdot}10^{21}$	$1.10{\cdot}10^{23}$

Retrieval Fit Parameter

VCD for CH_4

Fig. 5.6 shows the VCD for CH_4 with respect to the different atmospheric profiles. GEISA 2015 yielded bigger results than HITRAN 2012. The VCD decreases gently along with the increasing mean atmospheric temperature.

The Norm Residuals

Fig. 5.7 displays the norm residuals for the retrieval of these 12 simulated observations. Similar to the previous result, HITRAN 2012 yielded smaller residuals.

Scaling Factor

Fig. 5.8 shows the scaling factor for the trace gases. The values of the three scaling factors are close to 1. The results of α_{CH_4} are similar for different databases HITRAN 2012 and GEISA 2015. GEISA 2015 yielded smaller scaling factor for CO_2 and

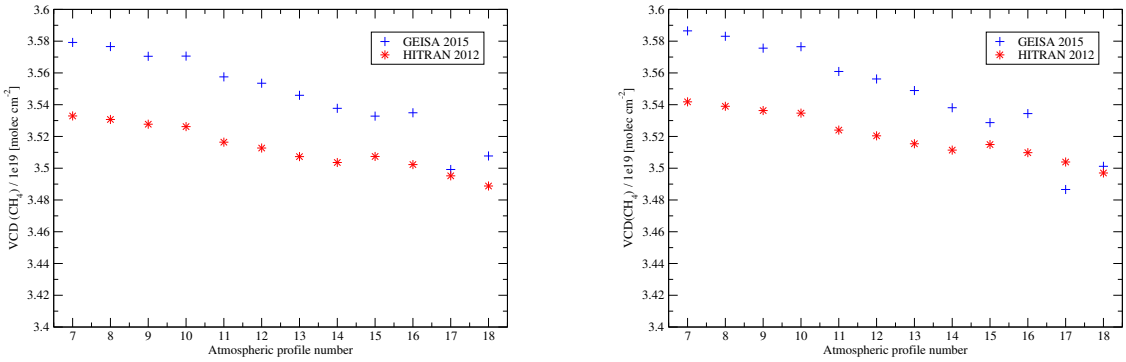

(a) (b)

Figure 5.6: Retrieved CH_4 VCD of simulated GOSAT data using atmospheric profiles No. 7−18. (a) VCD result for solar zenith angle 20°. (b) VCD result for solar zenith angle 60°.

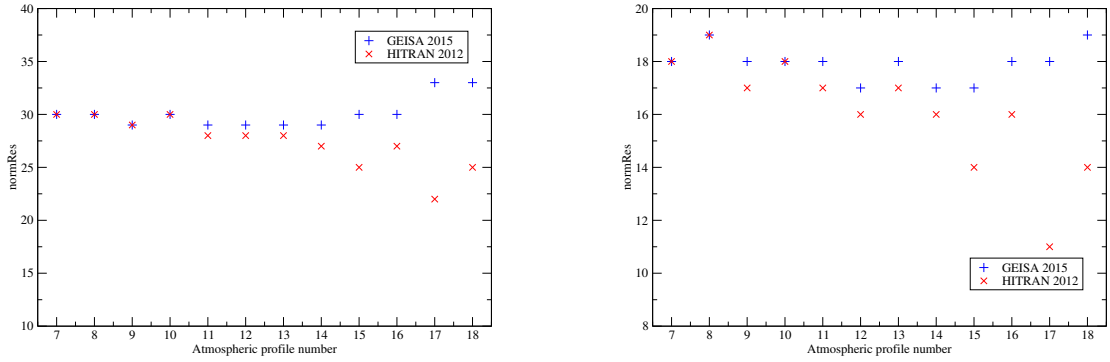

(a) (b)

Figure 5.7: CH_4 retrieval residuals of simulated GOSAT data using atmospheric profiles No. 7−18. (a) The norm residuals for solar zenith angle 20°. (b) The norm residuals for solar zenith angle 60°.

somewhat slightly higher results of α_{H_2O}. For the ratio of methane to carbon dioxide, HITRAN 2012 yielded smaller results.

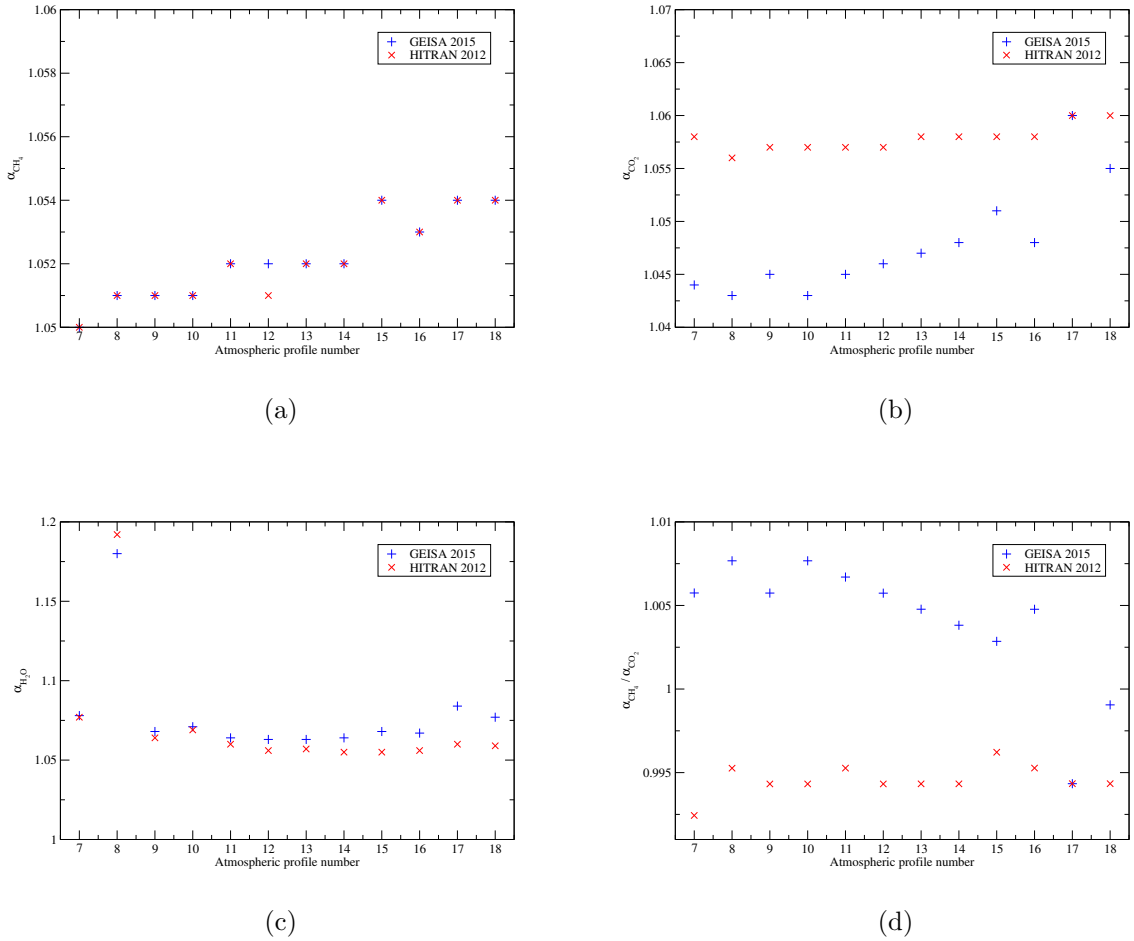

Figure 5.8: Scaling factors versus atmospheric profiles for different trace gases (SZA 20°). (a) Scaling factor for methane α_{CH_4}. (b) Scaling factor for carbon dioxide α_{CO_2}. (c) Scaling factor for water vapor α_{H_2O}. (d) Ratio of methane to carbon dioxide $\alpha_{CH_4}/\alpha_{CO_2}$.

Retrieval Error

Fig. 5.9 displays the errors of scaling factors. The errors of the retrieval using HITRAN 2012 are slightly smaller than GEISA 2015.

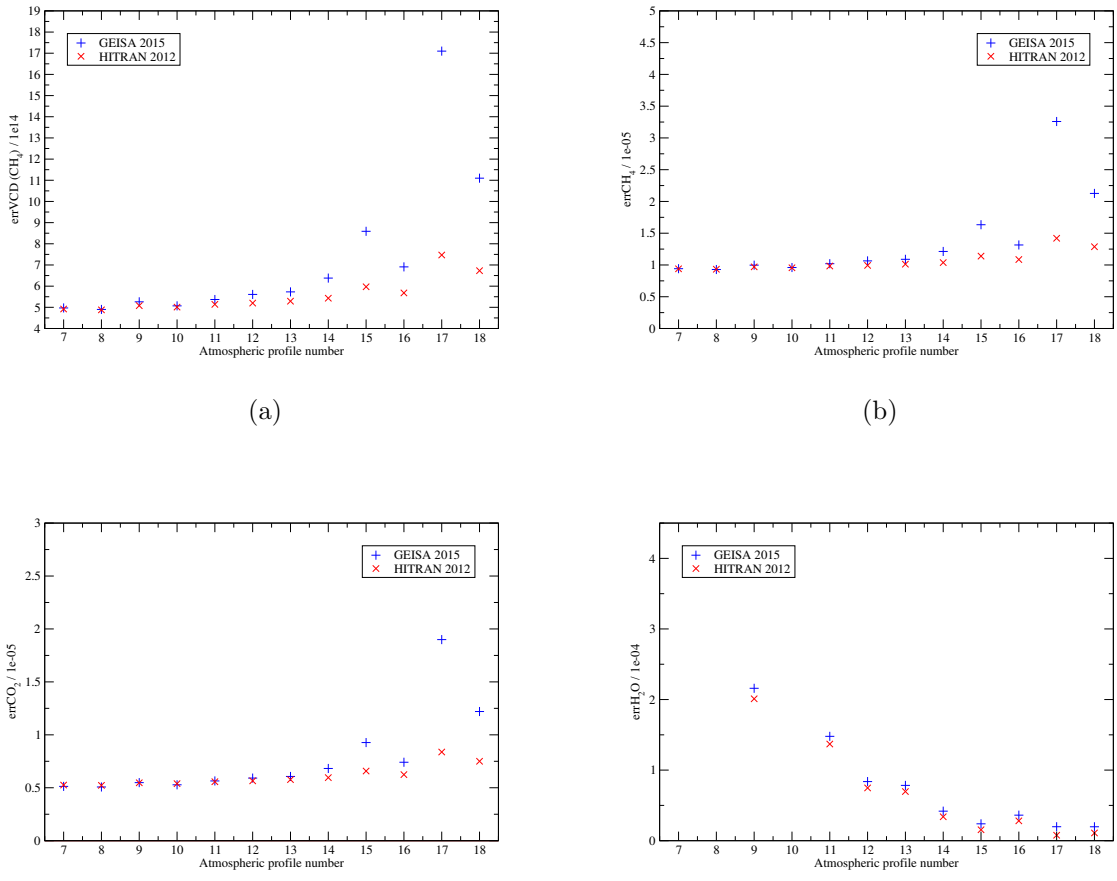

Figure 5.9: Errors versus different atmospheric profiles by CH_4 retrieval using HITRAN 2012 and GEISA 2015. (SZA 20°) (a) Error of VCD. (b) Error of scaling factor α_{CH_4}. (c) Error of scaling factor α_{CO_2}. (d) Error of scaling factor α_{H_2O}.

5.4 Retrieval Analysis: Data Using Atmospheric Profiles With Increasing Integrated Water

The atmospheric characteristics of the selected profiles are listed in the Table 5.5. No. 19−30 profiles are ranked by increasing integrated water vapor.

Table 5.5: Atmospheric profile characteristics in terms of mean atmospheric temperature T, integrated water content IWC, integrated ozone amount IOC, and the a-priori vertical column density for the investigated trace gases.

Profile	T_m [K]	IWC [kg/m^2]	IOC [DU]	$N_{CH_4}^{prior}$ [molec/cm^2]	$N_{CO_2}^{prior}$ [molec/cm^2]	$N_{H_2O}^{prior}$ [molec/cm^2]
19	234.5	2.4	205.8	$3.54{\cdot}10^{19}$	$7.72{\cdot}10^{21}$	$7.86{\cdot}10^{21}$
20	258.1	10.2	484.0	$3.52{\cdot}10^{19}$	$7.70{\cdot}10^{21}$	$3.41{\cdot}10^{22}$
21	248.7	12.9	334.2	$3.53{\cdot}10^{19}$	$7.70{\cdot}10^{21}$	$4.33{\cdot}10^{22}$
22	264.5	19.6	320.6	$3.51{\cdot}10^{19}$	$7.69{\cdot}10^{21}$	$6.54{\cdot}10^{22}$
23	259.5	22.0	355.7	$3.51{\cdot}10^{19}$	$7.69{\cdot}10^{21}$	$7.44{\cdot}10^{22}$
24	255.6	33.9	343.7	$3.52{\cdot}10^{19}$	$7.70{\cdot}10^{21}$	$1.12{\cdot}10^{23}$
25	255.7	37.3	272.4	$3.52{\cdot}10^{19}$	$7.70{\cdot}10^{21}$	$1.24{\cdot}10^{23}$
26	258.2	45.0	364.1	$3.52{\cdot}10^{19}$	$7.70{\cdot}10^{21}$	$1.50{\cdot}10^{23}$
27	259.8	52.2	262.7	$3.51{\cdot}10^{19}$	$7.70{\cdot}10^{21}$	$1.74{\cdot}10^{23}$
28	260.4	59.9	242.3	$3.52{\cdot}10^{19}$	$7.70{\cdot}10^{21}$	$2.0{\cdot}10^{23}$
29	259.2	61.5	235.9	$3.52{\cdot}10^{19}$	$7.70{\cdot}10^{21}$	$2.04{\cdot}10^{23}$
30	260.7	70.9	271.3	$3.51{\cdot}10^{19}$	$7.70{\cdot}10^{21}$	$2.26{\cdot}10^{23}$

Retrieval Fit Parameter

VCD For CH_4

Fig. 5.10 shows the retrieved VCD for the simulated data of the third set of atmospheric profiles. The result yielded by HITRAN 2012 keeps stable along with the increasing concentration of water in the atmosphere, whereas the result yielded by GEISA 2015 shows a slow decrease with increasing water content.

The Norm Residuals

Fig. 5.11 illustrates that HITRAN 2012 yielded smaller residuals than GEISA 2015.

Scaling Factor

As Fig. 5.12 shows, α_{CH_4} ranging from 1.051 to 1.056 presents a gentle increase with increasing IWC. α_{CO_2} is stable for HITRAN 2012 and increases from 1.042 to 1.065 for GEISA 2015. α_{H_2O} for both databases is stable around 1. For the ratio

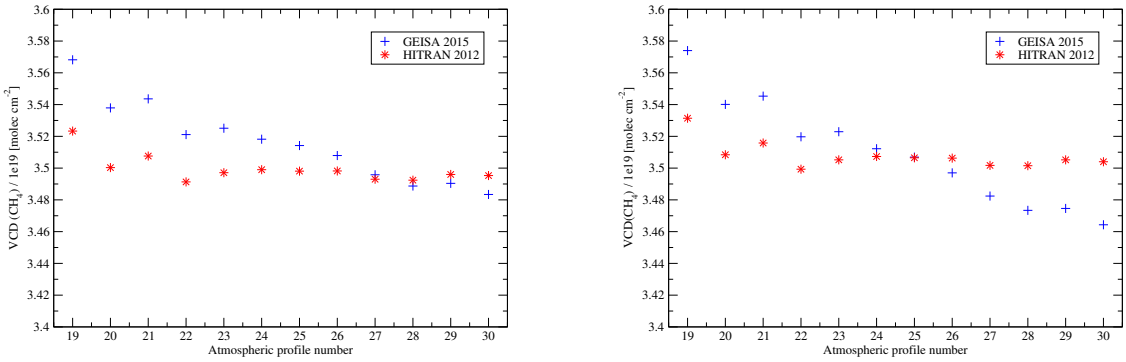

(a) (b)

Figure 5.10: Retrieved CH_4 VCD of simulated GOSAT data using atmospheric profiles No. 19−30. (a) VCD result for solar zenith angle 20°. (b) VCD result for solar zenith angle 60°.

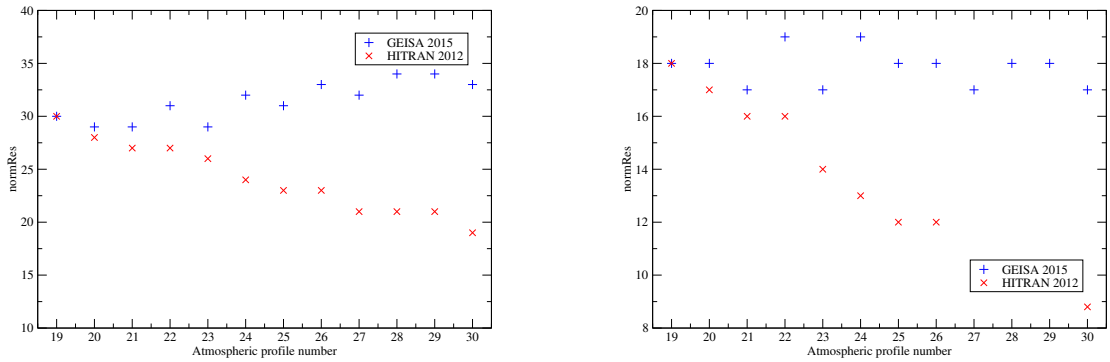

(a) (b)

Figure 5.11: CH_4 retrieval residuals of simulated GOSAT data using atmospheric profiles No. 19−30. (a) The norm residuals for solar zenith angle 20°. (b)The norm residuals for solar zenith angle 60°.

of methane to carbon dioxide $\alpha_{CH_4}/\alpha_{CO_2}$, the ratio by HITRAN 2012 is floating around 0.995. For GEISA 2015 it shows a downward trend.

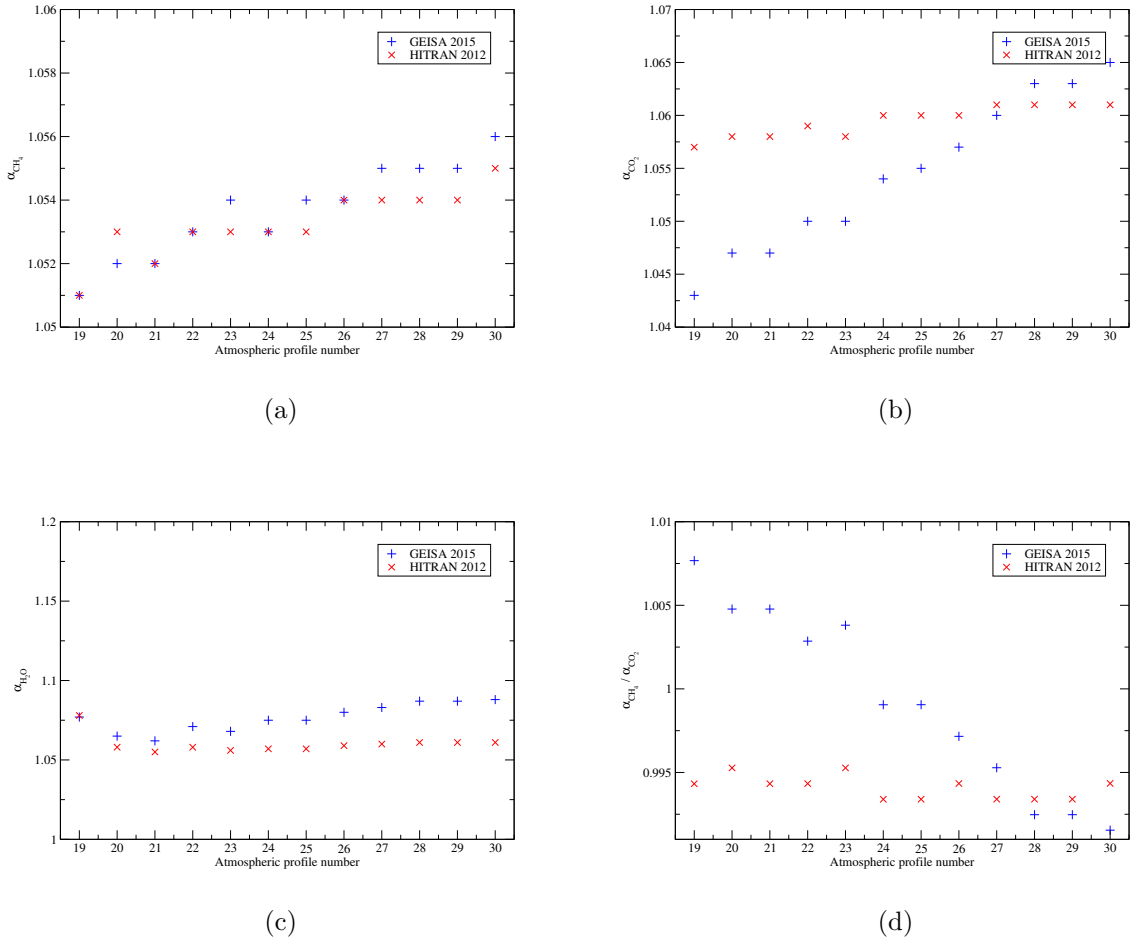

Figure 5.12: Scaling factors versus atmospheric profiles for different trace gases (SZA 20°). (a) Scaling factor for methane α_{CH_4}. (b) Scaling factor for carbon dioxide α_{CO_2}. (c) Scaling factor for water vapor α_{H_2O}. (d) Ratio of methane to carbon dioxide $\alpha_{CH_4}/\alpha_{CO_2}$.

Retrieval Error

Fig. 5.13 displays the errors of scaling factors. The errors of the retrieval using HITRAN are smaller than with GEISA. For the error of water vapor, there is an outlier for the profile No.19, which is unusual high. This could be explained for the extremely low concentration of H_2 that makes the retrieval for water inaccurate. In the orbit analysis (see Sect. 4.1.3), it can be found that the retrieval errors of water

vapor in the polar region with quite dry atmosphere are also higher than the others.

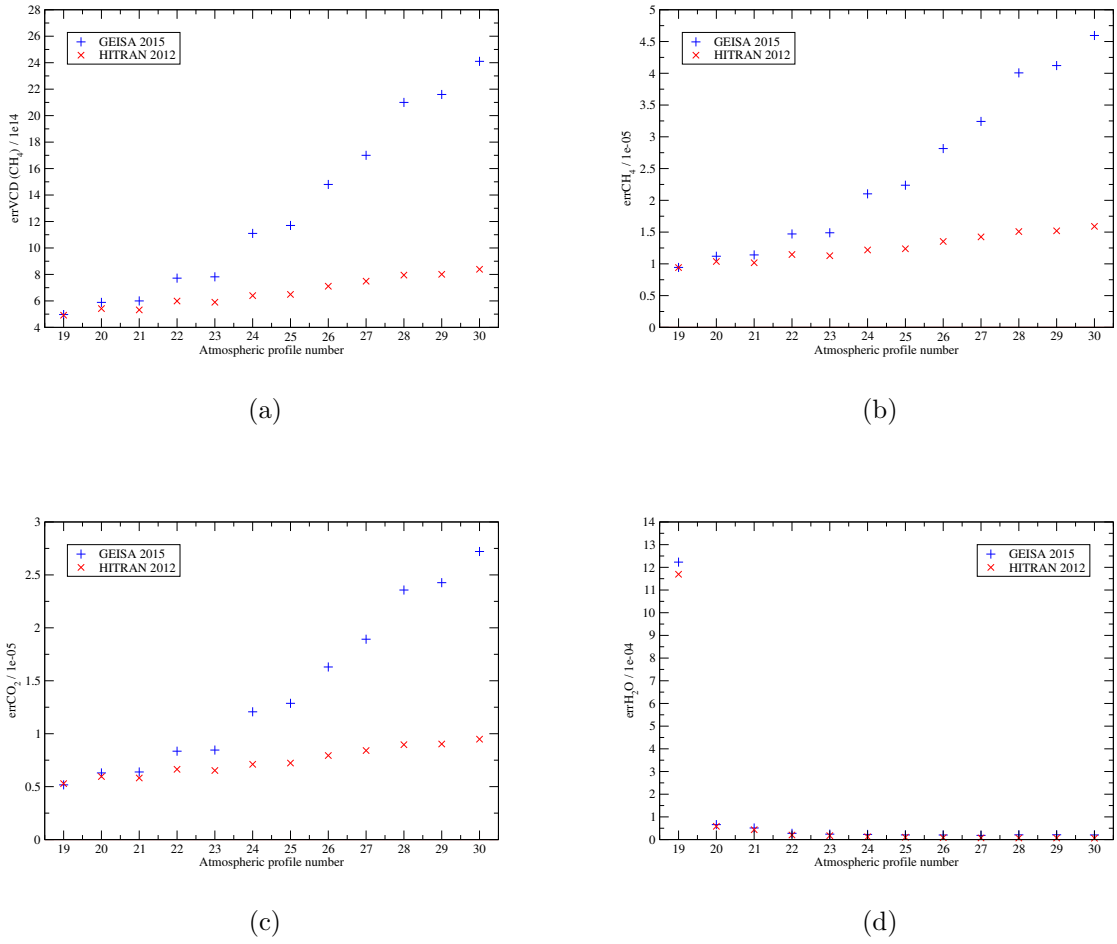

Figure 5.13: Errors versus different atmospheric profiles by CH_4 retrieval using HITRAN 2012 and GEISA 2015. (SZA 20°) (a) Error of VCD. (b) Error of scaling factor α_{CH_4}. (c) Error of scaling factor α_{CO_2}. (d) Error of scaling factor α_{H_2O}.

Chapter 6

Final Remarks

6.1 Conclusions

In the framework of this thesis the retrieval of methane VCD was conducted for ENVISAT orbit 8663 and towards the Sahara region, in order to assess the impact of the spectroscopic database on methane retrieval. The retrieval was conducted by the BIRRA software package using SCIAMACHY channel 6 short wave infrared spectra. Another retrieval using GOSAT simulated observation data intercompared the performance yielded by the two most recent released line databases and displays the influence of the certain climatological conditions on retrieval performance. The spectroscopic line parameter input is investigated in order to give a recommendation of the optimal parameter settings to achieve the highest possible retrieval quality for methane with BIRRA. The investigated fit parameters are the methane VCD, the norm residuals, the scaling factors for methane α_{CH_4}, carbon dioxide α_{CO_2} and water vapor α_{H_2O} as well as the respective retrieval errors for the VCD, CH_4, CO_2 and H_2O scaling factors. Moreover, the ratio of α_{CH_4} to α_{CO_2} is investigated due to the definition of a proxy-normalized final CH_4 VCD.

Before the retrieval started, the altitude sensitivity study exhibits the sensitivity for trace gases retrieval with respect to the altitude and the spectral range. This analysis ensures the meaning and accuracy of the retrieval. In general, methane VCD is determined by retrieval with high accuracy due to strong absorption lines in the fitting window. The orbit analysis of all parameters shows somewhat latitudinal dependency, at certain latitudes the results exhibit some outliers or unusual high values. The retrieved results may be affected by some determinative factors such as the surface reflectivity and the solar zenith angle. The surface albedo of the orbit state which has mixed terrain is quite variable and uncertain, that may lead to negative VCD for methane sometimes. The smaller solar zenith angle the observations are characterized, the stronger radiation signal is measured, hence the better condition for retrieval. On the other hand, analysis of latitude dependent data has shown the connection of the retrieved qualities to the water distribution

in the Earth's atmosphere. The equatorial climate is very humid and the corresponding atmosphere contains highly variable concentrations of water vapor, that is one of the largest uncertainties for radiative transfer calculations. Compared to the polar region with dry atmosphere, the retrieval residuals in the tropic and subtropic regions are generally higher. The region analysis towards the Sahara desert in October 2003 displays a good retrieval quality due to the small solar zenith angle, homogeneous and high surface albedo and low cloud coverage. The VCD, norm of residuals and the retrieval errors for each scaling factor all locate in a reasonable and stable range. The retrieved CH_4 VCD in the Sahara region is lower than the result by orbit 8663 analysis, which also reflects that the region has less natural or anthropogenic methane emission sources.

The comparison between spectroscopic line parameters have been conducted using HITRAN 1986, HITRAN 2012 and GEISA 2015 databases. From the statistic for the line parameters, e.g. the number of spectral lines, the range of line strengths and air broadening HWHM, it can be found that much more spectral lines are identified in the two recent databases and the maximum line strength (i.e. the strongest line) is almost identifiable for all the three databases. The newer databases simply have much more weak lines. The orbit analysis reveals that HITRAN 1986 achieves the worst retrieval quality, HITRAN 2012 and GEISA 2015 have a comparative performance, which yielded smaller residuals and retrieval errors for the scaling factors than HITRAN 1986. The general consensus is that the recent spectroscopic database is compiled with advanced spectral measurement techniques and more sophisticated theoretical treatment, consequently provides better retrieval results. For the orbit 8663, according to Table 4.3, GEISA 2015 is prepotent for the three fitting parameters and HITRAN 2012 achieves better results by two fitting parameters. For the Sahara region, GEISA 2015 shows a slight superiority in retrieval performance compared with HITRAN 2012.

The climatological input provides not only temperature and pressure profiles depending on latitude but also the volume mixing ratio profile for different gases which work as the a-priori for the retrieval. The actual conditions at the time of the measurements are unknown which may cause large deviations. The retrieval for the artificial GOSAT data simulated with different atmospheric profiles provides an insight into the impact of the climatological datasets. Compared with the real data retrieval, the scaling factor has a more homogenous distribution and is closer to one for the simulated data due to the certainty of the atmospheric conditions including the water vapor concentration. On the other hand, the simulated observations are created using HITRAN 2012 as the spectral line parameters input. The retrieved results yielded by HITRAN 2012 have a better quality than GEISA 2015 and the scaling factors for investigated gases stabilize near one by HITRAN 2012, which are in line with the expectation. It also illustrates from another point of view that with more accurate line parameters provided by spectroscopic database, the better

retrieval quality can be obtained.

6.2 Outlook

In the course of this thesis it has been shown that the retrieval of the SCIAMACHY SWIR data can be improved with further refinements. This thesis is just a beginning of a series of investigations that are to follow.

The strong interconnection of the surface reflectivity with the fit parameters has been observed by the analysis for orbit 8663 and the Sahara region. Independent surface reflectivity or albedo maps can be used to determine the relation on a global scale in order to retrieve the accurate albedo coefficients. Another major impact on radiative transfer modeling is the information on the atmospheric conditions at the time of the observation, the climatological database with higher spatial and temporal resolution and even an accurate a-priori estimate of water vapor is always required for good retrieval quality.

Water concentration in the humid atmosphere is quite variable, which is a big influence on retrieval. Due to weak absorption the signal for H_2O is low in the spectral intervals ($5986-6139\,\mathrm{cm}^{-1}$ and $6273-6419\,\mathrm{cm}^{-1}$), the H_2O is retrieved as an interfering gas. This poses a large uncertainty for retrieval calculations. Therefore, efforts can be made to implement the multiwindow fitting for water vapor retrieval. This can be used to retrieve H_2O from the fitting window centered around strong H_2O absorption lines, where H_2O is predominant absorber. The accuracy improving for water retrieval is advantageous for the CH_4 estimation.

It is well known that spectral regions with overlapping lines cannot be described by the sum of separate profiles because of the line mixing effect. In order to describe the spectral line shape in a more accurate way, the line mixing effect could be taken into account for the line by line radiation calculation in the GARLIC algorithm (mentioned in Sect. 2.3) in the near future. In this way, the retrieval accurancy for the trace gases can be enhanced.

Even though the ENVISAT mission has reached its end in 2012, the BIRRA code is still of large value to the scientific community as follow up missions are being planned. The Sentinel-5 Precursor mission (current launch data: in September 2017) is intended to provide data continuity for the SCIAMACHY instrument. Furthermore, GOSAT2 continues and enhances spaceborne measurement of major greenhouse gases from space started by GOSAT. Therefore, it is quite significative to maintain and refine the BIRRA software package for the use of trace gases retrieval within the near infrared spectral region.

Bibliography

G. Anderson, S. Clough, F. Kneizys, J. Chetwynd, and E. Shettle. AFGL atmospheric constituent profiles (0 – 120 km). Technical Report TR-86-0110, AFGL, 1986.

J. Angelbratt, J. Mellqvist, T. Blumenstock, T. Borsdorff, S. Brohede, P. Duchatelet, F. Forster, F. Hase, E. Mahieu, D. Murtagh, A. K. Petersen, M. Schneider, R. Sussmann, and J. Urban. A new method to detect long term trends of methane (CH_4) and nitrous oxide (N_2O) total columns measured within the ndacc ground-based high resolution solar ftir network. *Atmospheric Chemistry and Physics*, 11(13):6167–6183, 2011. doi: 10.5194/acp-11-6167-2011. URL `https://www.atmos-chem-phys.net/11/6167/2011/`.

B. Armstrong. Spectrum line profiles: The Voigt function. *J. Quant. Spectrosc. & Radiat. Transfer*, 7:61–88, 1967. doi: 10.1016/0022-4073(67)90057-X.

M. Buchwitz, R. de Beek, S. Noël, J. P. Burrows, H. Bovensmann, H. Bremer, P. Bergamaschi, S. Körner, and M. Heimann. Carbon monoxide, methane and carbon dioxide columns retrieved from SCIAMACHY by WFM-DOAS: year 2003 initial data set. *Atm. Chem. Phys.*, 5:3313–3329, 2005. doi: 10.5194/acp-5-3313-2005.

E. L. Fleming, S. Chandra, J. J. Barnett, and M. Corney. Zonal mean temperature, pressure, zonal wind and geopotential height as functions of latitude. 10(12): 11–59, 1990. doi: 10.1016/0273-1177(90)90386-E.

L. Garand, D. Turner, M. Larocque, J. Bates, S. Boukabara, P. Brunel, F. Chevallier, G. Deblonde, R. Engelen, M. Hollingshead, D. Jackson, G. Jedlovec, J. Joiner, T. Kleespies, D. McKague, L. McMillen, J.-L. Moncet, J. Pardo, P. Rayer, E. Salathé, R. Saunders, N. Scott, P. V. Delst, and H. Woolf. Radiance and Jacobian intercomparison of radiative transfer models applied to HIRS and AMSU channels. *J. Geophys. Res.*, 106(D20):24017–24031, 2001. doi: 10.1029/2000JD000184.

D. Gay. Usage summary for selected optimization routines (PORT mathematical subroutine library, optimization chapter). Computing Science Technical Report

153, AT&T Bell Laboratories, Murray Hill, NJ 07974, Oct. 1990. available at `http://netlib.bell-labs.com/cm/cs/cstr/153.pdf`.

S. Gimeno García, F. Schreier, G. Lichtenberg, and S. Slijkhuis. Near infrared nadir retrieval of vertical column densities: methodology and application to SCIAMACHY. *Atmos. Meas. Tech.*, 4(12):2633–2657, 2011. doi: 10.5194/amt-4-2633-2011.

S. Gimeno García, F. Schreier, G. Lichtenberg, and S. Slijkhuis. Near infrared nadir sounding of vertical column densities: Methodology and application to SCIAMACHY. *Atmos. Meas. Tech. Disc.*, 4(3):3685–3737, 2011. doi: 10.5194/amtd-4-3685-2011.

G. Golub and V. Pereyra. Separable nonlinear least squares: the variable projection method and its applications. 19:R1–R26, 2003. doi: 10.1088/0266-5611/19/2/201.

R. Goody and Y. Yung. *Atmospheric Radiation — Theoretical Basis*. Oxford University Press, second edition, 1989.

M. Gottwald and H. Bovensmann, editors. *SCIAMACHY — Exploring the Changing Earth's Atmosphere*. Springer, Dordrecht, NL, 2011. doi: 10.1007/978-90-481-9896-2.

J. Husson, B. Bonnet, N. Scott, and A. Chedin. Managment and study of spectroscopic information: The GEISA program. *J. Quant. Spectrosc. & Radiat. Transfer*, 48:509–518, 1992.

N. Jacquinet-Husson, E. Arié, J. Ballard, A. Barbe, G. Bjoraker, B. Bonnet, L. Brown, C. Camy-Peyret, J. Champion, A. Chédin, A. Chursin, C. Clerbaux, G. Duxbury, J.-M. Flaud, N. Fourrié, A. Fayt, G. Graner, R. Gamache, A. Goldman, V. Golovko, G. Guelachvili, J. Hartmann, J. Hilico, J. Hillman, G. Lefèvre, E. Lellouch, S. Mikhailenko, O. Naumenko, V. Nemtchinov, D. Newnham, A. Nikitin, J. Orphal, A. Perrin, D. Reuter, C. Rinsland, L. Rosenmann, L. Rothman, N. Scott, J. Selby, L. Sinitsa, J. Sirota, A. Smith, K. Smith, V. G. Tyuterev, R. Tipping, S. Urban, P. Varanasi, and M. Weber. The 1997 spectroscopic GEISA databank. *J. Quant. Spectrosc. & Radiat. Transfer*, 62:205–254, 1999.

N. Jacquinet-Husson, N. Scott, A. Chedin, L. Crepeau, R. Armante, V. Capelle, J. Orphal, A. Coustenis, C. Boonne, N. Poulet-Crovisier, A. Barbe, M. Birk, L. Brown, C. Camy-Peyret, C. Claveau, K. Chance, N. Christidis, C. Clerbaux, P. Coheur, V. Dana, L. Daumont, M. D. Backer-Barilly, G. D. Lonardo, J. Flaud, A. Goldman, A. Hamdouni, M. Hess, M. Hurley, D. Jacquemart, I. Kleiner, P. Köpke, J. Mandin, S. Massie, S. Mikhailenko, V. Nemtchinov, A. Nikitin, D. Newnham, A. Perrin, V. Perevalov, S. Pinnock, L. Regalia-Jarlot, C. Rinsland, A. Rublev, F. Schreier, L. Schult, K. Smith, S. Tashkun, J. Teffo, R. Toth,

V. Tyuterev, J. V. Auwera, P. Varanasi, and G. Wagner. The GEISA spectroscopic database: Current and future archive for Earth and planetary atmosphere studies. *J. Quant. Spectrosc. & Radiat. Transfer*, 109:1043–1059, 2008. doi: 10.1016/j.jqsrt.2007.12.015.

N. Jacquinet-Husson, L. Crepeau, R. Armante, C. Boutammine, A. Chedin, N. Scott, C. Crevoisier, V. Capelle, C. Boone, N. Poulet-Crovisier, A. Barbe, A. Campargue, D. C. Benner, Y. Benilan, B. Bezard, V. Boudon, L. Brown, L. Coudert, A. Coustenis, V. Dana, V. Devi, S. Fally, A. Fayt, J.-M. Flaud, A. Goldman, M. Herman, G. Harris, D. Jacquemart, A. Jolly, I. Kleiner, A. Kleinböhl, F. Kwabia-Tchana, N. Lavrentieva, N. Lacome, L.-H. Xu, O. Lyulin, J.-Y. Mandin, A. Maki, S. Mikhailenko, C. Miller, T. Mishina, N. Moazzen-Ahmadi, H. Müller, A. Nikitin, J. Orphal, V. Perevalov, A. Perrin, D. Petkie, A. Predoi-Cross, C. Rinsland, J. Remedios, M. Rotger, M. Smith, K. Sung, S. Tashkun, J. Tennyson, R. Toth, A.-C. Vandaele, and J. V. Auwera. The 2009 edition of the GEISA spectroscopic database. *J. Quant. Spectrosc. & Radiat. Transfer*, 112(15):2395 – 2445, 2011. doi: 10.1016/j.jqsrt.2011.06.004.

N. Jacquinet-Husson, R. Armante, N. Scott, A. Chédin, L. Crépeau, C. Boutammine, A. Bouhdaoui, C. Crevoisier, V. Capelle, C. Boonne, N. Poulet-Crovisier, A. Barbe, D. C. Benner, V. Boudon, L. Brown, J. Buldyreva, A. Campargue, L. Coudert, V. Devi, M. Down, B. Drouin, A. Fayt, C. Fittschen, J.-M. Flaud, R. Gamache, J. Harrison, C. Hill, O. Hodnebrog, S.-M. Hu, D. Jacquemart, A. Jolly, E. Jiménez, N. Lavrentieva, A.-W. Liu, L. Lodi, O. Lyulin, S. Massie, S. Mikhailenko, H. Müller, O. Naumenko, A. Nikitin, C. Nielsen, J. Orphal, V. Perevalov, A. Perrin, E. Polovtseva, A. Predoi-Cross, M. Rotger, A. Ruth, S. Yu, K. Sung, S. Tashkun, J. Tennyson, V. Tyuterev, J. V. Auwera, B. Voronin, and A. Makie. The 2015 edition of the GEISA spectroscopic database. *J. Mol. Spectrosc.*, 327:31 – 72, 2016. doi: 10.1016/j.jms.2016.06.007. New Visions of Spectroscopic Databases, Volume II.

A. Kuze, H. Suto, M. Nakajima, and T. Hamazaki. Thermal and near infrared sensor for carbon observation fourier-transform spectrometer on the greenhouse gases observing satellite for greenhouse gases monitoring. *Appl. Opt.*, 48(35): 6716–6733, Dec 2009. doi: 10.1364/AO.48.006716. URL `http://ao.osa.org/abstract.cfm?URI=ao-48-35-6716`.

A. Nikitin, O. Lyulin, S. Mikhailenko, V. Perevalov, N. Filippov, I. Grigoriev, I. Morino, Y. Yoshida, and T. Matsunaga. GOSAT-2014 methane spectral line list. *J. Quant. Spectrosc. & Radiat. Transfer*, 154:63 – 71, 2015. doi: 10.1016/j.jqsrt.2014.12.003.

R. Parker, H. Boesch, A. Cogan, A. Fraser, L. Feng, P. I. Palmer, J. Messerschmidt, N. Deutscher, D. W. T. Griffith, J. Notholt, P. O. Wennberg, and D. Wunch.

Methane observations from the Greenhouse Gases Observing SATellite: Comparison to ground–based TCCON data and model calculations. *Geophys. Res. Letters*, 38(15):L15807, 2011. doi: 10.1029/2011GL047871.

L. Rothman, R. Gamache, A. Goldman, L. Brown, R. Toth, H. Pickett, P. Poynter, J.-M. Flaud, C. Camy-Peyret, A. Barbe, N. Husson, C. Rinsland, and M. Smith. The HITRAN database: 1986 edition. *Appl. Opt.*, 26:4058, 1987.

L. Rothman, R. Gamache, R. Tipping, C. Rinsland, M. Smith, D. Benner, V. Malathy-Devi, J. Flaud, C. Camy-Peyret, A. Perrin, A. Goldman, S. Massie, L. Brown, and R. Toth. The HITRAN molecular database: editions of 1991 and 1992. *J. Quant. Spectrosc. & Radiat. Transfer*, 48:469–509, 1992.

L. Rothman, C. Rinsland, A. Goldman, S. Massie, D. Edwards, J.-M. Flaud, A. Perrin, C. Camy-Peyret, V. Dana, J.-Y. Mandin, J. Schroeder, A. McCann, R. Gamache, R. Wattson, K. Yoshino, K. Chance, K. Jucks, L. Brown, V. Nemtchinov, and P. Varanasi. The HITRAN molecular spectroscopic database and HAWKS (Hitran Atmospheric Workstation): 1996 edition. *J. Quant. Spectrosc. & Radiat. Transfer*, 60:665–710, 1998.

L. Rothman, A. Barbe, D. C. Benner, L. Brown, C. Camy-Peyret, M. Carleer, K. Chance, C. Clerbaux, V. Dana, V. Devi, A. Fayt, J.-M. Flaud, R. Gamache, A. Goldman, D. Jacquemart, K. Jucks, W. Lafferty, J.-Y. Mandin, S. Massie, V. Nemtchinov, D. Newnham, A. Perrin, C. Rinsland, J. Schroeder, K. Smith, M. Smith, K. Tang, R. Toth, J. V. Auwera, P. Varanasi, and K. Yoshino. The HITRAN molecular spectroscopic database: edition of 2000 including updates through 2001. *J. Quant. Spectrosc. & Radiat. Transfer*, 82:5–44, 2003. doi: 10.1016/S0022-4073(03)00146-8.

L. Rothman, D. Jacquemart, A. Barbe, D. C. Benner, M. Birk, L. Brown, M. Carleer, C. Chackerian, Jr., K. Chance, L. Coudert, V. Dana, V. Devi, J.-M. Flaud, R. Gamache, A. Goldman, J.-M. Hartmann, K. Jucks, A. Maki, J.-Y. Mandin, S. Massie, J. Orphal, A. Perrin, C. Rinsland, M. Smith, J. Tennyson, R. Tolchenov, R. Toth, J. V. Auwera, P. Varanasi, and G. Wagner. The HITRAN 2004 molecular spectroscopic database. *J. Quant. Spectrosc. & Radiat. Transfer*, 96:139–204, 2005. doi: 10.1016/j.jqsrt.2004.10.008.

L. Rothman, I. Gordon, A. Barbe, D. C. Benner, P. Bernath, M. Birk, V. Boudon, L. Brown, A. Campargue, J.-P. Champion, K. Chance, L. Coudert, V. Dana, V. Devi, S. Fally, J.-M. Flaud, R. Gamache, A. Goldman, D. Jacquemart, I. Kleiner, N. Lacome, W. Lafferty, J.-Y. Mandin, S. Massie, S. Mikhailenko, C. Miller, N. Moazzen-Ahmadi, O. Naumenko, A. Nikitin, J. Orphal, V. Perevalov, A. Perrin, A. Predoi-Cross, C. Rinsland, M. Rotger, M. Simecková, M. Smith, K. Sung, S. Tashkun, J. Tennyson, R. Toth, A. Vandaele, and J. V. Auwera. The

HITRAN 2008 molecular spectroscopic database. *J. Quant. Spectrosc. & Radiat. Transfer*, 110(9-10):533 – 572, 2009. doi: 10.1016/j.jqsrt.2009.02.013.

L. Rothman, I. Gordon, Y. Babikov, A. Barbe, D. C. Benner, P. Bernath, M. Birk, L. Bizzocchi, V. Boudon, L. Brown, A. Campargue, K. Chance, E. Cohen, L. Coudert, V. Devi, B. Drouin, A. Fayt, J.-M. Flaud, R. Gamache, J. Harrison, J.-M. Hartmann, C. Hill, J. Hodges, D. Jacquemart, A. Jolly, J. Lamouroux, R. L. Roy, G. Li, D. Long, O. Lyulin, C. Mackie, S. Massie, S. Mikhailenko, H. Müller, O. Naumenko, A. Nikitin, J. Orphal, V. Perevalov, A. Perrin, E. Polovtseva, C. Richard, M. Smith, E. Starikova, K. Sung, S. Tashkun, J. Tennyson, G. Toon, V. Tyuterev, and G. Wagner. The HITRAN2012 molecular spectroscopic database. *J. Quant. Spectrosc. & Radiat. Transfer*, 130:4–50, 2013. doi: 10.1016/j.jqsrt.2013.07.002.

B. W. Rust. Fitting nature's basic functions Part I: Polynomials and linear least squares. *Computing in Science & Eng.*, 3(5):84–89, 2001a. doi: 10.1109/MCISE.2001.947111.

B. W. Rust. Fitting nature's basic functions Part II: Estimating uncertainties and testing hypotheses. *Computing in Science & Eng.*, 3(6):60–64, 2001b. doi: 10.1109/5992.963429.

B. W. Rust. Fitting nature's basic functions Part III: Exponentials, sinusoids, and nonlinear least squares. *Computing in Science & Eng.*, 4(4):72–77, 2002. doi: 10.1109/MCISE.2002.1014982.

B. W. Rust. Fitting nature's basic functions Part IV: The variable projection algorithm. *Computing in Science & Eng.*, 5(2):74–79, 2003. doi: 10.1109/MCISE.2003.1182965.

F. Schreier. The Voigt and complex error function: A comparison of computational methods. 48:743–762, 1992. doi: 10.1016/0022-4073(92)90139-U.

F. Schreier. Comments on "a common misunderstanding about the Voigt line profile". 66(6):1860–1864, 2009. doi: 10.1175/2009JAS2906.1.

F. Schreier. Optimized implementations of rational approximations for the Voigt and complex error function. 112(6):1010–1025, 2011. doi: 10.1016/j.jqsrt.2010.12.010.

F. Schreier and S. Gimeno García. Py4CAtS – Python tools for line-by-line modelling of atmospheric radiative transfer. In R. F. Cahalan and J. Fischer, editors, *Radiation Processes in the Atmosphere and Ocean (IRS2012): Proceedings of the International Radiation Symposium (IRC/IAMAS)*, volume 1531 of *AIP Conference Proceedings*, pages 123–126. American Institute of Physics, 2013. doi: 10.1063/1.4804723.

F. Schreier, S. Gimeno García, P. Hedelt, M. Hess, J. Mendrok, M. Vasquez, and J. Xu. GARLIC – a general purpose atmospheric radiative transfer line-by-line infrared-microwave code: Implementation and evaluation. 137:29–50, 2014. doi: 10.1016/j.jqsrt.2013.11.018.

F. Schreier, S. Gimeno García, M. Vasquez, and J. Xu. Algorithmic vs. finite difference Jacobians for infrared atmospheric radiative transfer. 164:147–160, 2015. doi: 10.1016/j.jqsrt.2015.06.002.

G. Stephens. *Remote Sensing of the Lower Atmosphere*. Oxford University Press, 1994.

D. Turner. Absorption coefficient estimation using a two–dimensional interpolation procedure. *J. Quant. Spectrosc. & Radiat. Transfer*, 53:633, 1995. doi: 10.1016/0022-4073(95)00024-F.

R. A. Washenfelder, G. C. Toon, J.-F. Blavier, Z. Yang, N. T. Allen, P. O. Wennberg, S. A. Vay, D. M. Matross, and B. C. Daube. Carbon dioxide column abundances at the Wisconsin tall tower site. *Journal of Geophysical Research: Atmospheres*, 111(D22):n/a–n/a, 2006. ISSN 2156-2202. doi: 10.1029/2006JD007154. URL `http://dx.doi.org/10.1029/2006JD007154`. D22305.

D. Wunch, G. C. Toon, J.-F. L. Blavier, R. A. Washenfelder, J. Notholt, B. J. Connor, D. W. T. Griffith, V. Sherlock, and P. O. Wennberg. The Total Carbon Column Observing Network (TCCON). *Phil. Trans. R. Soc. A*, 369(1943):2087–2112, 2011.

T. Yokota, H. Oguma, I. Morino, and G. Inoue. A nadir looking SWIR sensor to monitor CO_2 column density for japanese GOSAT project. In *Proceedings of the twenty-fourth international symposium on space technology and science. Miyazaki: Japan Society for Aeronautical and Space Sciences and ISTS*, pages 887–889, 2004.